turnitin

# Hussam Sadique

## 2K17PhDME03_Hussamsadique_RD4.pdf

Delhi Technological University

---

## Document Details

**Submission ID**

trn:oid:::27535:106451444

**Submission Date**

Jul 30, 2025, 4:38 PM GMT+5:30

**Download Date**

Jul 30, 2025, 4:43 PM GMT+5:30

**File Name**

2K17PhDME03_Hussamsadique_RD4.pdf

**File Size**

5.7 MB

174 Pages

44,879 Words

250,513 Characters

# 4%  Overall Similarity

The combined total of all matches, including overlapping sources, for each database.

## Filtered from the Report

▸ Bibliography

▸ Quoted Text

▸ Cited Text

▸ Small Matches (less than 9 words)

## Exclusions

▸ 5 Excluded Sources

## Match Groups

**139** Not Cited or Quoted  4%
Matches with neither in-text citation nor quotation marks

**0**  Missing Quotations  0%
Matches that are still very similar to source material

**0**  Missing Citation  0%
Matches that have quotation marks, but no in-text citation

**0**  Cited and Quoted  0%
Matches with in-text citation present, but no quotation marks

## Top Sources

1%  🌐 Internet sources

4%  📖 Publications

2%  👤 Submitted works (Student Papers)

## Integrity Flags

**1 Integrity Flag for Review**

🚩 **Replaced Characters**
42 suspect characters on 21 pages
Letters are swapped with similar characters from another alphabet.

Our system's algorithms look deeply at a document for any inconsistencies that would set it apart from a normal submission. If we notice something strange, we flag it for you to review.

A Flag is not necessarily an indicator of a problem. However, we'd recommend you focus your attention there for further review.

## Match Groups

**139** Not Cited or Quoted   4%
Matches with neither in-text citation nor quotation marks

**0**   Missing Quotations   0%
Matches that are still very similar to source material

**0**   Missing Citation   0%
Matches that have quotation marks, but no in-text citation

**0**   Cited and Quoted   0%
Matches with in-text citation present, but no quotation marks

## Top Sources

| | | |
|---|---|---|
| 1% | 🌐 | Internet sources |
| 4% | 📖 | Publications |
| 2% | 👤 | Submitted works (Student Papers) |

## Top Sources

The sources with the highest number of matches within the submission. Overlapping sources will not be displayed.

**1**   Publication

Ulu, Ayse Gözde. "Experimental Investigation of Uninterrupted and Interrupted ...   **<1%**

**2**   Publication

Ukaegbu, Uchechi Faithful. "Optimization of a Solar-Assisted Combined Cooling, ...   **<1%**

**3**   Publication

Perry, Jeffrey L. "Fouling in silicon microchannel designs used for IC chip cooling ...   **<1%**

**4**   Internet

etheses.whiterose.ac.uk   **<1%**

**5**   Submitted works

SASTRA University on 2017-02-10   **<1%**

**6**   Submitted works

iGroup on 2024-11-04   **<1%**

**7**   Publication

Chaowei Chen, Fei Li, Xinyu Wang, Jingzhi Zhang, Gongming Xin. "Improvement o...   **<1%**

**8**   Submitted works

Institute of International Studies on 2024-04-14   **<1%**

**9**   Publication

Çetin, Murat. "Design and Experimental Investigation of Microchannel Heat Exch...   **<1%**

**10**   Publication

Madhuker, Reuben Joshua. "Improving the Impingement Cold Plate Thermal Desi...   **<1%**

| 11 | Internet | |
|---|---|---|
| coek.info | | <1% |

| 12 | Publication | |
|---|---|---|
| Ziqiang He, Yunfei Yan, Zhien Zhang. "Thermal management and temperature un... | | <1% |

| 13 | Publication | |
|---|---|---|
| "Fluid Mechanics and Fluid Power (Vol. 3)", Springer Science and Business Media L... | | <1% |

| 14 | Publication | |
|---|---|---|
| Mourad Rebay, Sadik Kakac, Renato M. Cotta. "Microscale and Nanoscale Heat Tr... | | <1% |

| 15 | Publication | |
|---|---|---|
| Svetlana N. Yanushkevich, Vlad P. Shmerko. "Introduction to Logic Design", CRC P... | | <1% |

| 16 | Publication | |
|---|---|---|
| Vodapally, Sai Nikhil. "Cybersecured Smart Intelligent Inverter for 5G-Enabled Gri... | | <1% |

| 17 | Publication | |
|---|---|---|
| Katarzyna Kopczewska. "Applied Spatial Statistics and Econometrics - Data Analys... | | <1% |

| 18 | Publication | |
|---|---|---|
| Qinghua Wang, Junyu Tao, Zhuo Cui, Tiantian Zhang, Guanyi Chen. "Passive enha... | | <1% |

| 19 | Submitted works | |
|---|---|---|
| Rajiv Gandhi Institute of Technology, Kottayam on 2025-06-01 | | <1% |

| 20 | Publication | |
|---|---|---|
| Ho, An Quang Hai. "Nuclear Hybrid Energy Systems as a Solution for Carbon-Free ... | | <1% |

| 21 | Publication | |
|---|---|---|
| Jiawei, Zuo. "Numerical Investigation of Heat Transfer of a Multi-Layered Microch... | | <1% |

| 22 | Publication | |
|---|---|---|
| Ali Alsharif, Ali Mohamed. "Development of U-Shaped Two-Phase Hollow Fiber-Liq... | | <1% |

| 23 | Submitted works | |
|---|---|---|
| De Montfort University on 2024-09-05 | | <1% |

| 24 | Publication | |
|---|---|---|
| Xu, Zhanyou. "Machine Learning Analytics for Predictive Breeding.", Iowa State U... | | <1% |

| | | |
|---|---|---|
| **25** | Publication | |
| Liang Du, Wenbo Hu. "An overview of heat transfer enhancement methods in mic... | | <1% |
| **26** | Publication | |
| Checketts, Gus Thomas. "Microchannel radiator: An investigation of microchanne... | | <1% |
| **27** | Publication | |
| Kanargi, Omer Bugra. "Enhanced Air Side Thermal Transport for High Efficiency H... | | <1% |
| **28** | Publication | |
| Xin Cui, Weichao Yan, Kian Jon Chua. "Hollow Fiber Membrane-Based Evaporative ... | | <1% |
| **29** | Internet | |
| link.springer.com | | <1% |
| **30** | Publication | |
| Li, Linqing. "Quantitative MR/MRI Analysis of Fluids in Porous Media", Proquest, 2... | | <1% |
| **31** | Publication | |
| Ji-Feng Zhu, Xian-Yang Li, Shuo-Lin Wang, Yan-Ru Yang, Xiao-Dong Wang. "Perfor... | | <1% |
| **32** | Publication | |
| Shashi Rastogi, Nilanjan Mondal, Chirodeep Bakli. "Systematic design of tree-like ... | | <1% |
| **33** | Submitted works | |
| University of Aberdeen on 2019-06-04 | | <1% |
| **34** | Publication | |
| Bin Li, Yuqi Cui, Guidan Li, Huangzhou Jiang. "Numerical analysis on thermal-hydr... | | <1% |
| **35** | Publication | |
| Xinyu Ji, Xiaoping Yang, Yuantong Zhang, Yonghai Zhang, Jinjia Wei. "Experiment... | | <1% |
| **36** | Publication | |
| M. Hajialibabaei, M.Z. Saghir. "A critical review of the straight and wavy microcha... | | <1% |
| **37** | Publication | |
| Namie, Shane. "The Reservoir Geomechanics and Production Effects on Permafro... | | <1% |
| **38** | Publication | |
| Weinan Zhou, Kaijun Dong, Qin Sun, Weimin Luo, Bobo Zhang, Shengli Guan, Gua... | | <1% |

**39**   Publication

"Advances in Heat Transfer and Thermal Engineering", Springer Science and Busi...   <1%

**40**   Publication

Bhoopesh Singh Bhati, Dimple Tiwari, Nitesh Singh Bhati. "IoT and AI-Enabled He...   <1%

**41**   Publication

Chaowei Chen, Xinyu Wang, Baoqiang Yuan, Wenjing Du, Gongming Xin. "Investi...   <1%

**42**   Publication

Ding, Ruikang. "Investigating Size–Dependent Mechanical Behavior of Sub–100 N...   <1%

**43**   Submitted works

Monash University on 2022-07-28   <1%

**44**   Publication

Nehad Abid Allah Hamza, Isam Mejbel Abed. "Hydrothermal performance throug...   <1%

**45**   Publication

Prabhakar Bhandari, Kamal S. Rawat, Yogesh K. Prajapati, Diwakar Padalia, Lalit ...   <1%

**46**   Publication

Xiao, Zuhui. "Essays on Marketing Strategies with Endogenous Reference-Depend...   <1%

**47**   Publication

Abney, William. "Exploring the Relationship Between Technical College Faculty M...   <1%

**48**   Publication

Al-Aghbari, Mohammed Zahir Salim. "Development and Applications of Multi-Obj...   <1%

**49**   Publication

Fatemeh Bagherighajari, Mohammadmahdi Abdollahzadehsangroudi, Mehdi Esm...   <1%

**50**   Submitted works

Higher Education Commission Pakistan on 2019-11-24   <1%

**51**   Submitted works

International Islamic University Malaysia on 2016-01-21   <1%

**52**   Submitted works

Mansoura University on 2021-02-14   <1%

| 53 | Publication | |
|---|---|---|
| Pankaj Srivastava, Ruchitkumar Ishwarlal Patel, Anupam Dewan. "Thermal perfor... | | <1% |

| 54 | Publication | |
|---|---|---|
| Smith, Rachael. "A Comparison Between CFD-Based Aerodynamic Models and BE... | | <1% |

| 55 | Submitted works | |
|---|---|---|
| South Bank University on 2024-09-13 | | <1% |

| 56 | Submitted works | |
|---|---|---|
| Universiti Sains Malaysia on 2018-06-21 | | <1% |

| 57 | Publication | |
|---|---|---|
| Zhiwei Huang, Yunho Hwang, Reinhard Radermacher. "Review of nature-inspired ... | | <1% |

| 58 | Publication | |
|---|---|---|
| "Fluid Mechanics and Fluid Power (Vol. 2)", Springer Science and Business Media L... | | <1% |

| 59 | Publication | |
|---|---|---|
| Haeun Lee, Minsoo Kang, Ki Wook Jung, Chirag R. Kharangate et al. "An artificial ... | | <1% |

| 60 | Publication | |
|---|---|---|
| Hamidreza Ermagan, Roohollah Rafee. "Effect of pumping power on the thermal ... | | <1% |

| 61 | Publication | |
|---|---|---|
| Hamidreza Ermagan, Roohollah Rafee. "Numerical investigation into the thermo-... | | <1% |

| 62 | Publication | |
|---|---|---|
| Hongzhao, Wang. "Flow Boiling Heat Transfer in Microchannels With Wettability-... | | <1% |

| 63 | Submitted works | |
|---|---|---|
| Imperial College of Science, Technology and Medicine on 2020-09-03 | | <1% |

| 64 | Submitted works | |
|---|---|---|
| Jordan University of Science & Technology on 2023-03-25 | | <1% |

| 65 | Publication | |
|---|---|---|
| Kangas, Joseph R.. "On a General Theory of Phase Change, Nucleation, and Growt... | | <1% |

| 66 | Publication | |
|---|---|---|
| Li, Lin. "Design of micromixer and microfluidic control system.", Proquest, 2014. | | <1% |

**67** Submitted works

Manchester Metropolitan University on 2025-05-13 <1%

**68** Publication

Md Atiqur Rahman. "Review on heat transfer augmentation in helically coiled tub... <1%

**69** Publication

Rafat Mohammadi, Nazanin Shahkarami. "Performance improvement of rectang... <1%

**70** Publication

Sangram Kumar Samal, Mohammed Qadeer, Sandip K. Saha. "Thermo-hydraulic p... <1%

**71** Publication

Shen, Jianqi. "Fischer-Tropsch Synthesis Fixed Bed Reactor Intensification", Unive... <1%

**72** Publication

Soojin Jun, Joseph M. Irudayaraj. "Food Processing Operations Modeling - Design ... <1%

**73** Submitted works

Universiti Tenaga Nasional on 2013-01-26 <1%

**74** Submitted works

University of Birmingham on 2023-08-30 <1%

**75** Submitted works

University of Duhok on 2022-09-15 <1%

**76** Submitted works

University of South Carolina-Aiken on 2019-04-14 <1%

**77** Publication

Xuelai Zhang, Zhe Ji, Jifen Wang, Xin Lv. "Research progress on structural optimiz... <1%

**78** Publication

Zaeim, Atousa. "Semi-Active Control for Independently Rotating Wheelset in Rail... <1%

**79** Internet

researchmgt.monash.edu <1%

# Numerical Investigation of Fractal-Shaped Microchannel Heat Sink (MCHS)

**A Thesis Submitted**
**In Partial Fulfillment of the Requirements**
**for the Degree of**

# DOCTOR OF PHILOSOPHY

**by**

## HUSSAM SADIQUE
**(Roll No. 2K17/PHDME/03)**

**Under the Supervision of**

| | |
|---|---|
| **Prof. SAMSHER** | **Prof. QASIM MURTAZA** |
| **(Supervisor)** | **(Joint Supervisor)** |



**Department of Mechanical Engineering**
**Delhi Technological University, Delhi**
**(Formerly Delhi College of Engineering)**
**Shahbad Daulatpur, Bawana Road, Delhi-110042, India.**

**July, 2025**

# CERTIFICATE

Certified that **Hussam Sadique (**2K17/PHDME/03) has carried out his research work presented in this thesis entitled **"Numerical Investigation of Fractal-Shaped Microchannel Heat Sink (MCHS)"** for the award of **Doctor of Philosophy** from the Department of Mechanical Engineering, Delhi Technological University, Delhi, under our supervision. The thesis embodies the results of the original work, and the student himself carries out studies. The contents of the thesis do not form the basis for the award of any other degree to the candidate or anybody else from this or any other University/Institution.

**Prof. Samsher**                                          **Prof. Qasim Murtaza**

(Professor)                                                    (Professor)

Department of Mechanical Engineering        Department of Mechanical Engineering

Delhi Technological University,                      Delhi Technological University,

Delhi-110042                                                 Delhi-110042

Date:

# CANDIDATE'S DECLARATION

I, Hussam Sadique, hereby certify that the work which is being presented in the thesis titled "**Numerical Investigation of Fractal-Shaped Microchannel Heat Sink (MCHS)**" in fulfilment of the requirements for the award of the Degree of Doctor of Philosophy, submitted in the Department of Mechanical Engineering, Delhi Technological University is an authentic record of my work carried out during the period from 01-08-2017 to 31-03-2025 under the supervision of Prof. Samsher and Prof. Qasim Murtaza.

The matter presented in the thesis has not been submitted by me for the award of any other degree from this or any other Institute.

Place: Delhi                                                        **Hussam Sadique**

Date:                                                              (2K17/PhDME/03)

# ACKNOWLEDGEMENTS

# ABSTRACT

The problem of effective temperature management has emerged as a significant obstacle to future developments in microelectromechanical systems (MEMS) and high-performance computing devices due to the growing integration and miniaturisation of electronic systems. Because of its small size and high surface-area-to-volume ratio, microchannel heat sinks (MCHS) have become a state-of-the-art option for efficient heat dissipation in constrained locations. This thorough analysis compiles a large body of research on enhancing heat transfer in MCHS using sophisticated geometrical adjustments, nanofluids, and best optimisation strategies.

With a focus on passive solutions like geometrical alterations, a first comprehensive analysis offers a thorough overview of state-of-the-art cooling strategies and divides MCHS enhancing techniques into active and passive categories. The study demonstrates how boundary layer development degrades thermal performance in straight channels and how fractal-shaped designs, which naturally produce chaotic advection and secondary flows, provide a ground-breaking method of improving convective heat transfer with negligible pressure drop penalties. Inspired by natural mass and energy transport phenomena, fractal MCHS (FMCHS) designs show exceptional ability to reduce temperature non-uniformity and thermal resistance.

In the beginning of the study, simplified MCHS geometries were investigated by adding square ribs with double-filleted and rounded corners. To comprehend the function of local geometric smoothening in flow behaviour and thermal augmentation, three configurations, such as MC-SQ, MC-SQ-FR, and MC-SQ-DFR were examined. Through boundary layer re-development and improved mixing, the results showed that adding fillets to the rib corners significantly improved thermal performance. The MC-SQ-FR design increased Nusselt numbers by 15-22% while only increasing pressure drop by 2-10%.

Building on this, a new FMCHS with cavities and ribs was suggested and subjected to ANSYS Fluent numerical analysis. Although there was a corresponding rise in pressure drop, the FMCHS with ribs (FMCHS-R) and diagonally positioned ribs (FMCHS-DR) layouts demonstrated the most notable heat transfer gains among the different configurations examined. An intelligent optimisation framework utilising Artificial Neural Networks (ANN) in conjunction with the Moth Flame Optimisation (MFO) algorithm was utilised to address the design trade-offs. This led

v

to an ideal configuration where the best thermal-hydraulic performance was obtained with a rib radius of 26% along the FMCHS paths at a flow rate of 200 ml/min.

RSM and HHO optimisation methods were also employed for the fractal microchannel heat sink (FMCHS) with ribs and cavities and show a thermal performance-thermal efficiency trade-off. RSM chose an FMCHS design with ribs (model value 1) and a moderate flow rate of 295 ml/min. The thermal resistance was 0.983, pumping work was 201.112 mW, high efficiency was 0.955, and Nusselt number (Nu) was 23.053. Conversely, HHO chose a rib-dominant hybrid design (model value 0.645) with a 400 ml/min flow rate. This design lowered thermal resistance to 0.7609 K-cm$^2$/W, improving cooling performance, but it also increased pumping work (376 mW) and decreased efficiency (0.8835). Nusselt was 21.59, slightly lower.

The effect of nanofluids, specifically water-based $Al_2O_3$ nanofluids, was examined in FMCHS under various Reynolds numbers (1000-3000) and a bottom heat flux of 50 W/cm² in order to further enhance the thermal performance. According to the findings, heat transport was significantly improved by nanofluids, quadrupling the Nusselt number at Re=3000. Increased viscosity and density resulted in a larger pressure drop, but the overall performance evaluation criterion (PEC) was greatly enhanced, demonstrating the thermophysical advantages of using nanoparticles.

The idea that integrating bio-inspired geometries, nanofluid cooling, and AI-based optimisation provides a revolutionary route for the next generation of ultra-compact, high-efficiency thermal management systems is essentially supported by this collective body of research.

**Keywords:** Microchannel heat sink (MCHS), fractal, ribs, cavity, thermohydraulic performance, Optimization, Nanofluid, ANN

# TABLE OF CONTENTS

viii

x

# LIST OF FIGURES

xiii

# LIST OF TABLES

# LIST OF SYMBOLS

| | |
|---|---|
| $D_h$ | Hydraulic Diameter |
| $Nu$ | Nusselt number |
| Re | Reynold Number |
| $n$ | normal-to-boundary direction |
| u, v, $w$ | x-, y-, z-components of flow velocity (m/s) |
| k | thermal conductivity (W/m.K) |
| $\mu$ | dynamic viscosity (Pa-s) |
| $C_p$ | specific heat capacity at a constant pressure (J/kg.K) |
| T | static temperature (°C) |
| Q | generated heat flux (W/m$^2$) |
| $Q_f$ | total effective heat transfer per second |
| $D_h$ | hydraulic diameter ($\mu$m) |
| $P$ | static Pressure (Pa) |
| $A_c$ | Inlet area of the FMCHS |
| $\dot{m}$ | mass low rate (Kg/s) |
| $\Delta P$ | pressure difference (Pa) |
| $\rho$ | density (kg/m$^3$) |
| $\emptyset$ | Nanoparticle volume fraction |
| $\Omega$ | pumping power (mW) |
| Objn | Objective function |
| Avg. | Average |
| q | volumetric flow rate (m$^3$/s) |
| u | Velocity |
| ρ | Density of fluid |
| υ | Kinematic viscosity |
| R | Correlation function |
| $R^2_{adj}$ | Fit Goodness |
| f | Force vector |
| $k_B$ | Boltzmann constant |
| λ | Mean free path |
| $\Delta$P | Pressure drops |
| m | Mass |

# ABBREVIATION

| | |
|---|---|
| 3D | Three-Dimensional |
| MCHS | Microchannel Heat Sink |
| FMCHS | Fractal Microchannel Heat Sink |
| HT | Heat Transfer |
| CFD | Computational fluid dynamics |
| PD | Pressure drop |
| DOE | Design of experiment |
| MOEA | Multi-Objective Evolutionary Algorithm |
| GA | Genetic algorithm |
| *PEF* | Performance Evaluation Factor |
| ANN | Artificial neural network |
| MFO | Moth flame optimization |
| HHO | Haris hawk optimization |
| RSM | Response surface method |
| μ-TAS | Micro-total analysis system |
| Obfn | Objective function |

## Subscripts

| | |
|---|---|
| f | fluid |
| s | solid |
| in | channel inlet |

# Chapter 1 INTRODUCTION

## 1.1    Motivation

Heat removal is a major challenge in nature, and it's also vital in many engineering applications. The efficient removal of ever-increasing heat flux has become a critical concern for thermal engineers as the current microelectronics industry has progressed. Recent advancements in advanced very large-scale integration (VLSI) technologies and MEMS micro-electromechanical systems (MEMS), along with associated micro-miniaturization, have resulted in a substantial increment in the packing densities and heat fluxes generation within these devices (up to 100 $W/cm^2$ [1]. Further miniaturization of electronic devices such as those found in avionics and advanced military equipment, has led to the requirement of heat removal exceeding 1000 $W/cm^2$ [2]  and this is beyond the capability of many heat removal technologies. The current trend shows a sharp rise in ICs and semiconductor devices and their associated markets, and hence a large increase in heat flux can be predicted [3].

As a result, developing an efficient cooling solution becomes a top priority.  traditional cooling methods are inadequate at dissipating the generated surplus heat within the IC. Furthermore, the proposed approach must be compatible with the ICs' shrunk size. Despite significant progress over the last few decades, high-heat-flux removal remains a difficult problem that requires ongoing investigation and research. To deal with the heat generated, researchers are working hard to develop micro cooling systems such as jet impingement, heat pipe, spray cooling, microchannel heat sinks (MCHS), etc. In the 1980s, there was a surge in interest in high-heat-flux electronic cooling. Microchannel initially reached the level of 790 $W/cm^2$ in the 1980s. Sprays took the lead in the 1990s, with 1200 $W/cm^2$. Jet impingement reached the ultra-heat flux in the 2000s, with a power density of 2000 $W/cm^2$ [4].

Moore's law states that greater heat energy dissipation is required every eighteen months since the transistor density roughly doubles [5] as depicted in Figure 1.1. There are already approximately 3-50 billion transistors in a chip [6], and research is still ongoing to expand that number. It's worth noting that the highest heat-flux removal approach isn't necessarily the best or most realistic option. Indeed, the practicality of such methods might be questioned at any time, as the goal is not only

1

to achieve high heat flux but also to achieve greater efficiency and reliability. Pumping power reduction, hot-spot mitigation, production costs, and other special needs emerging from various applications must all be considered while developing heat removal technologies.
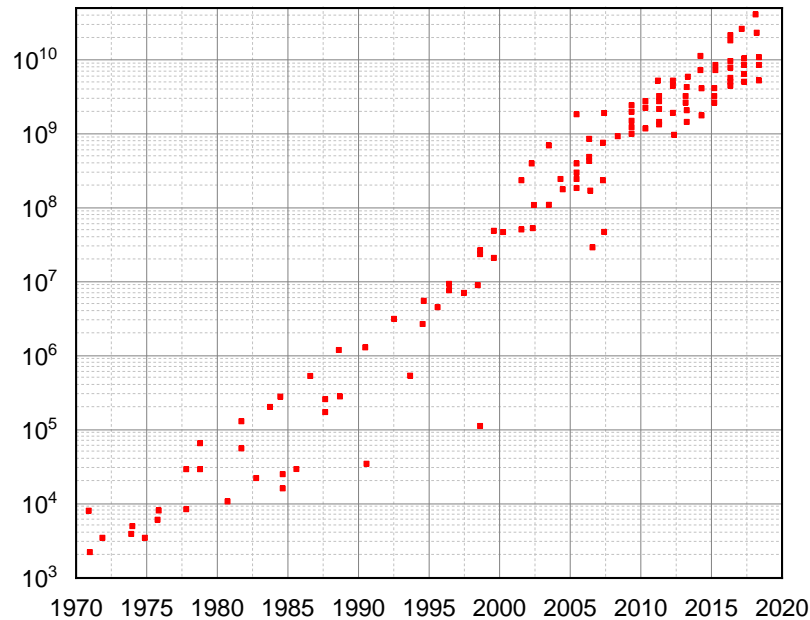


Figure 1.1 Transistors on an electronic chip over a period of time [5].

## 1.2    The rise of micro scale devices

In 2015, the market for thermal management technologies was assessed at 10.12 billion USD. The rapid growth of the renewable energy sector, nuclear industry, diode lasers, and electronic devices is accompanied by an increase in the amount of heat generated and, as a result, an unwanted temperature rise (Figure 1.2). The generated heat, or more precisely, heat flux, is one of the major roadblocks to technological advancement. In the near future, the growing demand for better heat removal methods in these miniaturized products is likely to encourage market growth [7].

Individual transistor reliability is exponentially dependent on operating temperature in many semiconductor technologies, and the median time to failure in hours (MTF) may be approximated using the Black's correlation [8], which takes the form:

$$MTF = \frac{1}{AJ^2} \exp{-\frac{\emptyset}{K_B T}} \tag{1.1}$$

where A is a constant that contains film cross-sectional area factor, J is the current density in Ampere (per $cm^2$), $\emptyset$ is the activation energy (in eV), KB is the Boltzmann

2

constant and T is the film temperature (Kelvin). This equation Eq. (1.1) shows that even a little rise in operating temperature can increase the device failure rate dramatically.
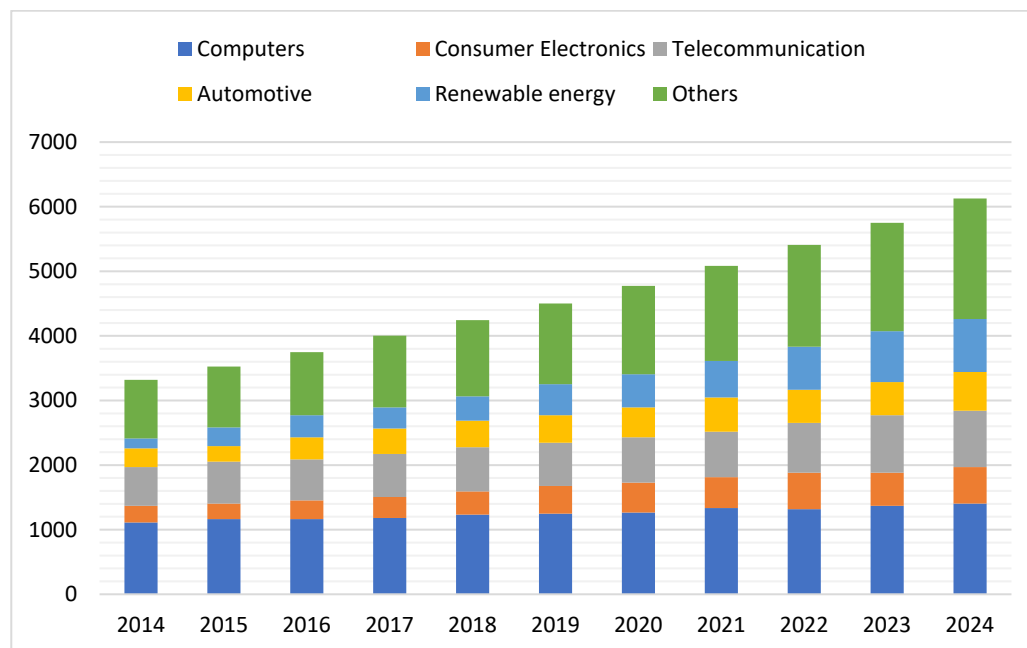


Figure 1.2 Thermal management technologies market in North America by application, 2014-2024 (USD Million) [9].
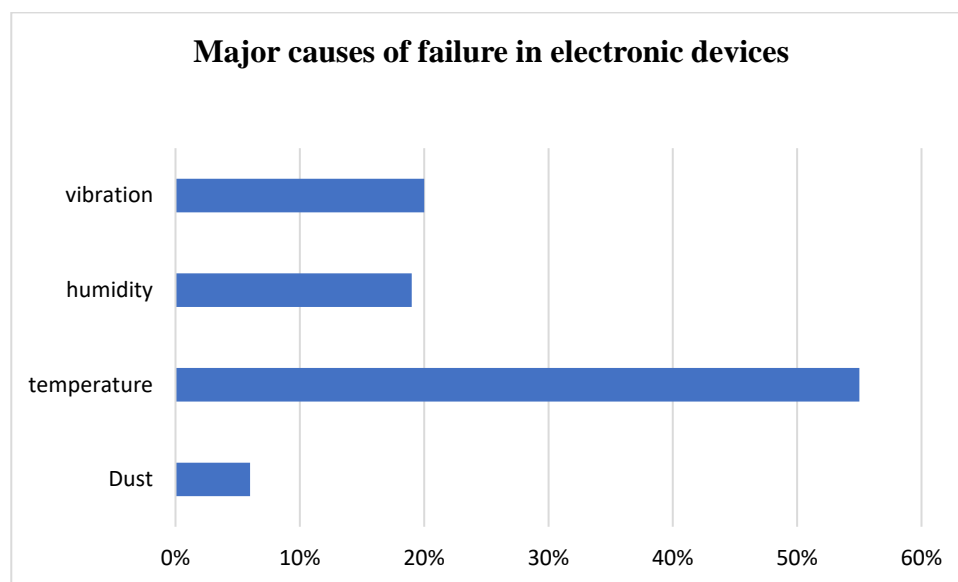


Figure 1.3 Major causes of failure of electronic devices [10].

Heat fluxes of more than 100 W/cm$^2$ are currently produced by ICs [11]. Electronic chip fabrication in the future is expected to generate the heat flux of 300 W/cm$^2$ [12], average heat flux of the chip can reach 200-450 W/cm$^2$ by the end of 2026 [13] or even more than 1000W/cm$^2$ at hotspots which may lead to failure of the

3

chip [14]. Hotspot heat flux of 700 W/cm2 has been reported by Feng et al. [15]. By the year 2026, IC hotspots could be as high as 2700–4500 $W/cm^2$ [16]. High power ICs involved in defense systems can generate heat flux up to 1000W/$cm^2$ [17]. Other technologies' high heat fluxes (HHF) can even exceed these figures. Furthermore, the microchip surface should be kept at a temperature lower than 85°C to avoid chip breakdown [12]. The removal of heat created by the ICs has become a major difficulty as the present heat removal technologies are not efficient enough to dissipate the required heat flux.

It is evident from Figure 1.3 that temperature is the main culprit in the failure of electronic devices. Around 55% of the failure is associated with the high operating temperature, followed by vibration and humidity of the surrounding.
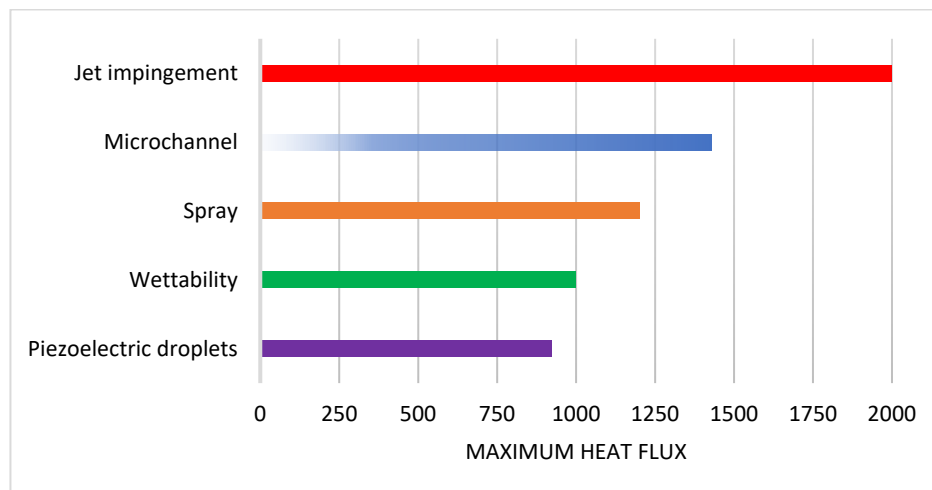


Figure 1.4 Maximum heat removal capacity of different cooling techniques [4].

## 1.3     Single- and two-phase heat transfer

Single-phase microchannel systems outperformed traditional cooling by a wide margin, but limitations such as temperature gradients caused by sensible heating and large pressure losses inside the channel encouraged the researchers to look for a better solution. Two-phase systems solve many of the disadvantages of single-phase flow by utilizing latent heat exchange, but implementation has been hampered by a lack of understanding of fluidic and thermal behaviour as well as concerns with flow instabilities. Two-phase cooling, on the contrary, has the best possibility of fulfilling future cooling demands. The flow boiling phenomenon results in higher coolant temperatures and lower flow rates, which improves efficiency and reduces cooling power consumption and cost. Isothermal cooling through latent heat transfer also presents a great opportunity to reduce stress caused by temperature non-uniformity,

4

hence enhancing device durability. Table 1.1 shows the difference between single phase and two-phase heat transfer with its advantages and disadvantages.

Table 1.1: Single-phase and two-phase flow advantages and disadvantages

|  | Advantages | Disadvantage |
|---|---|---|
| Single-phase | • Single-phase devices are used to be lightweight and compact.<br>• Very high heat flux can be obtained by reducing the diameter. | • High heat flux is achieved with the trade-off of large PD.<br>• Large temperature gradients are usually encountered in the flow direction.<br>• Rely on sensible heat for cooling and hence unable to achieve a large heat transfer coefficient. |
| Two-phase | • higher forced convective heat transfer coefficient<br>• increased temperature uniformity, and<br>• smaller coolant mass flow rates and hence reduced coolant reservoir. | • Hydraulic instabilities<br>• Existence of periodic dry zone<br>• Sometimes unpredictable, difficult to control, and leads to instability and local overheating.<br>• Choking may occur at a very small diameter, and this hampers heat transfer capability |

## 1.4    Heat transfer technologies and applications

With reference to the above paragraph, it is helpful to look at the features of today's most successful cooling strategies when looking for such solutions. A new generation of thermal management systems is required to protect electronic components, among other things, against increased heat flux and temperature peaks while also maintaining a compact overall package volume [18]. In terms of addressing the cooling requirements for compact space systems, heat removal technologies such as spray cooling, Microchannel heat sinks, porous media, heat pipe, jet impingement, etc., are highly promising.

Figure 1.4 depicts the maximum heat removal capabilities of various technologies. Jet impingement can remove the maximum amount of heat among all the cooling technologies available and involves less drop in pressure as compared to microchannels, however, it comes with many limitations. Such as, it causes substantial surface temperature fluctuations outside the impingement zone. This problem can be

5

solved by employing several impinging jets that spread temperature gradients over a large surface area. Microelectronic cooling applications often deal with a small surface area, hence jet impingement applicability is at odds with microelectronic cooling [19]. That is the reason why microchannel has got wide application area and popularity in high heat flux removal technologies.

Some of the technologies use conduction (Thermal interface material, Heat Pipe, etc.), Air convection (natural and forced air convection with extended surfaces such as fin), latent heat storage (phase change material), indirect liquid cooling (cold plates, thermosyphon, porous media, microchannels, heat pipe, etc.), direct liquid cooling (jet impingement, spray cooling, etc.)

The porous media heat removal technique is based on a porous metallic medium insert (in the form of a matrix) that increased both local mixing velocity and surface contact area-to-volume ratio [20]. Materials with high thermal conductivity are used as inserts, which results in efficient heat transfer to the coolant.

Microscale coolers can maintain the cooling temperature of electronic devices and appliances that generate intense heat. A MCHS's heat transfer performance is far superior to that of ordinary heat exchangers [21]. For high-heat-generating electronic equipment, forced convective liquid cooling using MCHS is one of the most promising and high-performance cooling solutions [22]. This emerging cooling method is also adaptable to on-chip integration, in addition to drastically reduced package size [23]. These two methods are comparable in terms of the heat transfer augmentation process, which is accomplished by improving the heat transfer contact area and intensifying the fluid flow within the channels.

The spray cooling approach is distinguished by high performance and uniform heat distribution, and it is a reliable means of cooling temperature-sensitive electronic components when compared to alternative options. In this, liquid droplets created with a nozzle are sprayed to a surface, and heat is dissipated by sensible heating of the liquid or evaporation. The heat transfer is also improved by secondary nucleation, which is generated by the entrainment of air in the thin layer [24] and it has been proved to be one of the most efficient cooling technologies [17]. Spray cooling is used to cool the computer chip and is a top contender for cooling high-voltage diode laser arrays on the ground, lasers used in space, and radar-based applications. During laser therapy for patients with port-wine stain birthmarks, spray cooling is also employed to cool human skin during laser dermatologic surgery [25].

6

Due to simplicity in design MCHS has got wide area of application such as in cooling of microelectronic devices [26], industrial heat exchangers [27], refrigeration system [28], automotive [29], process industries [30], bioengineering [31], renewable energy [32], microsensors [33], gas turbine blade cooling [34] etc. Porous media is commonly utilised in a variety of technical applications, such as drying operations [35], electronic cooling [36], solid matrix heat exchangers [37], heat pipe [38], in petroleum reservoirs [39], grain storage [40] etc. Some applications of impingement jets are in cooling of electronic devices, gas turbine blades and fusion reactors, solar collector, drying of tissue paper, textile, annealing, etc. [41,42]. Table 1.2 shows various cooling technologies with their advantages and limitations.

Table 1.2 Various cooling Techniques.

| Various cooling techniques | Advantages | Disadvantages |
|---|---|---|
| Spray cooling | • Offers uniform cooling, a wide range of applications, can use a wide range of cooling media, ease of manufacturing, low coolant flow rates, low thermal resistance at the contact, relatively quick cooling rate<br>• high heat dissipation capacity, low superheat degree, no temperature overshoot, low droplet impact velocity, and | • required proper adjustment, large parameters such as droplet size, droplet velocity, volumetric flux, spray angle, etc. are difficult to control.<br>• Filters, pumps, and the transportation of excess liquid and vapor to a condenser are all required for the functioning of spray cooling. |
| Microchannels | • Compact and lightweight<br>• Provide better heat transfer performance<br>• Reduced coolant flow requirement<br>• Maintain good temperature uniformity in a two-phase system | • As the number of flow pathways decreases, the pressure loss along the flow direction grows exponentially<br>• Clogging, temperature gradient.<br>• instabilities, as well as backflows, may occur in a |

7

| | | two-phase flow |
|---|---|---|
| Porous media | • compact size and high heat transfer area, high effective thermal conductivity, easy manufacturing. | • large pumping power requirement |
| Jet Impingement | • pressure drop is comparatively modest.<br>• Dissipates high heat flux densities, offers localized cooling.<br>• Can be used in compact space, with No thermal interference<br>• No manufacturing complexity | • Heat transfer is greatly affected by radially outward movement of fluid (liquid separation)<br>• Potential temperature uniformity issues for the single jet.<br>• Additional component cost and maintenance requirement |
| Heat Pipe | • With a low-temperature difference over the length of the pipe and passive operation, the PD is comparatively low and the heat transfer is efficient.<br>• High heat transfer rates over a long distance | • Operating conditions are constrained, and there are some instabilities associated with it.<br>• Small heat loads, gravity dependence. |
| Thermoelectric | • Efficient, silent, no mechanical moving parts, low maintenance, compact, high reliability, no working fluid, large cooling density | • Poor efficiencies lead to power consumption<br>• Limited heat removal capacity |

## 1.5    Microchannel Heat sink (MCHS)

MCHS has got the wide application in various disciplines such as Engineering, Biomedical Science, nanotechnology, material science, biotechnology, physical science, etc. same has been shown in below bar chart in which paper published between 1991 and 2020 has been shown in Figure 1.5, It is clear that MCHS has got an extensive range of applications from engineering to medical sciences.

Great progress has been made in recent decades in combination with the industrial miniaturization trend, leading to sophisticated micro and nanoscale technologies.

8

Fluid flows have been increasingly important in micro-scale applications in recent years. The idea for microchannel research came from the pioneering work of Tuckerman and Pease [43] in cooling VLSI applications.
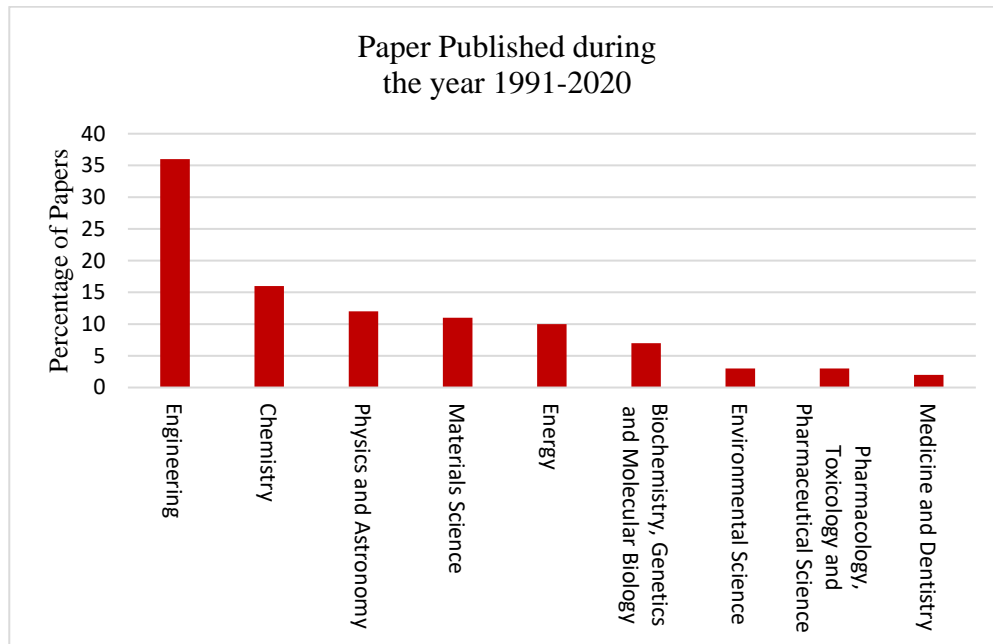


Figure 1.5 Different subject areas where papers on MCHS are published.
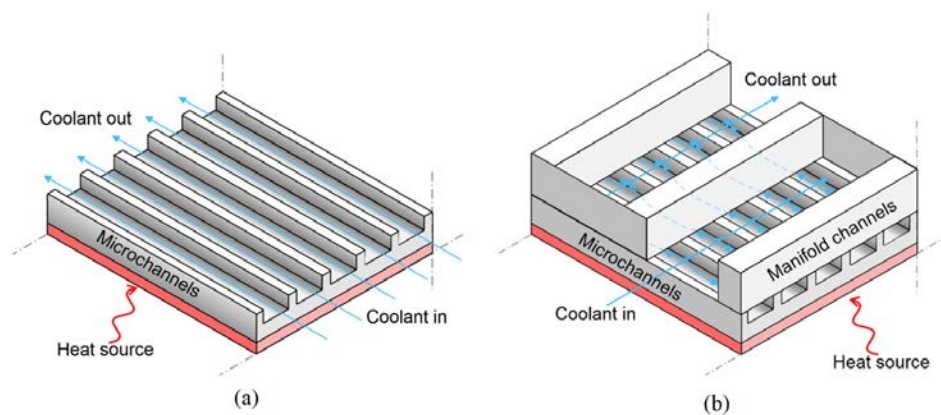


Figure 1.6 Microchannel heat sink (MCHS) as depicted in Gilmore et al. [44].

They created and put to the test a new water-cooled integral heat sink for silicon integrated circuits. The heat sink has been found to considerably improve the viability of complicated VLSI circuits at high power densities. Since then, this technique has gotten a lot of attention in important fields including fuel cell systems and sophisticated MCHS designs.

One of the most appealing features of microchannels is the incredibly little volume required on the bottom of the chip, which allows for multichip integration. Liquid maldistribution [45], large pressure drops along the flow direction [46], temperature

9

nonuniformity [47], and coolant leakage [48] are the key impediments and challenges faced by the researchers seeking to functionalize microchannel cooling technology.

The concept of microchannel cooling can be stated in Eq. (1.2) with the addition of the heat transfer coefficient.

$$h = k_f . \frac{Nu}{D_h} \qquad (1.2)$$

where h is the convective heat transfer coefficient (W/cm²K); k_f is the thermal conductivity of the fluid (W/cmK); $Nu$ is the Nusselt number, $D_h$ is the hydraulic diameter of the channel which can be defined as $D_h = \frac{2W_{ch}H_f}{W_{ch}+H_f}$, where $W_{ch}$ and $H_f$ being the width and height of the channel respectively. A fully developed laminar flow, the forced convection heat transfer coefficient h can be attained from, Eq. (1.2). The Nusselt number reported here varies depending on the cross-section shape and for the square channel under the condition of constant heat flux is found to be 3.61. Kandlikar and Grande [49] studied the effect of hydraulic diameter on heat transfer coefficient and pressure drop in a square channel for water and air with the same above mentioned conditions which are shown in  Figure 1.7. Figure 1.7(a) depicts the variation of h with hydraulic diameter $D_h$ and a sharp rise in the heat transfer coeffiecient is observed with the decrease in channel diameter. However chanenl hydraulic diameter cannot be infineltly reduced and the primary reason being the fluid viscosity [43]. Figure 1.7(b) shows the variation of pressure gradient with the hydraulic diameter of the square channel for air and water with a mass flow rate of 200 kg/m²s and incompressible flow assumption. It was observed that there was a drastic increment in the frictional pressure gradient with the decrease in the diameter of the channel.
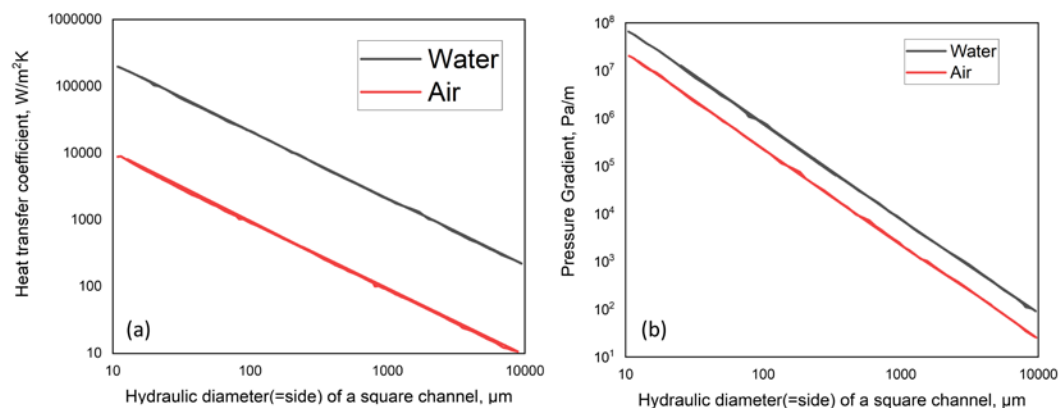


Figure 1.7 Plot of (a) heat transfer coefficient and (b) pressure gradient with hydraulic diameter of a square channel [49].

10

### 1.5.1 MCHS Fabrication Techniques

Microchannels generally have a hydraulic diameter in the range of 10–200 µm. Advances in microfabrication technology have substantially driven the evolution of MCHS.

Various technologies have been used to develop microchannel heat sinks over the last few decades. Many early investigations explored microchannels etching [50,51], with feature sizes of a few hundreds of micrometres, driven by utilization in electronic systems and the possibility to use microelectronics production. MCHS with metal substrate became much easier to manufacture due to the recent advances in micromachining such as Laser micromachining [52], micro-milling [53], micro-Ultra Sonic Machining (µUSM) [54], abrasive water jet machining [55]. Micro-Electro-Discharge Machining [56] is a mesoscale microfabrication technique that uses a plasma discharge to selectively remove an electrically conducting substance and provides relatively high design freedom and better accuracy. With the need for complex internal geometrical features and various shapes, conventional manufacturing technologies are found to be inadequate in the construction of MCHS. With the use of Additive Manufacturing (AM) in the construction of MCHS, the complex shaped feature can now be incorporated. Different metallic alloys with high thermal conductivity can be produced through AM-based technology which was not possible with other manufacturing techniques. Arie et al. [57] used stainless-steel (SS17-4), aluminium alloy (AlSi10Mg), and titanium alloy (Ti64) for the construction of manifold-MCHS using the Direct Metal Laser Sintering (DMLS) technique. Some other micro-fabrication technology includes Stereolithography and LIGA [58] etc.

### 1.5.2 MCHS Classification

Microchannels are classified in a variety of ways (Table 1.3). Researchers have provided different criteria for minichannels vs. microchannels.

Table 1.3: Various classifications of channels based on the different criteria.

| Authors, year | Type of channel |
|---|---|
| Mehendale et al. [59], 2000 | Microchannels: $D_h$=1-100 µm <br> Meso Heat Exchanger: $D_h$ =100 µm-1 mm <br> compact HE: $D_h$ =1 -6 mm <br> Conventional Channel: $D_h$ > 6mm |
| Kandlikar and Grande [49], | Microchannel heat sink:200 µm $\geq D_h$ > 10 µm |

11

| 2002 | Minichannel: 3 mm$\geq D_h>$ 6mm |
| | Conventional channels: $D_h > 3$mm |
| | Transitional Channels: 10 $\mu$m $\geq D_h > 0.1$ $\mu$m |
| Kew and Cornwell [60], 1997 | Microchannel if Co $\geq$0.5, where Co is confinement number. |
| Cheng and Wu [61], 2006 | Microchannel: if Bo<0.05 |
| | Minichannel: 0.05<Bo<3.0 |
| | Macro-channels: if Bo>3.0 |
| | Where Bo is bond number and is given by, Bo=$(D_h/lc)^2$ |
| | $= g(\rho_l - \rho_v)D_h^2/\sigma$ also Bo=$1/Co^2$ |

### 1.5.3 MCHS substrate material
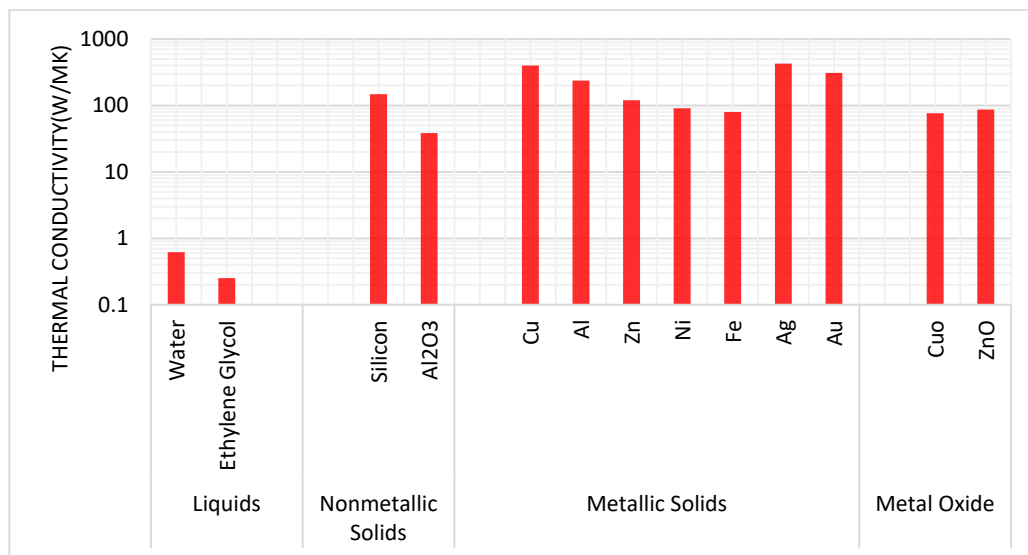


Figure 1.8: Probable materials for the MCHS fabrication (adopted from [62]).

Copper [46], Aluminum [63] and Silicon [64] are the frequently used substrate material found in reviewed literatures (Figure 1.8). According to Kang et al. [65], silicon has strong heat transfer and anticorrosive qualities, making the (1 1 0) silicon-based micro heat sinks appropriate for high temperature and corrosive environments.

### 1.5.4 MCHS Optimization schemes

As MCHS research advanced, the primary goal remained to reduce thermal resistance, lower the maximum base temperature, improve temperature uniformity, and increase compactness. Much research has been carried out to optimize the shape of the heat sink. In a study by Türkakar and Özyurt [66], it was observed that the channel with varying width, having narrow channels at the hotspot and coarser

12

channel elsewhere can increase the thermal performance of multi heat source device. Similarly, to improve the thermal performance of MCHS channel height- or width taper was varied by [67]. The hydrothermal performance of MCHS was optimized by [68]. Other optimization studies include the arrangement of the positions of the inlet and outlet of heat sink [69,70], optimization of substrate material of heat sink [71]. Different shapes of the pin fin in MCHS with nanofluids were optimized by [72], arrangement of pin fin in MCHS by [73], different orientation of fins by [74].

In order to minimize the thermal resistance associated with MCHS, a Y-shaped bifurcation plate was optimized by [75], multi-stage bifurcation also helped in achieving better thermal performance [76,77]. Shape optimization of microchannels such as wavy, circular, rectangular, zig-zag, rhombus, trapezoidal [58,78,79] and geometric parameters such as the number of the channel, hydraulic diameter [80], aspect ratio, the thickness of the base [81], height and width ratios, etc., flow parameters such as coolant flow rate, etc. are also found to be crucial in determining the optimal thermal performance of MCHS. Optimization tools such as Taguchi method [82,83] or heuristic algorithm based e.g., Genetic Algorithm (GA) [84,85], etc., can be employed.

## 1.6    Fractal Shaped MCHS (FMCHS)

The presence of a formal pattern that repeats itself even when the scale changes, characterize fractal structures, which are common in nature. This feature is known as 'self-similarity' [86]. Murray's law [87] is an important optimization principle in the construction of fractal-like branched systems with a wide range of functions and it states that the optimal network branching is attained when the cube of the parent channel radius equals the sum of the cubes of the daughter channel radii. it estimates the optimal diameter of branches in transportation networks to minimize the flow resistance and maintenance of the transport medium [88–90].

The study of fractal geometry further accelerated after the pioneering work of Mandelbrot [91]. Further, researchers have found the existence of fractal geometry in all elements of nature like in the respiratory and cardiovascular system of animals such as blood vessels, bronchial tree and vascular systems [92–96], leaf of the plant [97], coastline, river channels, plant root, snowflakes, etc. [98–101], where Murray's law has been proven to be a fair estimation. The main aim of hierarchically branched or fractal-shaped channels is to maximize heat transfer while reducing the fluid flow

13

and PD in a system [102]. Series of development in the area of Fractal microchannel heat sink (FMCHS) has been shown in Table 1.4

Bejan [103,104] has made the most significant contributions to the theories and literature on heat transfer in fractal and hierarchical systems, as well as methods for the synthesis and optimization of hierarchical networks. Bejan coined the term "constructal theory", in which scaling rules are allowed to change at each branch level. Fractal-like networks are a subset of feasible constructal networks [105]. Flow networks, as opposed to parallel flow configurations or serpentines, have been shown to have higher efficiency [98,106,107] and better temperature uniformity [108].

To give the optimized branching structure, minimum surface area, minimum flow resistance, minimum volume, and minimum power, were optimized using Murray's law. Based on early investigations, generalized Murray's law can be represented as follows [87,89,90,109,110]:

$$R_k^3 = \sum_{i=1}^{N} R_{k+1,i}^3 \tag{1.3}$$

Where $k$ and $k+1$ are parent and daughter branches respectively, R is the radius of branch pipe, N refers to the branching number in each bifurcation. The ratio of the parent branch to the daughter branch (i.e. $R_{k+1}/R_k$) in a symmetrical and dichotomous structure is $2^{-1/3}$.

Further development of Murray's law has been done by many researchers. For the turbulent flow regime, the optimized the branching structure by minimizing the pumping power and the expression is as follows [111]:

$$R_k^{7/3} = \sum_{i=1}^{N} R_{k+1,i}^{7/3} \tag{1.4}$$

Then in this case consecutive branching ratio $R_{k+1}/R_k$ is $2^{-3/7}$ for a symmetrical and dichotomous branching structure in turbulent flow regime and for the heat conduction to attain minimum thermal resistance, $R_{k+1}/R_k$ is $2^{-1/2}$ [90]. Kuo et al. [110] give the optimal ratio of turbulent flow through the rough pipe and is found to be -7/17 and this differs from smooth pipe flow conditions which are -3/7.

Murray's law can also be reduced for a symmetric branched tree-like network as follows [90]:

$$\beta_k = {d_{k+1}}/{d_k} = n^{-1/D_d} \tag{1.5}$$

14

$$\alpha_k = {}^{l_{k+1}}\!/\!_{l_k} = n^{-1/D_l} \qquad (1.6)$$

Where $D_d$ and $D_l$ are fractal dimension of diameter and length respectively.
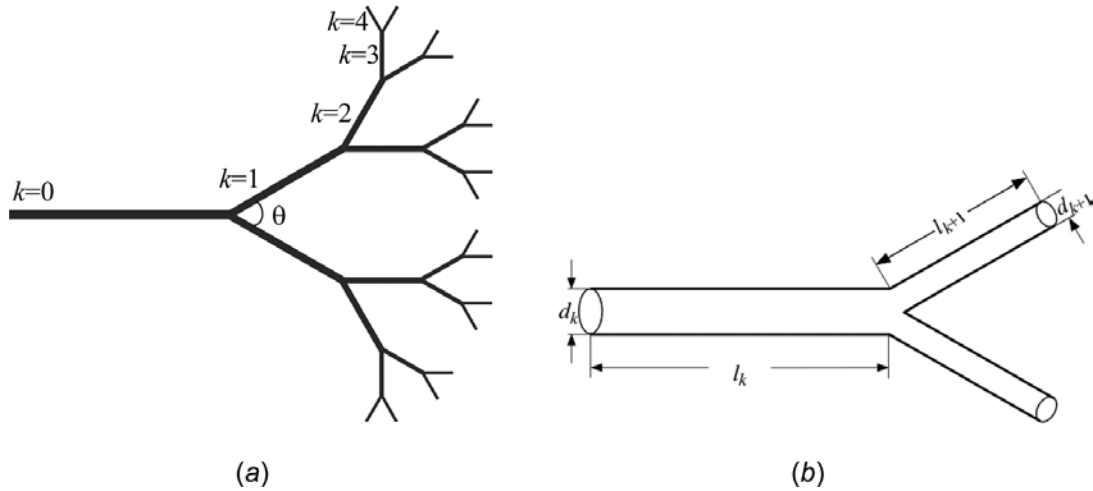


Figure 1.9: Schematic diagram for (a) a typical fractal treelike network (n=2, m=4, and =60º) and (b) $k_{th}$ branching structure [90].

Now from Figure 1.9, the treelike network consists of N branches from 0 to m level. $l_k$ and $d_k$ are length and diameter at arbitrary branching level k (0, 1, 2, ... to m). "n" shows the number of daughter branches at next level i/e at $k + 1$. From Figure 1.9, it is evident that n is 2 and m is 4.

Keeping in mind the importance of the fractal network in the thermal management of devices, optimal studies have been conducted by many researchers. Bejan et al. [89] optimized the T- and Y- shaped fractal structure by minimizing the flow resistance. Emerson et al. [112] applied Murray's law for the non-circular branching structures. Following the research of fractal shaped MCHS H-shaped [113–115] and Y-shaped [116,117] networks was proposed by many researchers.

Table 1.4 :Timeline of the development of fractal theory, inspired by [118]

| Researchers | Year(s) | Major findings |
|---|---|---|
| Murray [87] | 1926 | Developed Murray's law for optimal network branching. |
| Mandelbrot [91] | 1967 | Their research made fractal geometry a lot more accessible. |
| Sherman [109] | 1981 | Observed that the Murray's law is a functional link between vessel radius and volumetric flow, Re, vessel-wall shear stress, velocity profile, the average linear velocity of flow, and pressure gradient in individual vessels. |
| Mandelbrot [101] | 1982 | Natural fractal structures such as leaves, coastlines, and clouds are described. |

15

| West et al. [119] | 1997 | To reduce flow work, scaling principles (diameter ratio and length ratio) were developed for a bulk fluid transport phenomenon. |
|---|---|---|
| Bejan et al. [120]; Bejan [121–123] | 1997-2008 | Developed Constructal Theory: It explains the phenomenon of evolution (configuration, shape, and design) in nature, combining inanimate flow systems and living systems. |
| Xu and Yu [124] | 2006 | The scaling exponents of the transport properties in the networks were derived after analyzing the transport properties in the networks. |
| Chen and Chang [98,125] | 2002,2005 | Examined heat transfer in layered networks of Mandelbrot trees |
| Pence and co-workers [106,126,127] | 2003,2004 | They developed novel numerical approaches for heat transfer optimization. |

## 1.7    MCHS heat transfer enhancement techniques

Heat transfer enhancement methods are often divided into three categories: active, passive, and compound methods. The compound method has limited application due to its use in complex design [128]. Figure 1.10 depicts the various possible ways of heat transfer enhancement.

### 1.7.1 Active method

Improving the rate of heat transfer necessitates the use of an external power source. This external input source can be in the form of RF signal, electricity, or pumps. Mechanical mixing, fluid injection & suction, fluid vibration, surface vibration, and the addition of an external electrostatic or magnetic field that require external energy input and have been successfully used to intensify heat transfer [129]. External energy input, on the other hand, is costly and difficult to accommodate in many circumstances and hence has limited application.

Further, a feedback system is essential in cooling systems to target localized cooling. Closed-loop control of the chip's temperature is included in an adaptive cooling system. Thermal nonuniformity due to varying power distribution can produce deleterious strains on the IC substrate, therefore the ability to selectively cool different locations are critical. A nonadaptive cooling system is unable to respond to hot regions because it lacks a temperature feedback mechanism.

16

## 1.7.2 Passive method
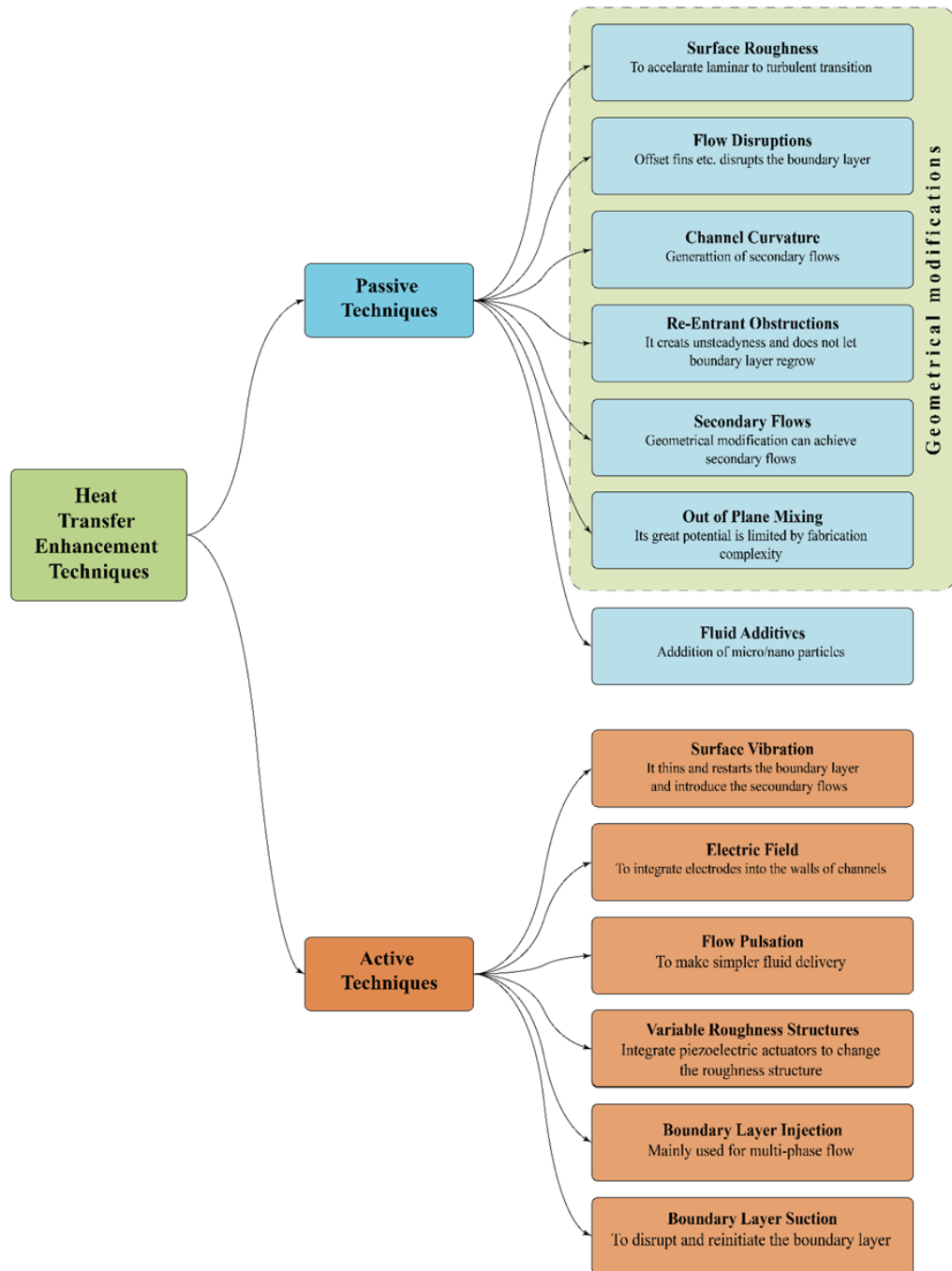


Figure 1.10: Active and passive heat transfer classification (adapted from [130]).

Heat transfer enhancement can be performed via passive means by creating flow disruption, altering the shape of the channel, change in channel curvature, the introduction of secondary flows, three-dimensional mixing, channel roughness, or attachments to increase surface area and turbulence, altering fluid properties through fluid additives (using nanoparticles) [131]. Limited thermal conductivity of heat

17

transfer fluids is an intrinsic restriction. As illustrated in Figure 1.8, water has the highest thermal conductivity of all the fluids we use today, yet it is ordered lower than most metals or metal oxides. These inherent limitations with the base coolants compelled designers to look for alternate coolants that could remove heat more effectively. Recent advancements in nanoparticle fabrication technologies have prompted a surge in nanofluid research to create viable alternative coolants with improved heat removal capabilities.

The use of a manifold microchannel, which provides higher uniform flow uniformity across the channel, is another passive heat transfer technology that also solves the shortcoming of single-layered microchannels of non-uniform flow distribution, and this also leads to more uniform temperature at the bottom wall. Apart from that, Tao et al. [132] proposed three probable mechanisms for improving single-phase heat transfer.

(1) Reduction in the thermal boundary layer, (2) Increase flow interruptions, and (3) Increase the velocity gradient near the heated surface are the three methods. Heat transfer enhancement is the outcome of all possible combinations of these mechanisms.

## 1.8    Nanofluids

Nanofluids are promise in microscale thermal management, especially in microchannel applications, due to their heat transfer ability. Copper oxide (CuO), titanium dioxide ($TiO_2$), and aluminium oxide ($Al_2O_3$) nanoparticles are mixed with base fluids like water or ethylene glycol to create engineered fluids. This solution enhances the fluid's interfacial properties, viscosity, and thermal conductivity.

When Choi and Eastman [133] created the basic concept of nanofluids at Argonne National Laboratory in the United States in 1995, thermal fluid research saw a dramatic shift. Numerous studies since then have demonstrated that nanoparticles have unique size-dependent characteristics, including high surface area-to-volume ratios, superior thermal conductivities, and enhanced mechanical, electrical, magnetic, and optical capabilities. When combined, these properties improve the performance of nanofluids in heat transfer systems, especially in high-performance, small-space applications such as MCHS.

One of the key benefits of using nanoparticles in heat transfer fluids as opposed to microparticles is their enhanced stability and dispersion within the base fluid.

18

Compared to microparticles, which are prone to rapid sedimentation and can cause issues including blockage, erosion of channel walls, and large pressure drops, nanoparticles stay better suspended due to their minuscule size and lower settling velocity. They are therefore ideal for usage in microchannels, which are tiny and prone to obstruction. However, nanoparticles can also combine due to their high surface energy and activity, which can affect the thermal performance and flow characteristics of the nanofluid. To get around this problem, the fluid is usually treated with surfactants or dispersants. These additives support suspension stabilisation by reducing surface tension and inter-particle attractions, ensuring long-term homogeneity and efficient heat conductivity in microchannel systems.

Combining two or more distinct types of nanoparticles into a single base fluid creates a new class of modified fluids called hybrid nanofluids. This multi-component approach aims to synergistically use the advantages of each type of nanoparticle to produce enhanced thermophysical, optical, rheological, and morphological properties as compared to conventional single nanoparticle (mono) nanofluids. Because of their better performance, hybrid nanofluids are increasingly being explored as a potential replacement for traditional nanofluids. Among their primary benefits are a wider absorbance spectrum, improved thermal conductivity, lower extinction coefficients, and reduced frictional losses. They are also typically less power-intensive to pump and exhibit fewer pressure drops, making them ideal for heat transfer applications, especially in tiny systems like microchannels. The basic classification of nanoparticles based on how they interact with various working fluids is shown in Figure 1.11, emphasising the variety and possible pairings utilised in hybrid nanofluid formulations.

Key feature of Nanofluids in Microchannels

    i. By encouraging the development of secondary flows and enhancing chaotic advection, nanoparticles in microchannels greatly increase mixing efficiency.

    ii. By encouraging a more even and quick dispersion of particles throughout the fluid, phenomena like thermophoresis and Brownian motion further quicken the mixing process.

    iii. Additionally, nanoparticles alter the base fluid's rheological behavior, which affects the pressure drop and general flow dynamics in microchannels.

The following are the main difficulties in using nanofluids:

19

i. Eensuring stability over time, as performance is hampered by nanoparticles' tendency to settle or cluster.

ii. The potential for particle buildup in microchannels, especially in constrained flow routes, can result in blockage or fouling.

iii. High levels of viscosity, which might raise flow resistance and necessitate more pumping force.
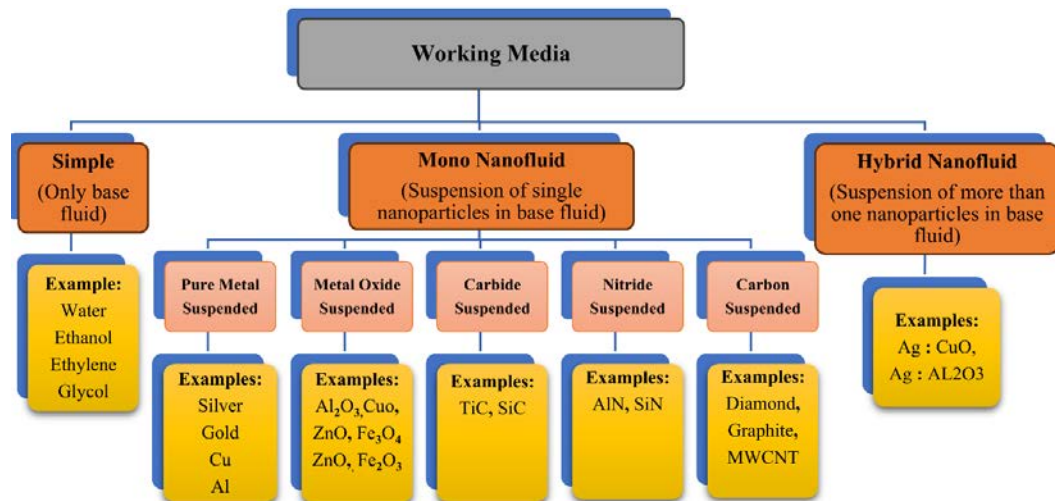


Figure 1.11 Classification of nanofluid [133].

## 1.9    Outline of the Thesis

An overview of microchannel heat sinks, with an emphasis on fractal microchannel heat sinks (FMCHS), is provided in **Chapter 1: Introduction**, the first section of the thesis.  It talks about their benefits for increasing heat transfer efficiency in a variety of high-performance applications and emphasises their importance in sophisticated thermal management systems.

**Chapter 2: Literature Review** explores the literature available on heat transfer enhancement in microchannel heat sink with particular emphasis on fractal microchannel heat sink. Channels with different cross-sectional geometries were studied.  It reviews the use of Computational Fluid Dynamics (CFD) in microchannel analysis and identifies research gaps to formulate the objectives for the present study.

The Navier-Stokes, continuity, and momentum equations utilised in this investigation are among the governing equations for fluid flow that are presented in **Chapter 3: Methodology.**  It also describes the computational approach, including the design of the various models of 3D fractal microchannel heat sink, numerical simulation setup, and mesh sensitivity analysis, and explains CFD methodologies and

20

important performance metrics like the Nusselt number, pressure drop, temperature distribution, thermal resistance, and performance evaluation criteria. It outlines the boundary conditions for the investigation and describes the nanofluid simulation instances.

**Chapter 4: Results and Discussion** analyses the thermohydraulic performance across different fractal microchannel heat sink designs and validates the strategies against bench data. The effects of flow rate, different model configurations, on thermal and hydraulic performance have also been discussed. A comparative study of various FMCHS models have been studied. Effects of nanofluid on thermohydraulic performance of FMCHS were also discussed in detail. Further moth optimization of FMCHS were discussed.

A final summary of the study's main conclusions and contributions can be found in **Chapter 5: Conclusions, Future Work, and Social Impact**. Along with offering suggestions for additional research, it addresses the research's shortcomings and applications.

The thesis concludes with references and appendices containing supplementary data and computational details.

21

# Chapter 2 LITERATURE REVIEW

In the design of MCHS, the high amount of heat removal and uniformity of substrate temperature are significant factors to consider. This could be accomplished through better coolant distribution, heat flux distribution, or the use of working fluids with better properties, for example, nanofluids. When using water as a coolant and in cases where heat flux distribution is challenging, the availability of low-temperature coolant to various parts of the sink is critical to assure substrate temperature homogeneity. This can be accomplished with a MCHS design that includes capabilities for improved coolant distribution and shape optimization. This element of coolant distribution, however, has been extensively studied to increase the heat removal rate while minimizing the substrate temperature gradient. The presence of thermally developing zones and coolant mixing is predicted to help microchannel heat sinks transport heat more efficiently.

The following are the primary causes for increased heat transfer in enhanced MCHSs [134]: (1) the extension of heat transfer area due to microchannel surface modified by microstructures (such as ribs and cavities) results in heat transfer performance enhancement [135]; (2) Due to the existence of flow disrupting elements (ribs, fins, and cavities), the thermal and hydrodynamic boundary layers are interrupted and redeveloped frequently or the change of stream-wise direction [136]; (3) the vortexes generated by secondary flow due to the presence of flow disturbing elements or the change of stream-wise direction, intensify the flow disturbance, thereby reducing temperature gradient and disarranging the boundary layers [137].

## 2.1    Heat transfer enhancement through design modifications

Corrugated channels are undoubtedly one of the most significant applications in the area of passive heat transfer enhancement. The flow mixing between higher temperature fluid layers along the channel wall and lower temperature fluid layers in the core region is significantly improved using this technique. Dean vortices and Chaotic advection are thought to be responsible for inducing high flow mixing [138]. As the flow becomes regular and the boundary layers grow, the heat transfer performance in straight channels degrades in the flow direction. Secondary flows (Dean vortices) can be formed when liquid flows through curved passageways, which improve fluid mixing and hence heat transfer [139].

22

### 2.1.1   Wavy MCHS

Straight MCHS suffer from a problem where the flow becomes regular and the boundary layer thickens [139,140], resulting in poor heat transfer performance along the stream-wise direction. In wavy microchannels with a low Reynolds number, Dean vortices have been seen to form rapidly along the flow direction and disrupt the boundary layer [141,142]. As a result, wavy microchannels can perform better in terms of heat transfer. The thickness of the thermal boundary layer can be reduced and the velocity gradient near a HT wall can be increased to improve convective HT [132].

Heat transport and fluid flow in a 3D wavy microchannel heat sink (MCHS) with a rectangular cross-section were investigated numerically by Sui et al. [139]. They noticed the development of secondary flows (Dean vortices) using the Poincaré section approach. These flows fluctuated along the channel and caused chaotic advection, which improved heat transmission and fluid mixing. In high heat flux zones, increasing wall waviness either locally or streamwise greatly enhanced heat transfer while comparatively reducing pressure drop penalties Figure 2.1. While the pressure drop only rose by 1.38 to 2 times, the heat transfer enhancement varied from 1.71 to 2.95.
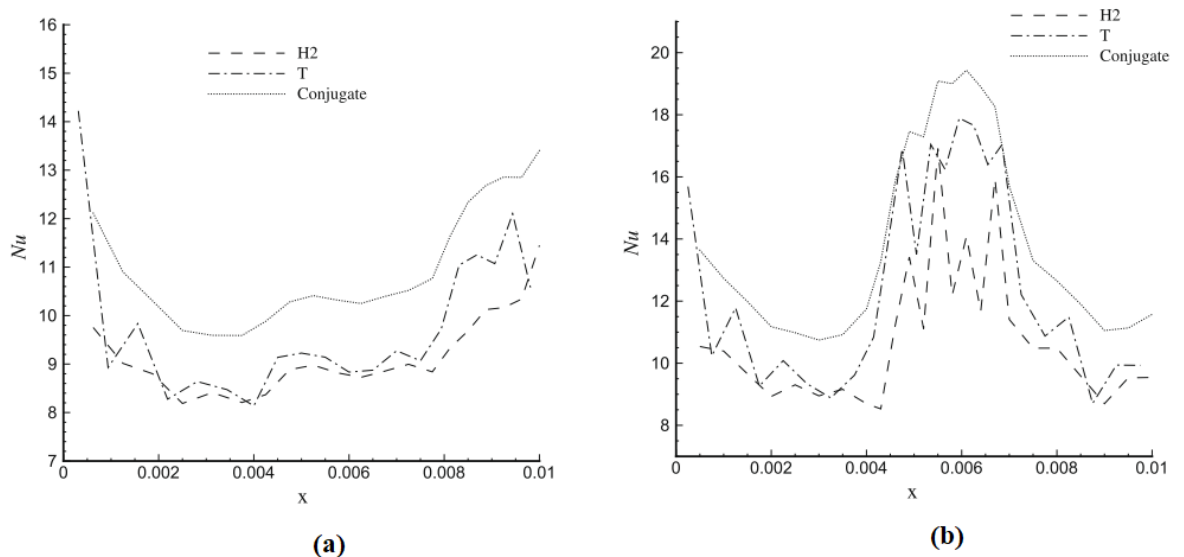


Figure 2.1 Variation of Local Nu along the wavy MCHS with increasing relative wavy amplitude (a) in streamwise direction (b) locally at Re = 300 [139].

Rostami et al. [143,144] used a Eulerian–Lagrangian two-phase model for nanofluids to quantitatively study conjugate heat transport in wavy microchannels. In

23

[143], the SIMPLE algorithm was used to study a water–$Al_2O_3$ nanofluid (120 nm, $\varphi$ =0–2%). The results indicated that secondary flows and recirculation caused a 195.7% increase in pressure drop and a 162.6% increase in Nusselt number when compared to straight channels. Nu rose by 11.6% at $\varphi = 0.02$ while using nanofluid rather than pure water, with a little change in pressure loss (<2.4%). According to an analysis of water-Cu and water–$Al_2O_3$ nanofluids in [144], the Eulerian–Lagrangian model performs better than single-phase models. Nu increased with decreasing particle size and volume fraction. With only a 10.6% increase in pressure drop, the water–Cu nanofluid increased Nu by 33.2% at $\varphi = 0.02$. These findings demonstrate how well nanofluids work to improve heat transmission in wavy MCHS while imposing controllable pressure penalties.
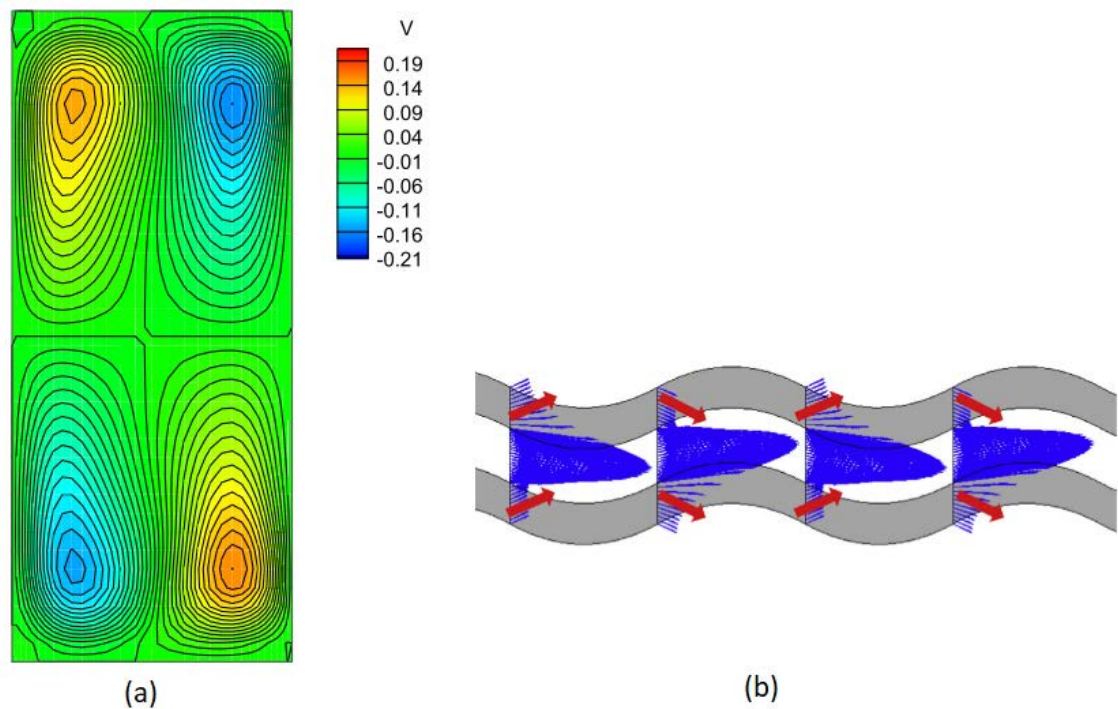


Figure 2.2: Depiction of Mechanisms of heat transfer performance enhancement in wavy MCHS with porous fins due to the development of Dean vortices [145].

Sakanova et al. [146] quantitatively studied how wavelength, wavy amplitude, volumetric flow rate, and volume percentage affect nanofluids. Diamond-water, CuO-water, and SiO2-water nanofluid are employed for 1%–5% nanoparticle volume fraction. When employing pure water and nanofluids as coolants, the wavy MCHS outperforms the rectangular one, but at high volume fractions of 5%, the difference is minimal. Higher amplitude and shorter wavelength reduce thermal resistance. Amplitude, volumetric flow rate, and wavelength decreases cause significant pressure

24

drop. However, nanofluids in wavy channels lose their effect as amplitude and wavelength decrease. This study found that diamond-water nanofluid has the highest HT coefficient and lowest thermal resistance.

Lu et al. [145] study wavy MCHS with porous fins to reduce pressure loss and heat resistance. Figure 2.2 shows that Dean vortices, channel length, and forced permeation by jet-like impingement improve coolant mixing and heat transfer performance, while permeation and slip effect of the coolants reduce PD.

A numerical analysis of heat and mass transmission in non-uniform wavy microchannels was conducted by Yuan et al. [147]. The overall wavelength ($\lambda = \lambda 1 + \lambda 2$) for each design was 5 mm. Whereas non-uniform wavy channels had unequal segments, uniform ones had equal $\lambda 1$ and $\lambda 2$. MCH-00 (smooth), MCH-01, MCH-02.5, MCH-05 (uniform), MCH-14 (convergent: $\lambda 1=1$ mm, $\lambda 2=4$ mm), and MCH-41 (divergent: $\lambda 1=4$ mm, $\lambda 2=1$ mm) were among the configurations employed. Among these, MCH-41 outperformed MCH-05 and MCH-14 in terms of heat transfer, entropy generation, and thermal resistance.

Mohammed et al. [148] studied rectangular wavy MCHS with amplitudes ranging from 125–500 µm and Reynolds numbers between 100–1000. Wavy channels showed significantly better heat transfer than straight ones with the same cross-section, with pressure drop penalties being much lower than the heat transfer gains. Increasing wave amplitude raised both the friction factor and heat transfer coefficient across all Re. The central channel consistently exhibited the highest heat transfer. Overall, wavy MCHS with a dimensionless amplitude ($\alpha$) between 0.0625 and 0.21875 delivered the best thermal performance.

Cho et al. [149] numerically studied flow behaviour in microchannels under four conditions: pure EOF, pure PDF, combined EOF/PDF with favourable and adverse pressure gradients. Flow recirculation occurred in PDF but was absent in EOF. Electrokinetically induced velocity was more sensitive to waveform geometry than pressure-induced flow. Combined EOF/PDF with favourable gradient suppressed recirculation, while adverse gradient induced it near wave crests. In the thermally developing region, Nu decayed rapidly due to boundary layer growth, while in the fully developed region, Nu oscillated. Thermal entrance length was longest for favourable and shortest for adverse gradient flows. Joule heating and geometry affected fully developed heat transfer.

25

Hasis et al. [150] numerically analyzed fully developed laminar flow and heat transfer in a twisted sinusoidal rectangular wavy microchannel with rotating cross-sections for Re = 300–700. The effects of twist ($\delta$), waviness ($\gamma$), and aspect ratio ($\beta$) were studied under constant heat flux and constant temperature conditions. Compared to sinusoidal microchannels, twisted designs showed up to 30% better heat transfer with minimal pressure drop at low Re, high AR, and waviness. Nu increased linearly with flow rate and waviness but declined with reduced twist. At higher Re and waviness, twisting showed limited benefits. Asymmetric corner vortices improved heat transfer performance. (Figure 2.3).
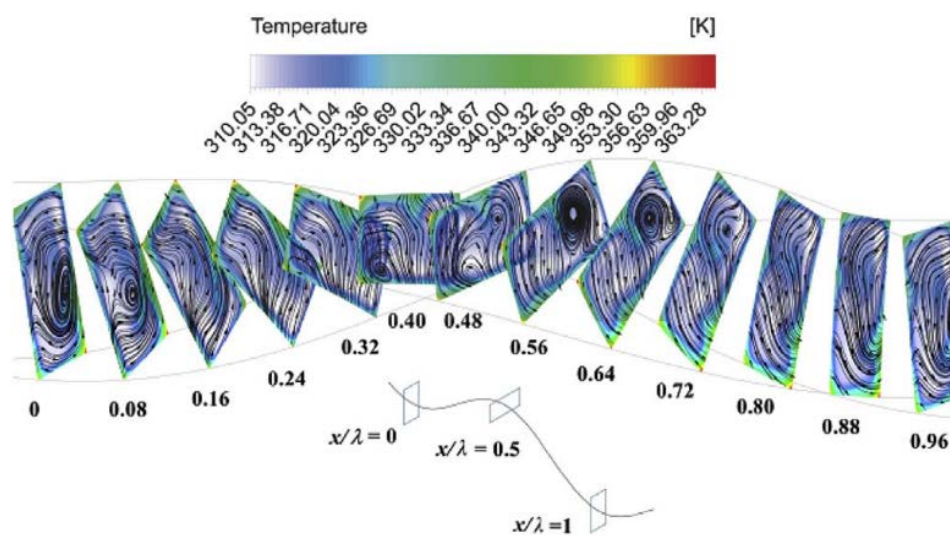


Figure 2.3 Depiction of progression of secondary flow structure with superimposed temperature field streamline in twisted wavy MCHS [150].
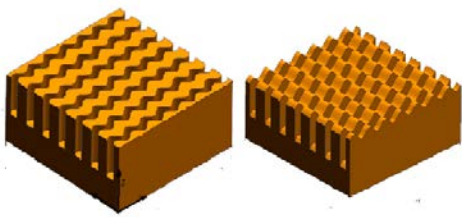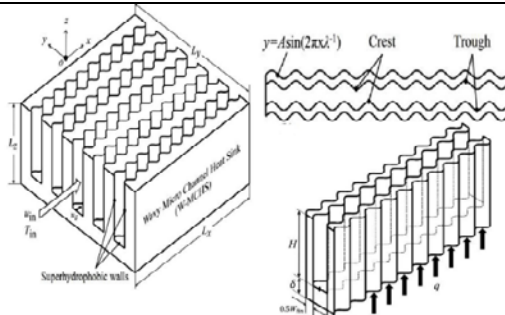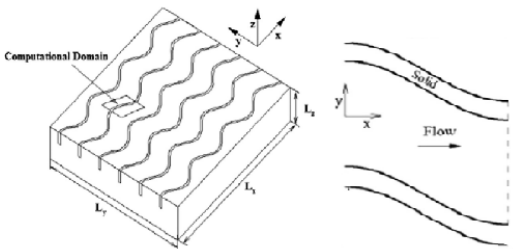
Numerical analysis of fully developed flow and heat transfer in periodic rectangular wavy MCHS [151] showed that secondary flows or Dean vortices formed at bends enhance mixing and heat transfer through chaotic advection in steady flow. As Re increased into the transitional range, the flow became unsteady, causing temporal and spatial evolution of Dean vortices and loss of symmetry. At higher Re, chaotic flow developed. Overall, wavy channels demonstrated significantly better heat transfer than straight channels of the same cross-section, without a notable increase in pressure drop.
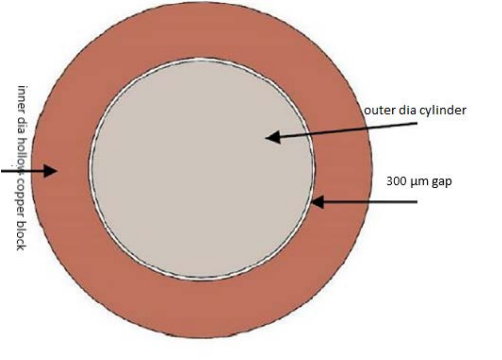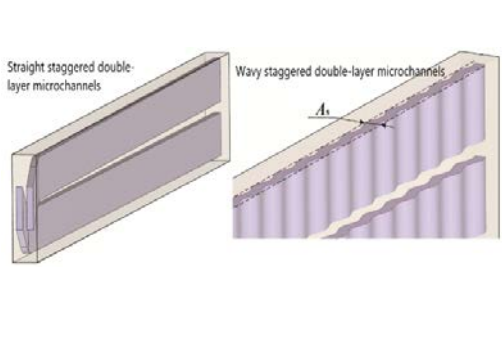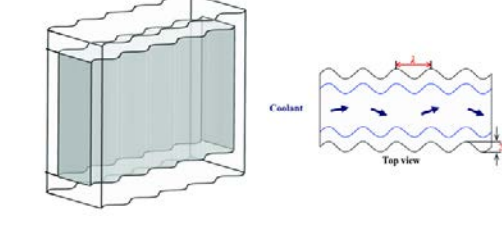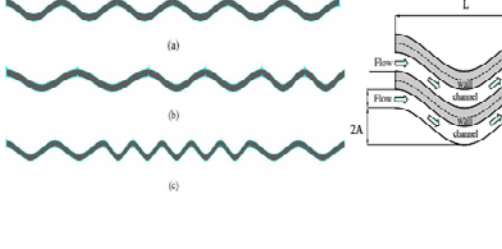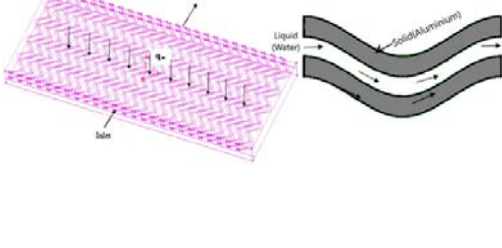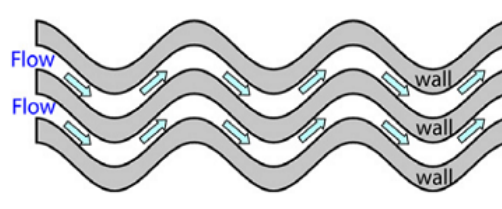
To enhance wavy MCHS performance, wavelength and/or amplitude were varied along the streamwise direction [152]. Reducing wavelength or increasing amplitude significantly improved performance by lowering thermal resistance (R) and bottom

26
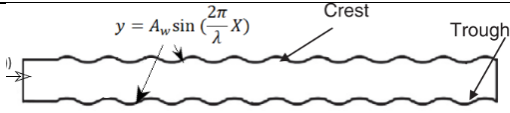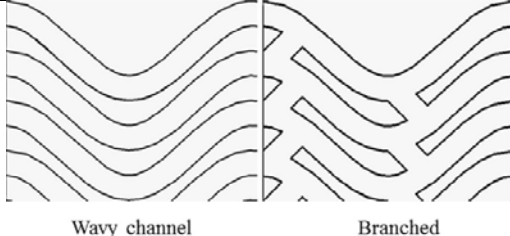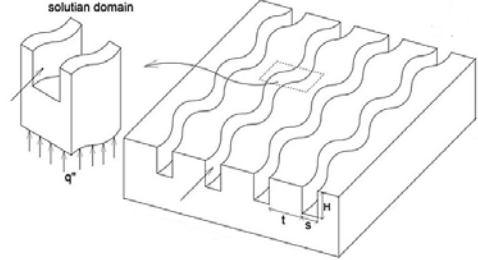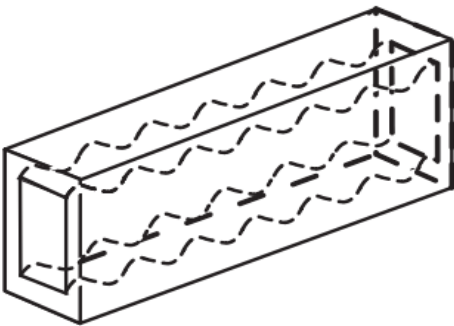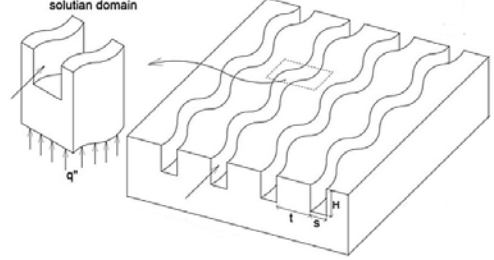
wall temperature difference ($\Delta T_{b,max}$), especially when differences in wavelength ($\Delta\lambda$) and amplitude ($\Delta A$) between units increased. Channels with lower aspect ratios showed reduced R and $\Delta T_{b,max}$ compared to both straight and conventional wavy MCHS.
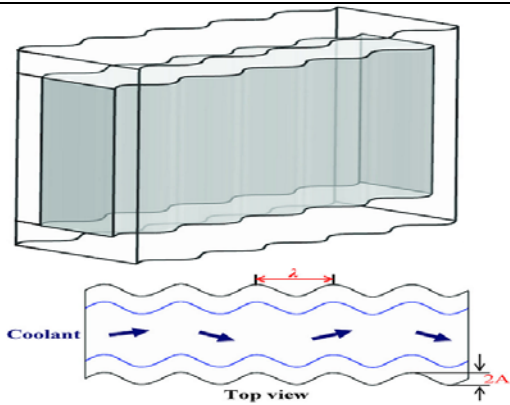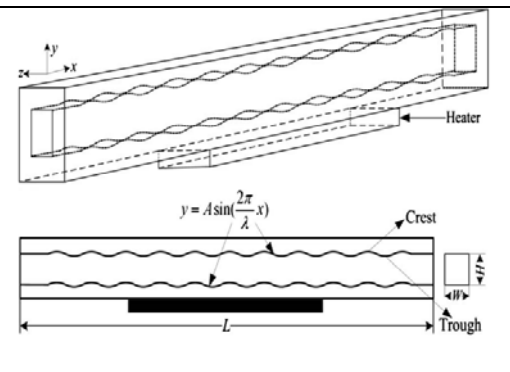
The thermal performance of up-down and left-right wavy MCHS was studied [153], showing improved heat transfer with minimal pressure drop. Both designs generated symmetric Dean vortices that enhanced coolant mixing. In up-down wavy channels, vortices formed near the sidewalls, while in left-right designs, they appeared near the top and bottom walls. Up-down wavy MCHS consistently outperformed left-right designs, although both showed similar performance at larger wavelengths. Table 2.1 summarises the various studies related to wavy shape of MCHS.

Table 2.1 Brief summary of work in wavy MCHS

| Author | Wavy pattern | C/S Material, Study type and input parameter | HT ↑↑ enhancement | PD penalty |
|---|---|---|---|---|
| Ji-Feng Zhu et al. [153] (2019) |  | Water/Silicon, CFD $T_{in}$= 300K, q =100 W/cm$^2$ | ~35% | |
| Hamidreza Ermagan et al. [154] (2018) |  | DI Water/ Silicon Numerical $u_{in}$= 0.6 to 1.4 m/s q= 100W/cm$^2$ $T_{in}$=293 K A= 15, 30, and 60 µm $\lambda$= 250, 500 and 1000 µm | 47.3% | 64.8% |
| Javad Rostami et al. [144] (2018) |  | -/Water-Cu/Al$_2$O$_3$ Nanofluid Numerical/ Fluent Dh=90 µm $\lambda$=200 µm | 174% | 195.7% |

27

| | | | | |
|---|---|---|---|---|
| Zi Hao Foo et al. [155] (2018) |  | -/Distilled water Exp and numerical Re= 1300–4600 Tin=321 K $\lambda$= 3, 6 and 10 mm A= 0.05, 0.10, and 0.15 mm | 51% | |
| Han Shen et al. [156] (2018) |  | Silicon/DI water numerical/Fluent q=100 W/cm$^2$ $u_{in}$= 1.32-2.6 m/s Re= 175-345 $\lambda$= 2.5 mm A 0-205 $\mu$m | 10% | |
| Xie et al. [157] (2017) |  | -/- Numerical/Fluent q=100 W/cm$^2$ $u_{in}$= 0.6-1.4 m/s Re= 96-223 $T_{in}$=293.15 k | 27.3% | 149.2% |
| Y. Sui et al. [139] (2010) |  | -/- Numerical/Fluent Re= 100–800, $\gamma$ ranging from 0.05 to 0.2, where $\gamma$=A/L q=300 W/cm$^2$ | 53% | 154% |
| H.A. Mohammed et al. [148] (2011) |  | Water/Aluminium numerical A= 125 to 500 $\mu$m Re=100 to 1000 $D_h$= 339.15 $\mu$m | 0.6% | |
| Y. Sui et al. [151] (2011) |  | Water/ Numerical/Fluent Re=50-175 | 278.6% | 51.8% |

28

| | | | | |
|---|---|---|---|---|
| Tapas K. Nandi et al. [158] (2013) |  $y = A_w \sin(\frac{2\pi}{\lambda} X)$ Crest Trough | Water/Silicon Numerical Re= 0.1 to 100 $A_{pulsation}$= 0.2, 0.5, 0.8 $0.1 < A < 1$ $T_{in}$=330K | 50% | |
| Lin et al. [159] (2016) |  Wavy channel   Branched | DI water/ Copper Re=50-200 Numerical/Fluent $\lambda$=3 mm A=450 µm V=0.1-1 l/min | 15% | 115% |
| Rostami and Abbasi [143] (2016) |  | Water-$Al_2O_3$ nanofluid/- $\varphi$= 0%-2% $\lambda$ =200 µm $D_h$=90 µm $T_{in}$=293K q= 100W/$cm^2$ | 162.6% | 195.7% |
| Sakanova et al. [160] (2015) |  | -/- Numerical/Fluent A= 25, 50 and 75 µm $\lambda$= 250 and 500 µm V= 0.152 l/min-0.354 l/min q=100 W/$cm^2$ | 13.9% | |
| Rostami et al. [161] (2015) |  | Water/ Silicon -/- Re=50-200 $D_h$=90 µm $\lambda$ = 200 µm Pitch of MCHS= 100 µm | 11.6% | 102.4% |

29

| Xie et al. [162] (2013) |  | -/- Numerical/Fluent $\lambda$=350 µm, 500 µm Re=100-230 $D_h$=160 µm q=100 W/cm$^2$ $u_{in}$=0.6-1.4 m/s | 15.6% | 185 % |
|---|---|---|---|---|
| Gong et al. [58] (2011) |  | -/- Numerical/Fluent Re= 50-150 q=47 W/cm2 $D_h$=500 µm A=50-200 µm $\lambda$=1.3-4 mm | 55% | 216.67 % |
| *Note: - C/S material: coolant and substrate material, f-pulsation frequency(Hz), q=heat flux (W/cm$^2$), A-Amplitude, $\lambda$-wavelength, $D_h$-Hydraulic Diameter, Re-Reynolds Number | | | | |

### 2.1.2 Serpentine MCHS

Al-Neama et al. [163] did an experimental and numerical study of serpentine rectangular MCHS with four different configurations, straight rectangular MCHS (SRMs), single (SPSMs), double (DPSMs), and triple path serpentine rectangular MCHS (TPSMs). When compared to the typical SRMs, SPSM achieves 35% gain in $Nu_{avg}$ and 19 % drop in total thermal resistance ($R_{th}$) at a volumetric flow rate of 0.5 l/min, but at the cost of 10 times drop in pressure.
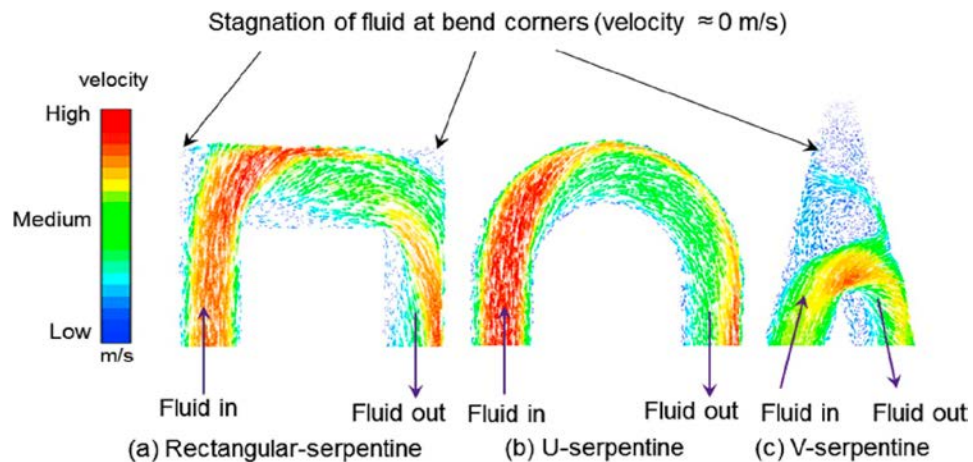


Figure 2.4 Stagnation zones are indicated by velocity profiles at the bends of various serpentine MCHS [164].

30

An experimental and numerical study using three serpentine MCHS shapes-Rectangular, U, and V-was conducted by Sreehari et al. [164] with silicon as the substrate and water as coolant over Re = 100–400 and heat fluxes of 10–30 kW/m². Thermal performance was governed by the Sink Area Factor (SAF), with higher SAF yielding better results. U-serpentine channels showed the best performance with low substrate temperature, high heat transfer coefficient, and minimal pressure drop, followed by rectangular and V-types. Sharp bends and surface roughness impacted performance, with V-serpentine performing worst due to stagnation zones and poor fluid mixing at corners (Figure 2.4).

A numerical study on fluid flow and heat transfer in serpentine MCHS with fan-shaped re-entrant cavities was performed for Re=150-980 [165]. Key geometric parameters included cavity width (Wc), height (Hc), and spacing (Sc), as shown in Figure 2.5a. These cavities reduce flow resistance and improve temperature uniformity. Dean vortices form within the cavities (Figure 2.5b), enhancing heat transfer by breaking and regenerating thermal and hydrodynamic boundary layers. However, stagnation zones from flow deflection can hinder performance. Overall, heat transfer improved, and flow resistance decreased, except at Re = 980 and Hc/Wc = 0.2887. Optimal performance was found at Sc/Wc = 3 and Hc/Wc = 0.2887.
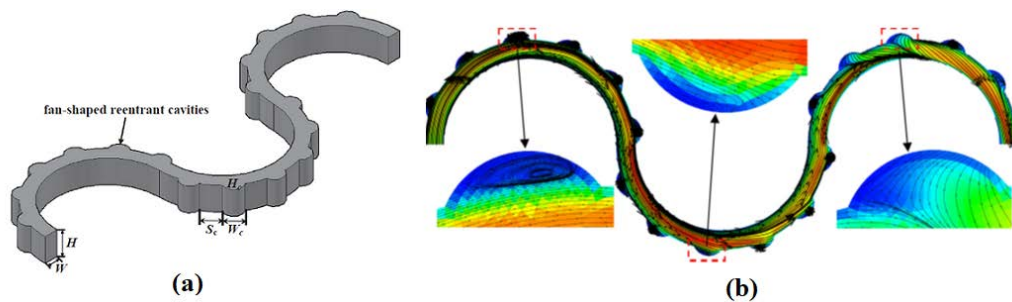


Figure 2.5 (a) Geometric parameters of serpentine MCHS with fan-shaped re-entrant cavities and (b) flow streamline at the mid plane for Re=480 [165].

An ANN and GA were used to optimize data from experimental and numerical studies of serpentine microchannels [166]. The ANN model showed higher accuracy, while GA-based empirical correlations were easier to apply.

CFD modelling was used to study the effect of cross-section orientation on serpentine equilateral triangular MCHS [167]. Channels with left-pointing triangles showed higher mean heat transfer than upward-pointing ones, with similar pressure drops for Re = 50–150. Twisted sections enhanced heat transfer with minimal pressure

31

increase, though the degree of twist had limited impact, except stronger twists improved heat transfer at downstream bends due to swirling flow. An experimental study using molecule-based temperature sensors evaluated segmented ethanol-air flows in serpentine MCHS [168]. At Re = 11, high gas flow and short liquid segments enhanced circulation, resulting in a 30% increase in Nusselt number.

### 2.1.3 Zigzag MCHS

Toghraie et al. [169] investigated the thermohydraulic performance of smooth, sinusoidal, and zig-zag shaped MCHS using nanofluids (water-CuO with φ=2% and 4%) for Re=100, 300, 900, and 1800. Effects of wavelength and amplitude, φ, and Re of sinusoidal and zig-zag MCHS on heat transfer performance were evaluated. Results show that with the increase in "φ" of CuO nanoparticle Nu increased. Effects of nanoparticles on the rate of heat transfer increment were more effective at Re=900 and 1800 than the Re= 100 and 300. Effects of nanofluid were more pronounced in smooth microchannel than sinusoidal MCHS. Nu increased with the decrease in wavelengths of sinusoidal and zig-zag shaped MCHS with zig-zag shaped MCHS being more appropriate compared to sinusoidal MCHS.

Duangthongsuk et al. [170] experimentally examined the thermal performance of two types of multiple zigzag flow channels namely continuous zigzag flow channel (CZ-HS) and the single cross-cutting zigzag flow channel (CCZ-HS). Nanofluid (DI water-SiO$_2$) with φ=0.3, 0.6, and 0.8 vol.% was used as working fluid and copper as substrate material. Results indicate that the 3-15% increment in TP was observed when nanofluid was used as a working medium. The CCZ-HS outperforms the CZ-HS by an average of 2–6% in terms of thermal performance. This could be because CCZ-HS divides the flow area into two parts when a single cross-cutting of the flow channel is used. Direct impingement of the fluid stream on the channel wall of the following region happens when the fluid flows past the first region. As a result, larger turbulent intensities are achieved, leading to improved HT performance. The pressure drop is moderately affected by particle concentration and flow channel cross-cutting.

### 2.1.4 Converging-Diverging MCHS

Another growing research area is a converging flow channel in the stream-wise direction. The convective heat transfer coefficient increases as the fluid velocity increases in the stream-wise direction of a converging channel. The MCHS's overall

32

temperature distribution and thermal resistance improve as a result of the reduced local wall temperature [171].

A tapered MCHS was designed to study the effect of height ($\Lambda y$) and width ($\Lambda z$) taper ratios on thermal performance [67]. The relationship between thermal resistance ($R_{th}$) and taper ratios was non-monotonic, with minimum $R_{th}$ at $\Lambda z = 0.6$ and $\Lambda y = 0.8$. Compared to parallel channels, width-tapered designs showed lower temperature rise and more uniform centerline temperature. A maximum thermal performance enhancement of 16.7% was achieved with width-tapered channels at pumping power > 0.4 W. Kumar et al. [176] used Water-$Al_2O_3$ nanofluid for the THP analysis of double-layered tapered MCHS (DL-MCHS). DL-MCHS was found to have better HT performance than the conventional channel but at the cost of increased PD penalty.

An experimental study found that highly-tapered MCHS induced early turbulence at lower Re, enhancing heat transfer but causing significant pressure drop [171]. All tapered MCHS had thermal performance (THP) less than one, indicating lower heat transfer efficiency than straight MCHS at equal pumping power. Straight MCHS also required less pumping power to remove the same heat at a given average Dh.

Heat transfer enhancement in MCHS with periodic expansion-constriction cross-sections was studied using rectangular (R), fan-shaped (F), and triangular (T) re-entrant cavities [51]. The Navier-Stokes equations were validated with entrance effects, temperature-dependent properties, and viscous heating. Compared to R, pressure drop was lower for F and T at Re < 300 but rose rapidly with increasing Re. Heat transfer improved significantly, with average Nusselt number increasing 1.8 times. As volumetric flow rate increased, the capacitive term decreased while the conductive term stayed constant, leading to reduced thermal resistance with higher pumping power.

### 2.1.5 Secondary flow microchannels

Secondary flows inside the flow field have been considered by many researchers to improve heat transfer. The geometry of MCHS can be altered by adding smaller channels in between the primary flow channel to create secondary flows (Figure 2.6). Kuppusamy et al. [172] designed a MCHS with slanted passage in the channel wall between the adjacent channels in alternating orientation. These passages cause flow disruption and decrement in thermal boundary layer. Overall performance of MCHS was reported to be increased by 146% and thermal resistance decreased by 76.8% as

33

compared to conventional MCHS. In contrary to the general research outcome, pressure drop decreased by 6% compared to its conventional counterpart. Thermal performance increment was more prominent at increased width of the secondary passage. The ratio of secondary channel width to MCHS width (α) was found to have a greater influence on the thermal resistance and pumping power [173]. Pumping power decreased by 13.7% and thermal resistance increased by 17.2% as the value of α increased from 1 to 2. Optimization of structural parameters played a significant role on the performance of MCHS with secondary flows.
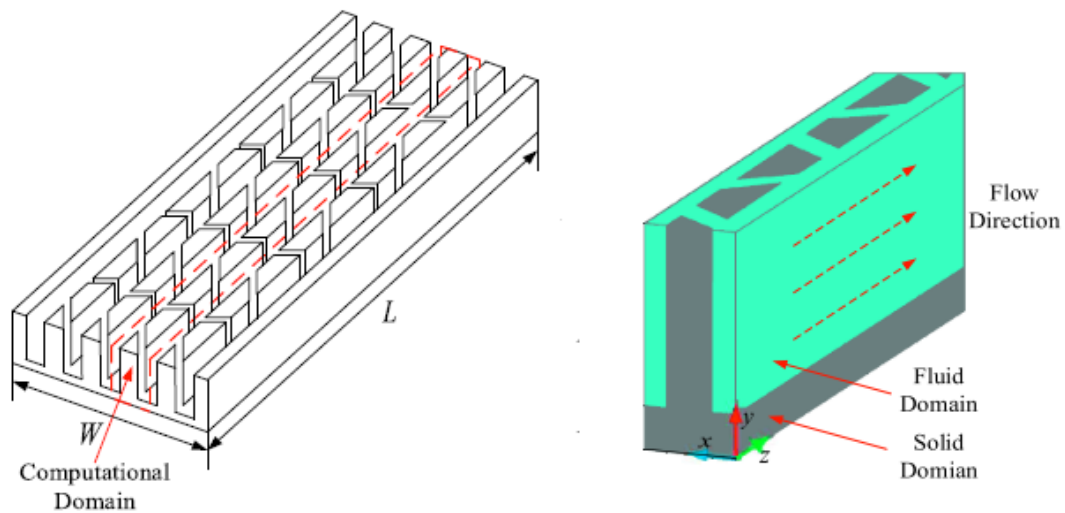


Figure 2.6: Schematic of Secondary flow channels (adapted from [173]).

## 2.1.6 Oblique finned microchannels

The purpose of employing an oblique fin in place of the continuous fin in MCHS is to modulate the flow. These oblique fins help to initialize the thermal and hydraulic boundary layer at the leading edge of the oblique fin and effectively thinning the boundary layer [174]. Because of these entrance effects, the flow is always in a developing state. Moreover, oblique fins also lead to diversion of a small fraction of flow from the main channel, thus creating secondary flows. These secondary flows provide better fluid mixing and hence enhancement in the heat transfer [175]. In another study, Law and Lee [176,177] revealed that the oblique fins inside MCHS helped to mitigate the instabilities related to two-phase flow along with the significant enhancement in heat transfer compared to straight finned MCHS. Far et al. [178] used Nano-Encapsulated Phase Change Material (NEPCM) as a coolant inside sectional oblique finned MCHS to analyze the pin tip-clearance effects on its thermal

34

performance. NEPCM slurry enhanced the cooling performance of MCHS with increased pumping power compared to pure water.

### 2.1.7 Transverse/Intersecting MCHS

As shown in Figure 2.7, In transverse MCHS, short and small microchannels join two or larger microchannels in transverse directions. These short channels divide the main flow into multiple paths and hence not letting the boundary layer grow in a thermally developing region by disrupting it which leads to high heat transfer than conventional microchannel. Moreover, the surface area to volume ratio is larger in the case of transverse MCHS than conventional MCHS. It has also been found to have a high heat transfer rate and low PD.

Heat transfer enhancement using transverse MCHS was numerically investigated by Soleimanikutanaei et al. [179]. The number and size of transverse MCHS at different Re determine the temperature distribution and hotspot location.
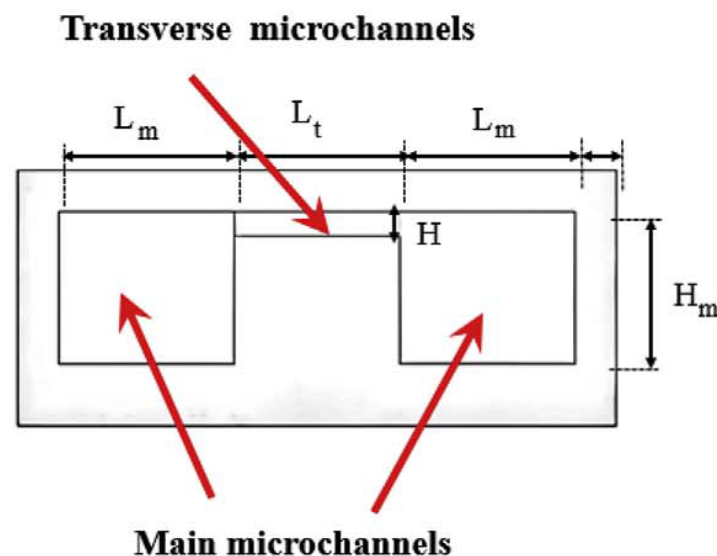


Figure 2.7: Schematic of transverse microchannel [179].

Nu increased with increase in number and decrease in height transverse microchannels at the expense of PD due to entrance effect (increased velocity) caused by the addition of transverse section. For narrower transverse microchannels, both heat transfer improvement and pressure drop were more evident. The figure of merit (ratio of HT to PD increase) increased with the increase in height and decrease in the number of transverse microchannel.

35

Wong and Lee [180] studied the thermal and hydraulic performance of MCHS by varying the geometrical parameters (length, width, and height) of the triangular rib of the transverse microchamber. The rate of heat transfer decreases with rib length but increases with rib width and height. The mean Nusselt number ratio demonstrates a 56 percent boost when compared to non-interrupted MCHS.

Chai and Wang [181] investigated the THP of interrupted transverse MCHS with ribs by considering viscous heating, entrance effect, and temperature-dependent thermophysical properties. Rectangular, backward triangular, diamond, forward triangular, and ellipsoidal rib configurations were used, and the rib geometry parameters comprised expansion-constriction profile length and ratio. When compared to straight MCHS, the interrupted MCHS with ribs in the transverse microchannel displays a 4–31% reduction in total thermal resistance, a 4–26% reduction in total entropy generation rate, and a PEC of a maximum of 1.39.

### 2.1.8 Double layered MCHS

The considerable temperature fluctuation within the heat sink between the inlet and outlet is one of the disadvantages of the single-layer channel layout. The resulting thermal stresses due to a high temperature rise cause thermal instability, as well as lower device performance and longevity, and hence, it is highly undesirable. While a single-layer MCHS with a high depth-to-width ratio can address this issue, it comes at a cost in terms of pumping power and fabrication complexity [182]. With this background, Vafai and Zhu [183] developed a double-layered heat sink structure to address these difficulties. They proposed that heat transferred to a double layered MCHS (DLMCHS) can be dissipated in two ways. One is the "direct path," in which heat from the base fin is first transferred to the lower layer through the bottom horizontal fin, and then dissipated by convection in the lower channels. The other is the "indirect path," in which heat is transferred to the upper layer via the vertical and middle horizontal fins, and then dissipated by convection in the upper channels. Here, the "indirect" path present in double-layered MCHS provides an extra benefit over single-layered MCHS. Figure 2.8 depicts the double layered MCHS.

An improved MCHS design with stacked double-layered rectangular channels-porous ribs in the upper and solid ribs in the lower layer-was proposed for enhanced TP and low PD [184]. Four other structures were compared: solid/porous-ribs in single/double-layered setups. The revised model showed the lowest thermal resistance

36

(reduced by 14.98%, 10.85%, 9.27%, and 11.44%) and best bottom wall temperature uniformity (improved by 52.44%, 58.04%, 14.57%, and 56.54%) at fixed Re or 0.05 W pumping power. This performance is attributed to better conductivity and low PD. Thermal resistance declined with increasing AR at constant channel-to-pitch width ratio and channel number.

Truncated DLMCHS was employed by Arani et al. [185] with water/single-wall CNT nanofluid as a coolant for Re in the range of 500, 1000, and 2000. Results show that this configuration led to better temperature uniformity and lower thermal resistance due to the use of water-CNT nanofluid. Up to 14% increment in thermal performance was observed for water-CNT nanofluid with non-Newtonian properties was observed by [186]. Leng et al. [187] observed that, apart from maintaining temperature uniformity at the base of the channel, truncated DLMCHS improved cooling performance at constant pumping power and volume flow rate of the coolant [188]. The average Nusselt number increased with decreased height and increased width of DLMCHS [189]. Mashayekhi et al. [190] used hybrid nanofluid in DLMCHS with sinusoidal walls. Hybrid Cu-Al2O3/water nanofluid was used for φ=0-2%. Nu was increased by 23%, 22%, 19% and 13% corresponding to Re=50, 300, 700 and 1200 at φ=2%.
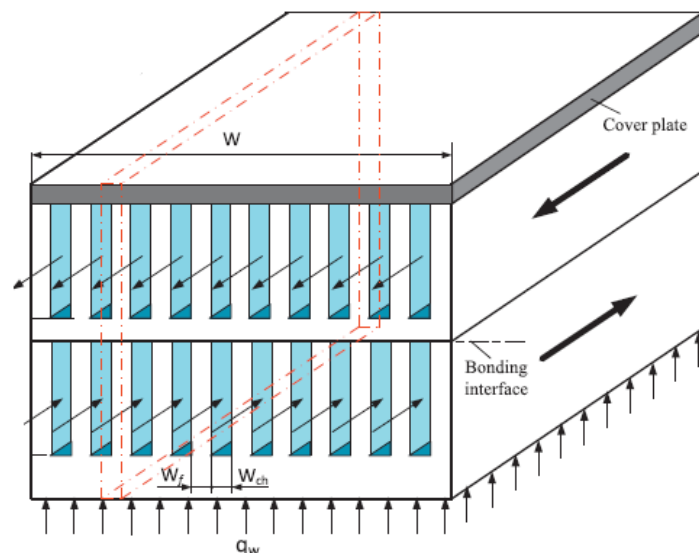


Figure 2.8 Schematic used in ref. [191] to describe double layered MCHS.

## 2.2    Fractal Microchannel Heat Sink

Many researchers have come out with different shapes and channel designs of FMCHS as depicted in Figure 2.9. Jing and co-workers [192,193] performed a comprehensive study for the optimization of a fractal tree-like network to obtain

37

minimum thermal resistance. For electrokinetic flow under the constant channel, volume constraints they found that the surface charge at the solid-liquid interface can significantly affect the optimal fractal network. In another study, they considered slip flow conditions for the investigation of Murray's law for laminar flow in a fractal tree-like network. The optimal diameter ratio for achieving minimum flow resistance was found to be dependent on slip length.
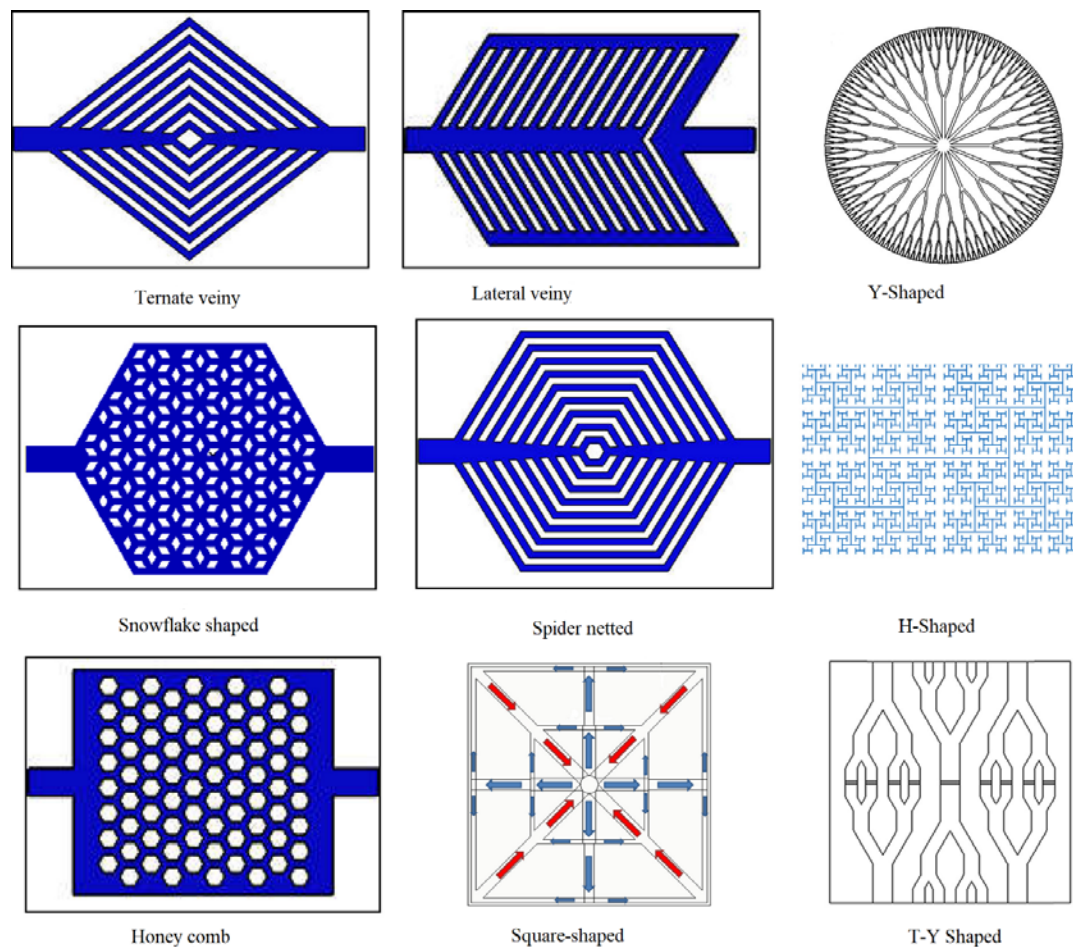


Figure 2.9: Various fractal shaped configuration [90,194–196].

In their experimental and numerical study of THP of fractal-like multilayer silicon MCHS. Xu et al. [197] discovered that layer number was an important factor in determining the Nu, pressure loss, and thermal resistance of the multilayer FMCHS. The use of a multilayer fractal MCHS results in lower thermal resistance and pumping power. MCHS performed best overall when the layer number was 5, with a small volume thermal resistance of 2.5 $Kcm^3/W$ and pumping power of 0.07 Watt at 400 ml/min.

The work of Ghodoossi [196] discovered that the thermal performance of fractal MCHS was unaffected, whereas hydraulic performance increased in the case of

38

turbulent flow and decreased for laminar flow compared to parallel MCHS. Zhang et al. [198] examined the formation of recirculation flow motions and secondary flows at the bends and bifurcation of fractal-like MCHS (Figure 2.10a). These motions, initiated at the L bend and T joints tend to substitute the slower moving fluid near the wall with faster-moving fluid as depicted in Figure 2.10(c-d), causing a great enhancement in viscous friction at the walls of the MCHS with large PD and enabling more convective thermal transport between fluid and walls of MCHS that led to better heat transfer.
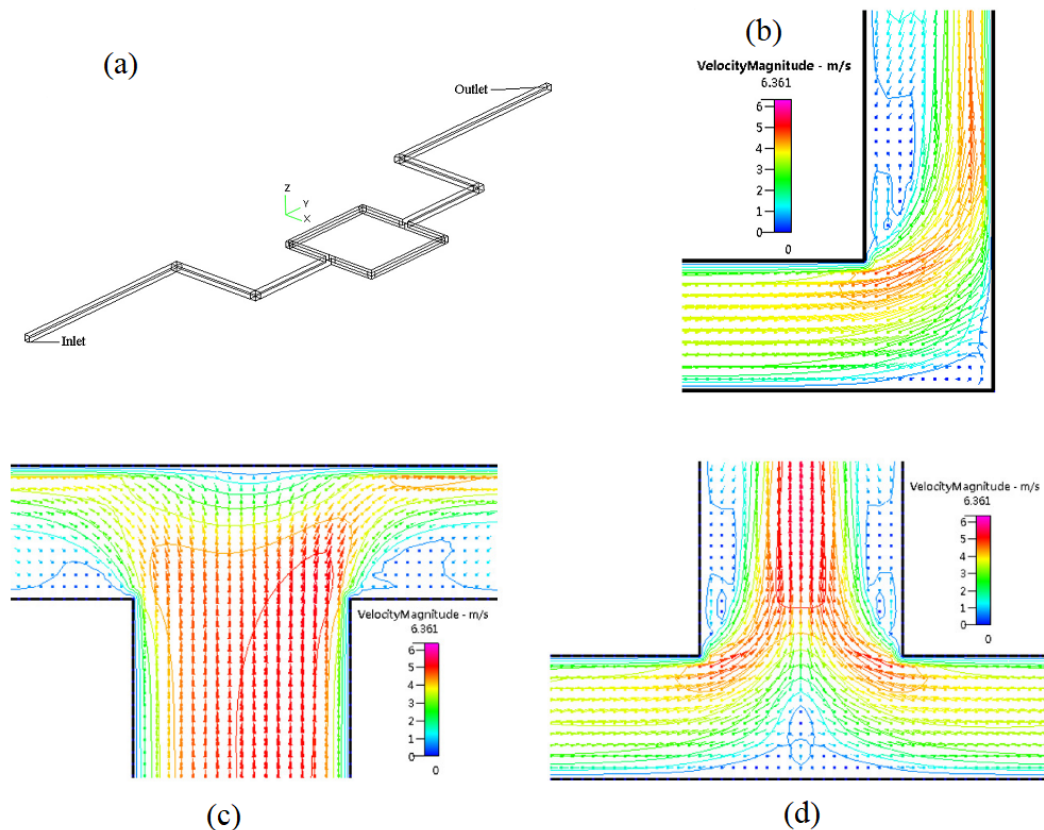


Figure 2.10. (a) Schematic of a fractal-like MCHS, Velocity distributions with an AR of 0.333 and Re=810 (b) L bend (c) diffluent flow at T joint and (d) confluent flow at T joint [198].

Heymann et al. [199] used a 1-D model to optimize the structure of fractal microchannels for the lowest PD and pumping power utilizing a direct numerical search and GA. Fewer branch levels with several channels originating from the input plenum were suitable for higher heat flux removal applications.

In another study, a truncated double-layered (TDL) heat sink along with Y-shaped fractal MCHS was investigated by [200]. TDL heat sink showed 24-30% improved

temperature uniformity at inlet than the simple double-layered (DL) channel with less requirement of pumping power.

Zhang et al. [201,202] numerically and experimentally analyzed the THP of fractal microchannel networks using the subsectional integral method, which showed lower deviation than the standard equivalent approach. Higher performance was observed for designs with smaller AR, higher fillet bends, and more branching levels. They found that flow rate and AR strongly influence vortex formation, enhancing mixing and heat transfer. Yu et al. [203] experimentally confirmed that fractal MCHS outperformed straight MCHS in heat transfer due to vortices, though at higher PD, especially at high Re due to losses at bifurcations—mitigated by using semi-circular bends. Senn and Poulikakos [204] showed that a 6-branch tree net had 50% lower PD than serpentine designs, with better thermal performance. Haller et al. [205] also reported high PD at L-bends and T-joints, suggesting shape modifications, albeit with reduced heat transfer. Shape and AR significantly affected PD.

Lu et al. [206] studied fractal heat sinks and found that increasing branching levels reduced average and peak temperatures, with level 4 being optimal, beyond which size constraints limited further gains. Right-angled bifurcations led to hotspots [194], resolved through design modifications that improved temperature uniformity, reduced thermal resistance, and lowered PD. Farzaneh et al. [207] showed that adding branches and loops decreased dimensionless temperature by 10–20% and PD by 25–30% compared to non-branching designs.

Yan et al. [208] developed a fractal MCHS with thermosensitive hydrogels for adaptive hotspot cooling via automatic flow redistribution. SFMHS 1+2 (hydrogels in both first and second-level branches) showed the least temperature rise due to superior flow modulation, followed by SFMHS 1 and SFMHS 2. SFMHS 1+2 required the highest pumping power but managed a wider heat flux range and effectively identified and cooled hotspots. Hotspot location significantly influenced hydrogel deformation and cooling performance.

Yan et al. [209] applied single and multi-objective evolutionary algorithms to optimize Y-shaped fractal MCHS topologies considering various geometric parameters. The Rt vs pumping power plot revealed two zones: an effective zone where structure depends on pumping power, and an ineffective zone where it does not. The hydraulically optimal model used 54.5–67.2% less energy with lower pumping power but had 50% higher thermal resistance than the thermally optimal model.

40

Table 2.2 summarises key findings from several studies related to fractal microchannel networks.

Table 2.2 Studies related to fractal shaped microchannel heat sink.

| Paper | Year | Configuration | C/S material | Flow conditions | % Increase in TP/ ΔP | Remarks |
|---|---|---|---|---|---|---|
| [210] | 2018 | FMCHS with pores | DI water/ Al | Laminar | ~17.27% (w.r.t. no pores)/- | Fractal Microreactor with a porous surface had better heat transfer performance. |
| [211] | 2015 | FMCHS | DI water /Si | Laminar<br>f= 0-40Hz<br>Re=1800-2800<br>q=40 W/cm$^2$ | 25-40% w.r.t. steady flow/- | Increase in heat transfer at low and high frequencies than at moderate frequencies. |
| [212] | | Y-FMCHS | Water/Cu | Turbulent<br>q=1-2.5 W/cm$^2$<br>$V_i$=0.6-1 l/min | -/- | Better temperature uniformity was obtained. |
| [213] | 2020 | leaf vein-shaped MCHS | Water/Al alloy | Laminar<br>$V_i$=0.4 L/min<br>q=100 W/cm$^2$ | -/- | The third-order assembly provides better temperature uniformity. |
| [214] | 2019 | Tree-shaped MCHS | Water/Cu | Laminar<br>q= 10 W/cm$^2$<br>Re=200-1000 | ~10.5%/14.2 KPa | Trees-shaped MCHS with ribs showed the highest HT performance |

41

| | | | | | | |
|---|---|---|---|---|---|---|
| [215] | 2020 | Rhombus-FMCHS | Water/Cu | Laminar $u_{in}$=0.25-2 m/s q=100 W/cm$^2$ Re=80-400 | 14.6%-29.4%/- | Rhombus FMCHS may increase the COP with increased cooling efficiency. |
| [216] | | FMCHS | CNT +Water& Kerosene/Si | Laminar Re=1500-3000 φ=0-8 vol. % q= 40 W/cm$^2$ | 108%/- | Nu of SWCNT nanoparticles is significantly higher. The water-based nanofluid's PEC is higher |
| [217] | 2019 | FMCHS | Al2O3-water and SiO2-water/- | Laminar q= 50 W/cm$^2$ $u_{in}$= 4-9 m/s φ= 0% to 4% | 8.3%/327.29 kPa | Al$_2$O$_3$-water has a higher mean HT coefficient, PD, lower base temperature than SiO2-water. |
| [218] | 2017 | T-Y-shaped FMCHS | liquid GaInSn/Cu | q=100 W/cm$^2$ Re=1021-6126 $u_{in}$=0.4-2.4 m/s Laminar and turbulent | 271.46% compared to water for GaInSn/22.1 kPa | The optimal bifurcation angle was found to be 60º where Nu is highest with the least PD. |
| [219] | 2009 | Tree-shaped MCHS | DI Water/Al | $D_h$=4mm q=2.5W/cm$^2$ Re=600-1500 | 110.38% increase in COP compared to serpentine MCHS at | Uniform temperature distribution and less PD compared to serpentine MCHS. |

42

| [220] | 2015 | Tree-shaped FMCHS | Water/Steel | q=25 W/cm$^2$ Re=600-1000 laminar | 132.98% more COP than helical net at Re=600/1.3 kPa | Fractal tree-like MCHS has lower PD, more uniform temperature distribution, and larger COP Helps in hotspot mitigation |

*Note: - HT: Heat Transfer, Pressure Drop, C/S material: coolant and substrate material, TP: Thermal Performance, Al-Aluminium, Si-Silicon, Cu-Copper, f-pulsation frequency(Hz), q=heat flux (W/cm$^2$)

## 2.3    Other modifications in shape

Apart from above-mentioned modification, some other techniques are being used for the thermal performance enhancement of MCHS. However, these are very uncommon and have not been studied by many researchers.

Brinda et al. [221] investigated ladder-shaped MCHS for enhancing contact area with the flowing coolant. By employing ladder-shaped MCHS with rectangular cross-sections helped in decreasing thermal resistance and increasing thermal performance.

Temperature uniformity is vital for microelectronic reliability. Stepwise varying channels improve thermal performance and uniformity without significant pressure drop. A stepwise varying width microchannel [222] showed a threefold increase in thermal resistance coefficient at the same mass flow rate. The TIM layer enhanced temperature uniformity by raising average temperature, prompting design changes considering TIM effects.

Luo et al. [7] studied brass Honeycomb porous MCHS to understand HT characteristics and cooling performance. Metal etching was used for the fabrication. The result show that it removed 18.2 W/cm$^2$ of heat flux at 2.4 Watt of pumping power. Tang et al. [223] designed a ring-shaped MCHS by turning process with added guide vanes to enhance uniformity in flow distribution in microchannels. Flow distribution uniformity was achieved in this configuration.

Microchannels with oblique fins [175], dimpled or protruded surfaces [224,225] have also been shown to improve heat transfer across the channel by generating secondary flows.

43

## 2.4    Nanofluids

Dispersing metallic or non-metallic nanoparticles with a high thermal conductivity into conventional fluids like water, ethylene glycol, or oils creates nanofluids, a special kind of heat transfer fluid. These nanoparticles, which are usually between 1 and 100 nanometers in size, improve the base fluid's thermal characteristics and efficiency of heat transfer. Because of this, heat exchangers, cooling systems, and other thermal management technologies can benefit from using nanofluids. Table 2.3 shows various nanoparticles' thermo-physical properties and their cost analysis.

Over the past several years, nanofluids, which are two-phase systems consisting of a base fluid and nanoparticles suspended in the fluid, have garnered substantial attention in the fields of biomedicine and industry [226]. They are widely used for cooling microdevices, targeted medication delivery, and blood component separation [227]. Because of their improved heat transfer capabilities, nanofluids in particular are thought to hold great promise for thermal management in cutting-edge electrical and biological systems.

Better thermohydraulic performance is necessary for these applications in order to ensure uniform distribution of nanoparticles, increase process efficiency, and optimise performance. Table 2.4 summaries the nanofluid analysis on hydro-thermal performances.

Table 2.3 Thermal-physical properties of nanoparticles and their cost analysis challenges.

| Nanoparticles | $\rho$ (kg.m$^{-3}$) | $C_p$ (J.kg$^{-1}$K$^{-1}$) | K (W.m$^{-2}$k$^{-1}$) | Quantity(g) | Cost (Rs) |
|---|---|---|---|---|---|
| CuO | 6510 | 540 | 76 | 5 | 3111 |
| $Al_2O_3$ | 3880 | 729 | 42.3 | 25 | 2000 |
| $TiO_2$ | 4175 | 692 | 8.5 | 100 | 12859 |
| $SnO_2$ | 2220 | 745 | 36 | 25 | 1500 |
| ZnO | 5610 | 494 | 29 | 100 | 1500 |
| $Fe_3O_4$ | 4950 | 640 | 7 | 25 | 1750 |
| Ag | 10500 | 230 | 424 | 5 | 12917 |
| Au | 19300 | 129 | 315 | 1 | 35029 |
| CNT | 1350 | 3900 | 3000-6000 | 250 | 19521 |

44

Table 2.4 Hybrid- nanofluids on hydrothermal performance

| Fluid Base | Nanoparticles | Concentration | Remarks | References |
|---|---|---|---|---|
| **Distilled Water** | $Al_2O_3$, CuO, $SiO_2$ and ZnO | 1-5 % | The volume fraction of particles increases, viscosity also increases. However, as temperature rises, viscosity decreases. Nanoparticles' shape significantly influences thermal conductivity (k) and viscosity. | [228] |
| **Water** | $TiO_2$ | 0.2 % | Models have been used to analyze the thermophysical properties, including viscosity, specific heat, and thermal conductivity. It was found that at very low concentrations, these properties have minimal impact on the heat transfer coefficient of nanofluids. | |
| **Water** | Zn and $Fe_2O_4$ | 0.02-0.5 % | The heat transfer coefficient and thermal conductivity increased by 42.99% and 11.8%, respectively, at a 0.5 weight concentration of Zn ferrite nanofluids. | [229] |
| **Deionized Water and EG** | Al2O3 and CuO | 0.05-0.75 % | Deionized water (DW) is used as the host fluid to decrease viscosity while enhancing electrical conductivity. | [230] |

45

| Water | ZnFe2O4, MnFe2O4, NiFe2O4 | - | Ternary nanoparticle-based heat transfer liquids offer better thermal dispersion in fins than mono nanofluids | [231] |
|---|---|---|---|---|

To get over the drawbacks of traditional microchannel heat sinks, engineers and researchers are constantly creating novel thermal management techniques. In order to optimise heat transfer and nanoparticle dispersion within the coolant flow, these include sophisticated geometrical designs, passive and active augmentation techniques, and the application of external forces like electric or magnetic fields. Improvements in mixing efficiency brought about by developments in microfluidic technology and nanofluid engineering eventually result in enhanced performance in targeted medication therapies, biological diagnostics, and next-generation electronic device cooling systems.

## 2.5     Summary of literature review

The efficiency of microchannel heat sinks in transferring heat and fluid has been the subject of numerous research, particularly when the geometry of the sinks changes, such as when they are square, rectangular, wavy, serpentine, convergent-divergent, or fractal. Conduction and forced convection are the primary means of heat dissipation due to laminar flow, and viscous effects are the most significant at the microscale. Thus, the effectiveness of cooling is greatly influenced by the channel's design. Because of their self-similar hierarchical branching structure, fractal microchannel heat sinks (FMCHS) offer potential for enhancing thermal performance without appreciably increasing pumping power.

Simple-shaped microchannel heat sinks may require longer flow paths or higher flow rates to remove sufficient heat since turbulence is reduced and viscous effects are more pronounced. Usually, this results in greater drops in pressure. Thermal-hydraulic performance is measured using the performance evaluation criteria (PEC). In fractal designs, branching creates a more uniform coolant distribution, reducing hotspots while maintaining an appropriate pressure drop. Through finer branches, fractal forms increase surface area contact. By doing this, heat transfer is enhanced without requiring large flow rates.

46

Rheological behaviour of nanofluids significantly influences the flow of heat via MCHS. Because fractal geometries have sharp angles and smaller cross-sections, they may strengthen chaotic advection and aid in mixing and heat exchange.

Numerical simulations of microchannel heat sinks are particularly prone to errors when predicting temperature gradients and local heat fluxes. These inaccuracies result from approximations made when breaking things down into smaller components, which may cover up thermal contours and lead to over- or under-predictions of local Nusselt numbers and overall efficacy. This is particularly crucial for 3D FMCHS simulations since the intricate shapes require high-resolution schemes and accurate grids. To ensure that the simulation results are correct, it is crucial to verify the results of grid independence studies and numerical simulations.

The choice of meshing strategy, solver schemes, and boundary conditions have a significant impact on how accurately thermal performance estimates turn out. Additionally, most current models assume steady-state flow conditions, meaning they do not account for the transient generation of heat that may occur in periodic or pulsating flow regimes. Finding thermal response delay, flow redistribution effects, and transient hotspots for FMCHS requires time-dependent numerical research, particularly when load conditions shift in the real world.

A variety of techniques, such as wet and dry etching, laser micromachining, lithography-based moulding, and additive manufacturing, can be used to create microchannel heat sinks. Due to its affordability and flexibility, soft lithography using materials like polydimethylsiloxane (PDMS) is one of the most often used prototyping techniques. The thermal conductivity of PDMS-based heat sinks can be increased by adding nanoparticles such as metal oxides or carbon nanotubes, which makes them suitable for moderate thermal applications. Additionally, altering the nanoparticle dispersion can alter the channel walls' hydrophilic or hydrophobic properties, which influences the formation of the thermal boundary layer.

Heat sinks with intricate designs, such as wavy, serpentine, or fractal patterns, can now be quickly created via additive manufacturing. 3D printers can print complex designs directly, including structures with multiple layers or integrated pieces, albeit they might not be as precise as lithography-based techniques. This gives thermal management systems a number of new options. Printing structures composed of many materials with high microscale precision is still challenging, though.

47

## 2.6      Research gaps

Numerous researchers have explored various microchannels geometries, including square microchannels, wavy MCHS, Serpentine MCHS, curved microchannels, zigzag microchannels, convergent-divergent microchannels, double layered MCHS, helical MCHS, Hierarchical MCHS, tree-shaped MCHS, Fractal MCHS and more. The primary objectives of these studies are to achieve better thermohydraulic performance and minimize pressure drop across a range of Reynolds numbers.

Additionally, numerical analyses have examined the influence of several parameters, such as fluid properties, inlet velocities, microchannel cross-sectional dimensions, and heat flux, on thermohydraulic performance. Various studies have also plotted relationships such as flow rate vs. Nusselt number, pressure drop vs. flow rate, temperature gradient along the channel length, temperature distribution on the base of the channel.

Obstacle-based microchannels have also been proposed, incorporating structural elements such as cylindrical, square, rectangular, and triangular obstacles and microchannels with patterned ribs and cavity. Simulation results indicate that thermohydraulic performance improves with an increased number of obstacles.

Despite extensive research, several gaps remain in the literature:

i.    Limited studies have focused on fractal shaped microchannels with reentrant obstruction in the form of ribs and cavities.

ii.   Research on optimization study on Fractal MCHS

iii.  Limited studies on the influence of nanofluid in the Fractal MCHS performance

## 2.7      Research objectives

The present study aims:

i.    To numerically investigate the fractal-shaped microchannel with re-entrant obstruction.

ii.   To investigate the thermohydraulic performance of microchannels integrated with re-entrant obstructions using nanofluid under different flow conditions.

iii.  To optimise the thermohydraulic performance of re-entrant fractal-shaped microchannel heat sinks.

48

# Chapter 3 METHODOLOGY

This chapter establishes the fundamental principles governing fluid flow and heat transfer in microchannel heat sink (MCHS), focusing on both water and nanofluid as working fluid. The study begins with the selection of microchannel geometries, including simple rectangular, fractal microchannel heat sink (FMCHS), FMCHS with ribs and cavities, followed by defining channel dimensions, inlet/outlet configurations, and boundary conditions. A structured meshing approach is employed, with a grid independence study to ensure numerical accuracy.  The governing equations, including the Navier-Stokes, energy equation and continuity equations, are implemented to describe fluid flow and heat transfer. Thermohydraulic performance is evaluated using key metrics like the Nusselt number, performance evaluation criteria (PEC), Thermal resistance, pumping power and pressure drop.

Computational Fluid Dynamics (CFD) simulations are conducted using an appropriate solver, applying numerical discretization methods and varying flow rates to study flow characteristics. Validation of the numerical results is performed by comparing with experimental data or benchmark studies. To optimize FMCHS performance, multiple strategies are employed. Geometric optimization involves refining channel structures to enhance thermohydraulic performance while minimizing energy losses. Multi-objective optimization techniques, such as Moth flame optimization and Response Surface Methodology, are utilized to maximize Nu, while reducing pumping power and thermal resistance. Additionally, the influence of nanofluids is analysed by adding nanoparticle concentration for enhanced heat transfer without significantly increasing viscosity.

Finally, a detailed performance evaluation is conducted by comparing different FMCHS configurations based on thermohydraulic performance indicator.

## 3.1    Flow in minichannel and microchannel

Microchannels are used in several single-phase liquid flow technologies. Among the earliest uses were micromachined devices like microsensors, micropumps, and microvalves. Analysis of biological materials, including proteins, embryos, DNA, cells, and chemical reagents, became important as a result of advancements in the biological sector and life sciences. The field of micromixers acquired prominence with the invention of microreactors, which blend two chemical species before

53

introducing them into a reaction chamber. The substantial heat loss from high-speed microprocessors prompted research on heat transfer in microchannels.

### 3.1.1   Fundamental issues in fluid flow in microscale

Innovations in microelectromechanical devices must be combined with compact heat removal technologies. Mirrors used in high-power laser systems must be cooled using low-footprint cooling technologies. Precision temperature control and regulated fluid flow in channels with a diameter of several micrometres are necessary for developments in genetic engineering and biomedicine. Designing and running these microscale systems requires a thorough understanding of fluid dynamics and heat transport.

### 3.1.2   Need for a smaller channel

Three main factors have contributed to a reduction in flow passage diameters in convective heat transfer applications:

i. Improved heat transfer.

ii. Improved microelectronic device thermal flux dissipation.

iii. Cooling solutions are required as microscale devices become more common.

Smaller channel widths increase heat transfer efficiency even when there is a larger pressure drop per unit length. Higher volumetric heat transfer densities necessitate more intricate manifold designs and sophisticated production processes. For each application, the optimal balance results in differentiable channel sizes. In the refrigeration business, larger plain tubes have been replaced by microfin tubes with 6 to 8 mm diameters, which, when paired with external copper heat sinks, result in temperature differentials that are sometimes as tiny as a few degrees Celsius. In order to allow fluid to circulate away from the heat source, the channel needs to be considerably smaller and fitted with the appropriate coolant loop devices due to the high heat dissipation. In automotive applications, radiator and evaporator channel sizes have exceeded a threshold of 1 mm, balancing the system's requirements for pumping power, heat transmission, and general cleanliness. Microelectronic devices, which cover a broad range of applications such servers, personal computers, laser diodes, and radio frequency devices, are continuously increasing the requirements for heat flux density. The 200 W/cm$^2$ heat dissipation threshold was considered unreachable in the late 1990s, but it appears to be a realistic objective presently. Over

54

the next decade, 600–1000 W/cm² will be the difficulty. The available temperature A cooling system for a microscale device can need cooling channels that are many tens of micrometres in size, in contrast to conventional channels with flow lengths of 1 to 3 mm. Many of these devices can also be combined, and heat can be dissipated using a secondary cooling loop in addition to a traditional cooling system.

A schematic illustration of a microchannel cooling system intended for server application cooling is shown in Figure 3.1. The cooling requirements of high-performance servers will be effectively met by the integration of (i) microchannel heat exchangers affixed directly to the chip or within the chip-bonded heat sink; (ii) water-cooled cold plates featuring minichannel or microchannel flow pathways; and (iii) supplementary localised cooling systems. According to Kandikar [232], the building's HVAC system incorporates the cooling system.
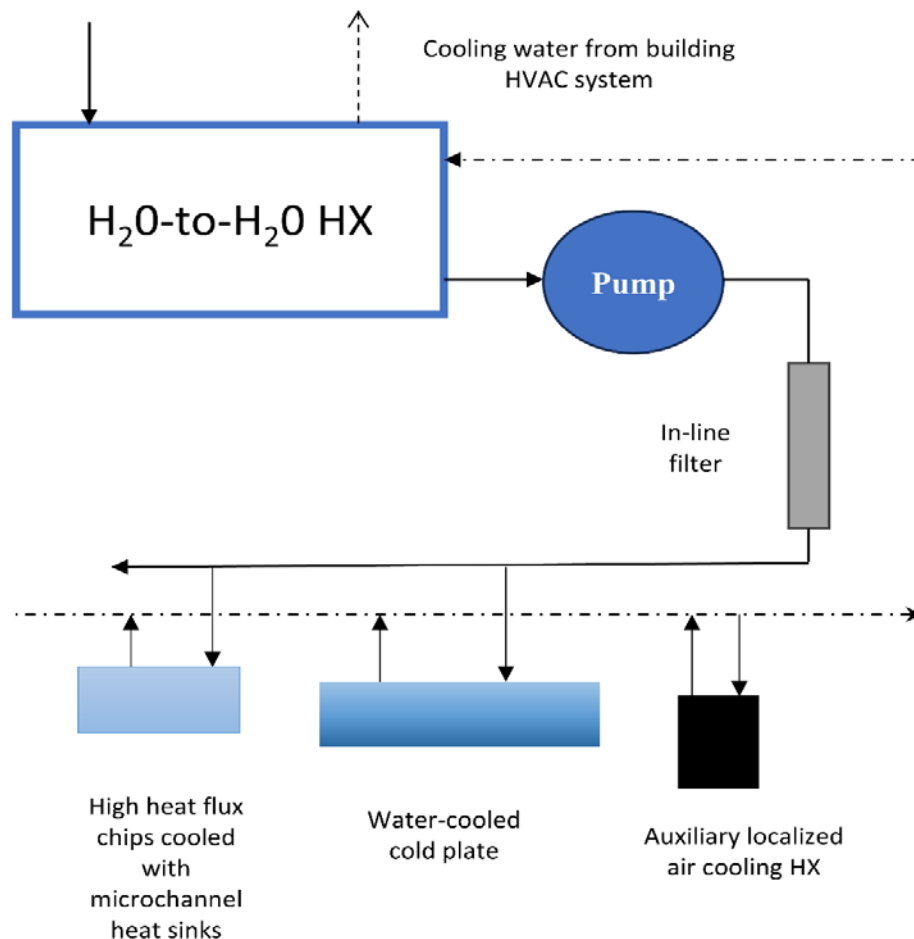


Figure 3.1 An illustration of a server cluster with MCHS, cold plates, localised air cooling, and a supplementary chilled water loop from the building's HVAC system to cool high heat flux CPUs.

## 3.2      Pressure drops in single-phase liquid flow

### 3.2.1 Fundamental pressure drop relation

To find out how pressure drops in interior flows, we begin with the one-dimensional motion of an incompressible fluid in a smooth circular tube. The following equations are easily obtained assuming that microchannels are continuous and that Newtonian fluid flows in them.

In analysing the equilibrium of a fluid element of length dx within a pipe of diameter D, the force resulting from the pressure differential $d_p$ is counterbalanced by the frictional force arising from the shear stress $\tau_w$ at the wall.

$$\frac{\pi}{4}D^2(-dp) = \pi D dx \, \tau_w \tag{3.1}$$

The subsequent equation consequently connects the pressure gradient and wall shear stress.

$$\frac{dp}{dx} = -\frac{4\tau_w}{D} \tag{3.2}$$

The velocity gradient at the wall determines the wall shear stress, represented by the symbol $\tau_w$, for Newtonian fluids, where $\mu$ is the fluid's dynamic viscosity. The Fanning friction factor f is used in the literature on heat transfer because it can accurately depict the fluid flow's momentum transfer process in a way that is consistent with the representations of heat and mass transfer processes.

$$\tau_w = \mu \frac{du}{dy}\Big|_w \tag{3.3}$$

The frictional pressure drop $\Delta p$ over a length L is obtained from Eqs. (3.2) and (3.4), respectively:

$$f = \frac{\tau_w}{\frac{1}{2}\rho u_m^2} \tag{3.4}$$

$$\Delta p = \frac{2f\rho u_m^2 L}{D} \tag{3.5}$$

The f in Eq. (3.5) is contingent upon the flow circumstances, channel wall geometry, and surface characteristics.

  i.      Flow-channel shape,

  ii.     Laminar or turbulent flow,

  iii.    Smooth or rough walls,

56

iv.     Fully formed or developing flow.

In noncircular flow channels, the D in Eq. (3.5) is substituted by the hydraulic diameter $D_h$, defined by the subsequent equation.

$$D_h = \frac{4A_c}{P_w} \tag{3.6}$$

where $A_c$ is the flow-channel cross-sectional area and Pw is the wetted perimeter. For a rectangular channel of sides, a and b, $D_h$ is given by

$$D_h = \frac{4ab}{2(a+b)} = \frac{2ab}{a+b} \tag{3.7}$$

### 3.2.2 Fully developed laminar flow

It is feasible to rapidly identify the velocity gradient at the channel wall by utilising the well-established Hagen-Poiseuille parabolic velocity profile for fully developed laminar flow in a circular pipe.   Based on the velocity profile, the equations (3.3) and (3.4) are utilised to get the values of $\tau_w$ and f.  The friction factor f is expressed in the subsequent format:

$$f = \frac{\text{Po}}{Re} \tag{3.8}$$

Where Po represents the Poiseuille number, defined as,

$$\text{Po} = fRe = 16 \tag{3.9}$$

which is contingent upon the geometry of the flow channel.  Table 3.1 presents the f Re product for various duct geometries, as calculated from Hornbeck et al.  [233].

$$fRe = 24(1 - 1.3553\alpha_c + 1.9467\alpha_c^2 - 1.7012\alpha_c^3 + 0.9564\alpha_c^4 \\ - 0.2537\alpha_c^5) \tag{3.10}$$

It is evident that for a circular channel, Shah and London [234] presented the equation for a rectangular channel characterized by a short side a and a long side b, with the channel aspect ratio specified as $\alpha_c = a/b$.

### 3.2.3 Developing laminar flow

The velocity profile progressively changes as fluid enters a duct, eventually attaining the fully formed Hagen-Poiseuille velocity profile over the duct's length. The velocity condition at the entrance is assumed to be uniform in the great majority of evaluations that have been reported in the literature. The length of the hydrodynamic

57

development region, represented by $L_h$, can be calculated using the following well-known formula:

$$\frac{L_h}{D_h} = 0.05 Re \tag{3.11}$$

Because small-diameter channels have higher pressure gradients, the flow lengths in these channels are often shorter. In many different applications, the length of the channel in the expanding zone makes up a significant portion of the flow length inside a microchannel. The pressure drop equations are expressed with an apparent friction factor to account for the developing region.

The friction factor that was observed $F_{app}$ assesses both the effects of the developing region and the pressure loss due to friction. The average friction factor value over the flow length from the entrance section to the specified endpoint is shown in the statement. The pressure drop in a channel characterised by a hydraulic diameter $D_h$ over a length x from the entrance is expressed as:

$$\Delta p = \frac{2 f_{app} \rho u_m^2 x}{D_h} \tag{3.12}$$

The disparity between the perceived friction factor over a length x and the fully developed friction factor f is articulated in relation to an incremental pressure defect $K(x)$:

$$K(x) = \left( f_{app} - f \right) \cdot \frac{4x}{D_h} \tag{3.13}$$

For x>.$L_h$, the incremental pressure defect reaches a constant value $K(N)$, referred to as Hagenbach's factor.

$$\Delta p = \frac{2 (fRe) \mu u_m x}{D_h^2} + \frac{K(x) \rho u_m^2}{2} \tag{3.14}$$

By integrating Eqs. (3.12) and (3.13), the pressure drop can be articulated in relation to the incremental pressure decrease.

Chen et al. (1964) [233] derived the axial velocity distribution and pressure drop for a circular tube in a nondimensional format. He projected that the completely formed zone commences at x150.0565, with a $K(N)$ value of 51.28 for a circular duct. They provided the subsequent equation for $K(N)$ in circular geometry:

58

$$K(\infty) = 1.20 + \frac{38}{Re} \tag{3.15}$$

Shah and London (1978) [233] demonstrated that the frictional pressure drop in the developing zone of a circular duct, as derived by Hornbeck [233], may be precisely represented by the following equation:

$$\frac{\Delta p}{\frac{1}{2}\rho u_m^2} = 13.74 x_1^{1/2} + \frac{1.25 + 64 x_1 - 13.74 x_1^{1/2}}{1 + 0.00021 x_1^{-2}} \tag{3.16}$$

Rectangular geometries are very significant in microfluidic applications.

$$K(\infty) = 0.6796 + 1.2197\alpha_c + 3.3089\alpha_c^2 - 9.5921\alpha_c^3 \\ + 8.9089\alpha_c^4 - 2.9959\alpha_c^5 \tag{3.17}$$

Phillips [235] examined the existing data, including that by Curr et al. [235], and aggregated the findings for the apparent friction factor in a rectangular duct. Fully developed flow is achieved at various x1 values, with low-aspect-ratio ducts attaining it sooner. The constant 0.05 in Equation (3.11) is adjusted to approximately 1 (x15100) for fully developed conditions in rectangular ducts.

### 3.2.4 Fully developed and developing turbulent flow

Numerous correlations with similar accuracies exist in the literature for fully developed turbulent flow in smooth channels. The equation proposed by Blasius is often utilised.

$$f = 0.0791 Re^{-0.25} \tag{3.18}$$

Phillips [235] proposed a more precise equation that encompasses both the developing and fully developed flow areas. He articulated the Fanning friction factor for a circular tube using the following equation:

$$f_{\text{app}} = ARe^B \tag{3.19}$$

$$A = \frac{0.092901}{1 + 1.01612 \cdot (x/D_h)} \tag{3.20}$$

$$B = \frac{0.26800}{1 + 0.32930 \cdot (x/D_h)} \tag{3.21}$$

In rectangular channel geometries, the Reynolds number (Re) is substituted with the laminar-equivalent Reynolds number Jones [236] defined as:

59

$$Re^* = \frac{\rho u_m D_{le}}{\mu} = \frac{\rho u_m}{\mu}\left[\left(\frac{2}{3}\right)+\left(\frac{11}{24}\right)\left(\frac{1}{\alpha_c}\right)\left(2-\frac{1}{\alpha_c}\right)\right]D_h \qquad (3.22)$$

where $D_{le}$ is the laminar-equivalent diameter given by the term in the brackets in Eq. (3.22)

## 3.3     Total pressure drop in a microchannel heat exchanger

### 3.3.1 Entrance and exit loss coefficients

Because it is difficult to detect the local pressure along the flow, researchers in microchannels have traditionally measured pressure drops between the intake and exit manifolds. The pressure drop measurement that follows represents the total of the losses from the turns, the entry and exit losses, the developing region's effects, and the frictional losses in the core. The pressure drop that was measured is the sum of these variable (Phillips [235]):

$$\Delta p = \frac{\rho\, u_m^2}{2}\left[\left(\frac{A_c}{A_p}\right)^2 (2K_{90}) + (K_c + K_e) + \frac{4f_{app}L}{D_h}\right] \qquad (3.23)$$

where $K_c$ and $K_e$ stand for the contraction, $A_c$ and $A_p$ for the total channel area and plenum cross-sectional area, respectively, and $K_{90}$ for the loss coefficient at 90-degree bends. growth loss coefficients because of changes in area, and $f_{app}$ incorporates both frictional losses and extra losses in the growing flow area.

### 3.3.2 Laminar-to-turbulent transition

Another area that has attracted the attention of many researchers is the change from laminar to turbulent flow. The change from laminar to turbulent flow in abrupt entry rectangular ducts was discovered to happen at a Reynolds number of $Re_t=2200$ for $\alpha_c=1$ and at $Re_t=2500$ for parallel plates with $\alpha_c=0$, according to Hartnett et al. [237]. It is advise using a linear interpolation between the two numbers for various aspect ratios.

An early shift to turbulent flow in microchannels was suggested by a few of the early investigations. The transition from laminar to turbulent flow, however, has not changed, according to a number of recent studies. The transition for circular microtubes with a diameter of 171 to 520 μm happened at $Re_t=2000$, from Bucci et al. [238]. The laminar-to-turbulent transition in smooth microchannels happens at around 2300 and is independent of the channel diameters, according to Baviere et al.

60

[238]. Researchers [239], have found similar outcomes for mini-channels with Dh = 1 mm.

## 3.4    Heat transfer in microchannels

### 3.4.1 Fully developed laminar flow

According to classical theory, the Nusselt number should remain constant in a fully developed laminar flow. However, numerous investigations that have been published in the literature show a trend in which the Reynolds number rises within this range. The channel geometry and the boundary condition for wall heat transfer determine the Nusselt number, which is constant in fully developed laminar flow.

Under four-sided heating, with an axially constant heat flux and a circumferentially constant wall temperature (H1) boundary.

The Nusselt number for a rectangular channel is determined by the channel aspect ratio $\alpha_c$=a/b and the wall boundary conditions. Three boundary conditions are identified in the literature; the Nusselt values for each are displayed below.

$$Nu_T = 7.54(1 - 2.610\alpha_c + 4.970\alpha_c^2 - 5.119\alpha_c^3 + 2.702\alpha_c^4 - 0.548\alpha_c^5) \tag{3.24}$$

With a constant circumferential wall temperature and a uniform axial heat flow, the following conditions hold at the T-boundary:

$$Nu_{H1} = 8.235(1 - 2.0421\alpha_c + 3.0853\alpha_c^2 - 2.4765\alpha_c^3 + 1.0578\alpha_c^4 - 0.1861\alpha_c^5) \tag{3.25}$$

The axial and circumferential heat flow of a constant wall:

$$Nu_{H2} = 8.235(1 - 0.6044\alpha_c + 1.1755\alpha_c^2 - 1.803\alpha_c^3 + 0.9203\alpha_c^4 - 0.29236\alpha_c^5) \tag{3.26}$$

### 3.4.2 Thermally developing flow

In thermally developing flow through ducts, the thermal entry length is generally expressed in the form

$$\frac{L_t}{D_h} = c \, \mathrm{Re} \, \mathrm{Pr}, \tag{3.27}$$

For circular channels, the leading constant c in Eq. (3.27) is determined to be 0.05, however for rectangular channels, the graphs provided by Phillips [235] indicate c to

61

be 0.1. The local heat transport in the developing section of a circular tube is described by the following equations (Shah and London [234]):

$$\text{Nu}_x = 4.363 + 8.68(10^3 x^*)^{-0.506} e^{-41x^*}, where x^* = \frac{x/D_h}{\text{Re} \cdot \text{Pr}} \qquad (3.28)$$

Three-sided heating, αc≥0.1 and αc≤10, use a four-sided heating table without any modification.

Three-side heating, 0.1≤αc≤10:

$$\text{Nu}_{x,3}(x^*, \alpha_c) = \text{Nu}_{x,4}(x^*, \alpha_c) \cdot \frac{\text{Nu}_{fd,3}(x^* = x^*_{fd}, \alpha_c)}{\text{Nu}_{fd,4}(x^* = x^*_{fd}, \alpha_c)} \qquad (3.29)$$

### 3.4.3 Heat Transfer in the transition and turbulent flow regions

The crucial Reynolds number for the laminar-to-turbulent transition was previously covered in depth. The well-established criteria of Re$_c$52300 is anticipated to be valid for smooth channels. A lot of minichannel and microchannel heat exchangers deal with the transition zone; thus, it's important to have good experimental data for smooth and rough tubes in this area.

The following equations are used in the emerging turbulent zone. As x grows bigger, the effect of the expression $[1 + (^{D_h}/_x)^{2/3}]$ gradually decreases to 1:

$$Nu = 0.0214 \left[ 1.01 \left( \frac{D_h}{x} \right)^{2/3} \right] [(Re^{0.8} \cdot 100) Pr^{0.4}] \qquad (3.30)$$

Microchannels are able to have very high heat transfer coefficients because of their small hydraulic widths. Because of the large pressure gradients, researchers have had to employ modest flow rates. However, as the flow rate declines, the fluid stream's ability to disperse heat for a given temperature increase diminishes. The overall cooling performance can be improved by selecting one of these two options.

i.    Cut down on the channel flow length.

ii.   Raise the rate at which the liquid is pumped.

Similar to a split-flow system that offers two streams, it is generally recommended to use multiple streams with short pathways. The designer can employ higher flow rates while maintaining a certain pressure drop limit by reducing the flow length. This method offers several advantages over a single-pass design, where the fluid moves the entire length of the heat exchanger:

i. Because the flow length is shorter, the pressure drop is reduced. Less overall pressure drop results from a shorter flow length.

ii. A larger developing zone results from higher heat transmission during developing conditions, which causes the channel size to increase due to the numerous inlets.

iii. Faster flow rates: Some of the pressure drop reduction may be used to accelerate specific streams. Turbulence flow would be interesting looking into because the heat transfer coefficient is higher here.

## 3.5 Conventional MCHS

### 3.5.1 Problem statement

The geometry of a typical channel for modelling MCHS is shown in Figure 3.2. The values of the parameters $H_C, W_C, H_T, W_T$ and $L_C$, which stand for height, distance between MCHS wall, height, width, and length (in mm), respectively, are 0.2, 0.1, 0.35, 0.25, and 10. The bottom of the MCHS, where heat is absorbed and transported to the coolant fluid, is where electronic appliances generate their heat.

Figure 3.3 shows the four designs that were looked at in this study: MCHS with square ribs (MC-SQ), MCHS with square ribs and filleted corner (MC-SQ-FR), MCHS with square ribs and doble filleted corner (MC-SQ-DFR), and conventional MCHS (S-MCHS). Therefore, in these designs, the influence of rib fillet on thermohydraulic performance in MCHS was be studied. To investigate the fillet radius influence on MC-SQ performance, a fillet radius of 0.01 mm was chosen.
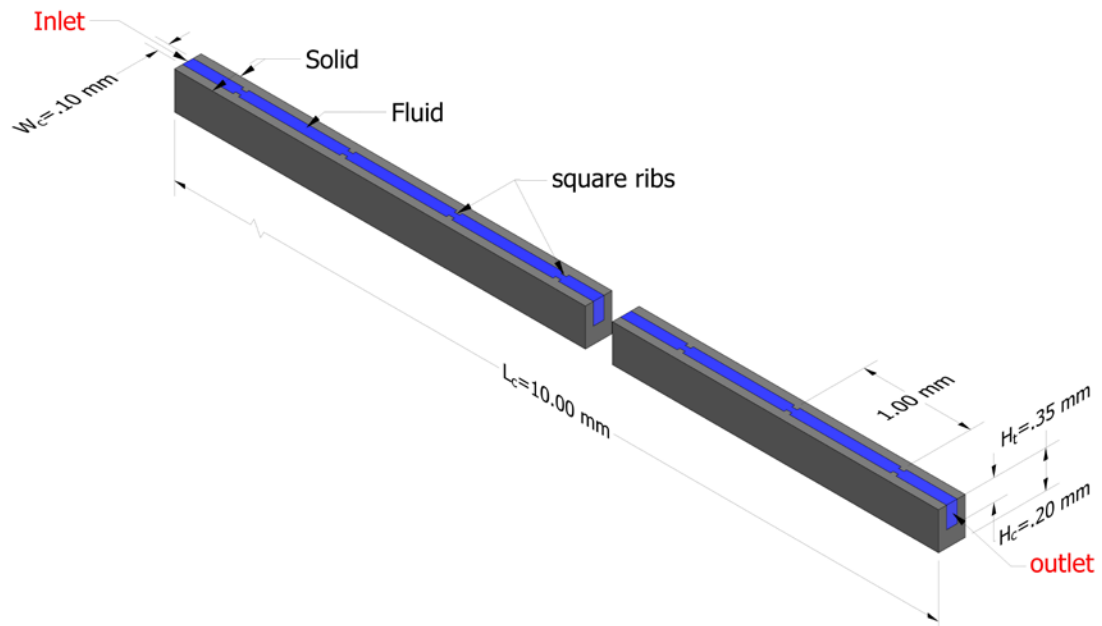
Figure 3.2 Model of the 3-D MCHS with square ribs, including its geometry and schematic perspective.
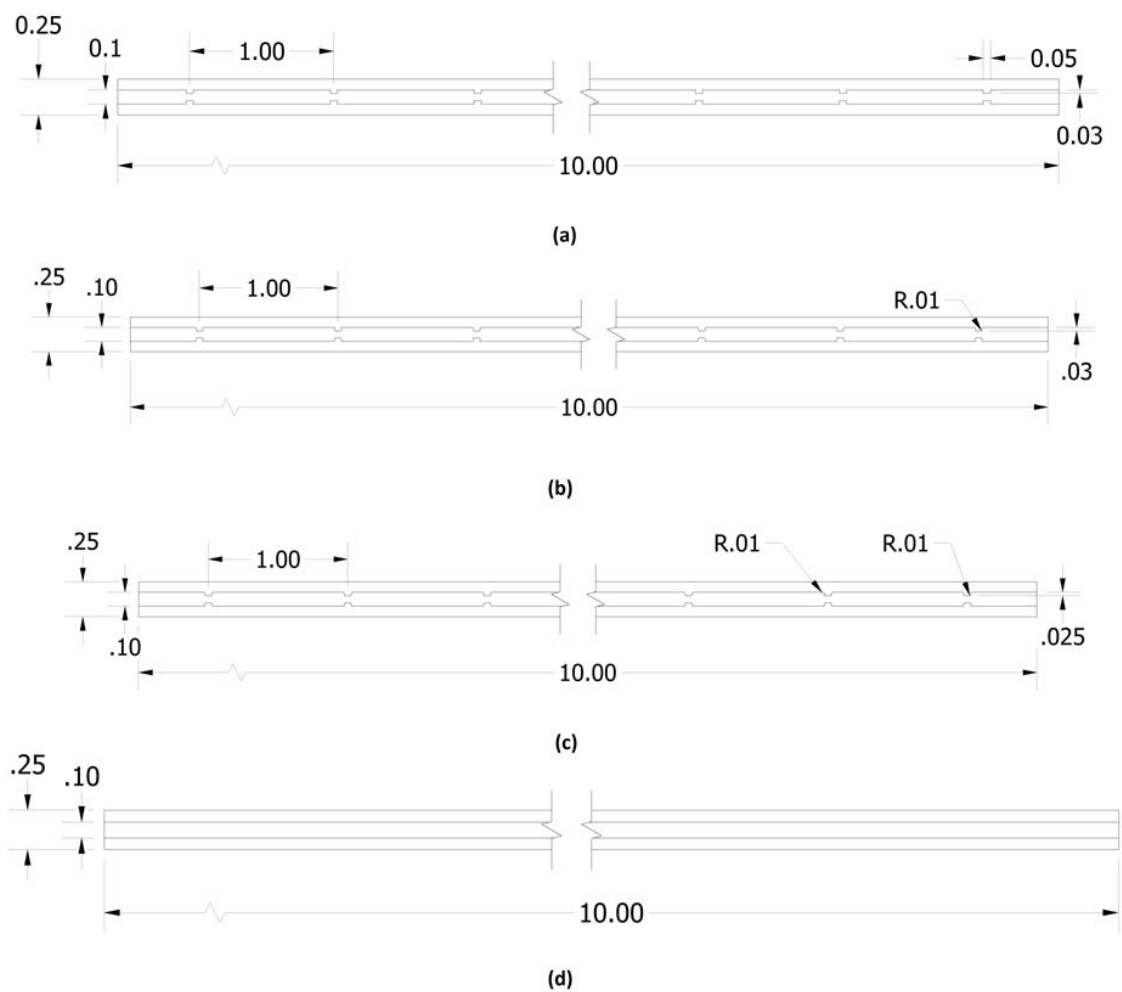


Figure 3.3 Geometrical configuration and dimension of different microstructures: a) MC-SQ, b) MC-SQ-FR, c) MC-SQ-DFR, d) S-MCHS.

64

To assess potential enhancements in thermal hydraulic performance, the S-MCHS is also modelled. Velocity at the inlet is varied from 0.5-3 m/s and corresponding Reynolds number (Re) are 66<Re<398. All Reynolds values have the same heat flux at the heat sink's bottom, which is 100 W/cm$^2$.

### 3.5.2 Numerical methods

The assumptions laid out have been formulated to facilitate a numerical analysis of the thermal and flow behaviour within the MCHS. The continuum assumption was applied due to the very small value of the Knudsen number [240] and hence Navier-Stokes equation can be safely applied in this case. A CFD package Ansys Fluent [241] is used to perform 3-D numerical simulations.

The fluid is considered incompressible, and the flow is characterised as laminar and in a steady state condition. The effects of radiation heat transfer are disregarded. Thermal conductivity of working fluids is expected to be independent of temperature, as is the viscosity. Table 3.1 lists the thermophysical properties of MCHS materials.

Table 3.1 Thermophysical properties of water and Aluminium [242].

| Material | $\rho$(kg.m$^{-3}$) | $C_P$(J.kg$^{-1}$.K$^{-1}$) | $k$ (W.m$^{-1}$.K$^{-1}$) | $\mu$ (kg.m$^{-1}$s$^{-1}$) |
|---|---|---|---|---|
| Water | 998.2 | 4181 | 0.6 | 0.001003 |
| Aluminium | 2719 | 871 | 202.4 | |

### (a) Grid study

The optimal mesh size plays a crucial role in ensuring the accuracy and reliability of numerical simulations. Figure 3.4, depicts a portion of the structured mesh for several MCHS designs. This test is conducted to verify the accuracy of the numerical results. Information regarding the grid study for the MC-SQ with a 2 m/s input velocity is provided in Table 3.2. Result is compared after the calculation of relative error (e%) is

$$e\% = \left| \frac{G_{max} - G_{min}}{G_{max}} \right| \times 100 \qquad (3.31)$$

Where G denote any parameter such as, temperature, Nu etc. The grid of $1 \times 10^6$ is selected as the ideal configuration for the investigation based on the findings.
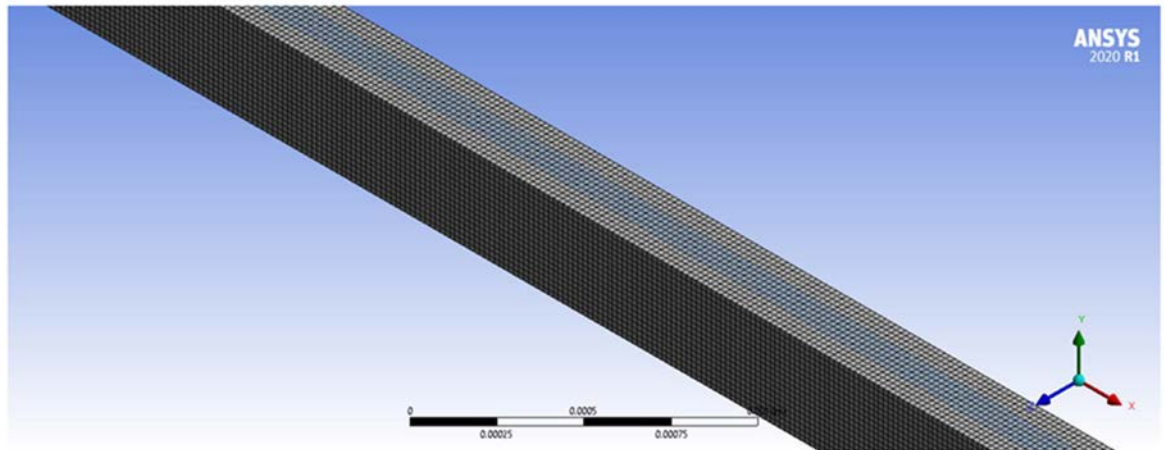
Figure 3.4 3D diagram depiction of the MC-SQ structured mesh design

Table 3.2 Grid independency test

| Grid number ($\times 10^6$) | $\Delta P$ ($kPa$) | e % |
|---|---|---|
| 0.75 | 105.05 | 5.31 |
| 0.80 | 107.98 | 2.5 |
| 1.2 | 109.38 | 0.8 |
| 1.5 | 110.57 | - |

**(b)  Solution procedure**

ANSYS Fluent is used to solve the governing differential. The SIMPLEC algorithm is employed for pressure-velocity coupling in microchannels.    The residuals for all governing equations are maintained within the range of $10^{-9}$ to ensure convergence in numerical simulations.

**(c) Different parameters**

The primary parameters that characterise the thermohydraulic performance of MCHS are determined through the analysis of numerical simulation results. The hydraulic diameter is:

$$D_h = \frac{2W_c H_c}{W_c + H_c} \tag{3.32}$$

Where $W_c$ is width and $H_c$ is height of MCHS, respectively. Reynold number is given by:

66

$$Re = \frac{\rho_f u_{in} D_h}{\mu_f} \tag{3.33}$$

In this equation, $\rho_f$ represents density, $\mu_f$ viscosity, and $u_{in}$ represents inlet velocity of fluid, respectively.

Where, $L_T$, $u_m$, and $\Delta P$ indicate length of the MCHS, velocity of the fluid, and pressure drop, respectively. calculation of average Nusselt number is done by:

$$Nu_{ave} = \frac{h_{ave} D_h}{k_f} \tag{3.34}$$

Where $k_f$ is fluid thermal conductivity and $h_{ave}$ is avg. convective heat transfer coefficient, which is specified as:

$$h_{ave} = \frac{q A_{film}}{A_{con}(T_{ave,w} - T_{ave,f})} \tag{3.35}$$

Parameters such as $q$, $A_{film}$, and $A_{con}$, correspond to heat flux, surface area subjected to heat flux, heat transfer area, and $T_{ave,w}$ and $T_{ave,f}$ represents wall average temperature and mean fluid temperature of MCHS respectively.

## 3.6    Fractal model design

The key parameters of fractal-like structures encompass the branching angle, branch count, channel diameter, and channel length. Pence [243] created a fractal-like channel in a disklike heat sink, starting with Murray's investigation of blood arteries.

The subsequent scale factors describe the topological structure of a tree-like network (West et al. [119]; Xu et al. [244]). To reduce the required pumping power, almost all prior research endeavours have established $\beta$ and $\alpha$ to be $n^{-1/3}$ and $n^{-1/2}$, respectively [119,243].

$$\alpha_k = \frac{L_{k+1}}{L_k} = n^{-1/2} \tag{3.36}$$

$$\beta_k = \frac{D_{k+1}}{D_k} = n^{-1/3} \tag{3.37}$$

where $\alpha$ and $\beta$ are the successive lengths ($L$) ratio. As shown in Figure 3.5, the subscript $k$ ($= 0,1,2 \ldots$) denotes the branching level, which is indexed from 0 to 3, $k$ represents branching level order with 0 representing lower and $k + 1$ higher order, at a bifurcation point, $L_0$ and $D_0$ are the length and diameter of the parent channel. In

67

this research, '$D$' denotes the hydraulic diameter, while '$n$' signifies the number of branches into which each channel divides. In this study, '$n$' is assumed to be 2.

In the context of a bifurcating channel structure with n = 2, based on Equations (1) and (2), the diameter ratio (β) is calculated as 0.7937 and the length ratio (α) as 0.7071, respectively. The expression of the hydraulic diameter is given by:

$$d_k = \frac{4A_k}{P_k} = \frac{2Hw_k}{H + w_k} \tag{3.38}$$

In this study, the fractal channel maintains a consistent channel depth denoted as $H$. The variables $A_k$, $P_k$ and $w_k$ represent the wet area, wetted perimeter, and width of the kth-level segment. $w_k$ may be written as follows:

$$w_k = \frac{w_{k+1}H}{\beta(w_{k+1} + H) - w_{k+1}} \tag{3.39}$$
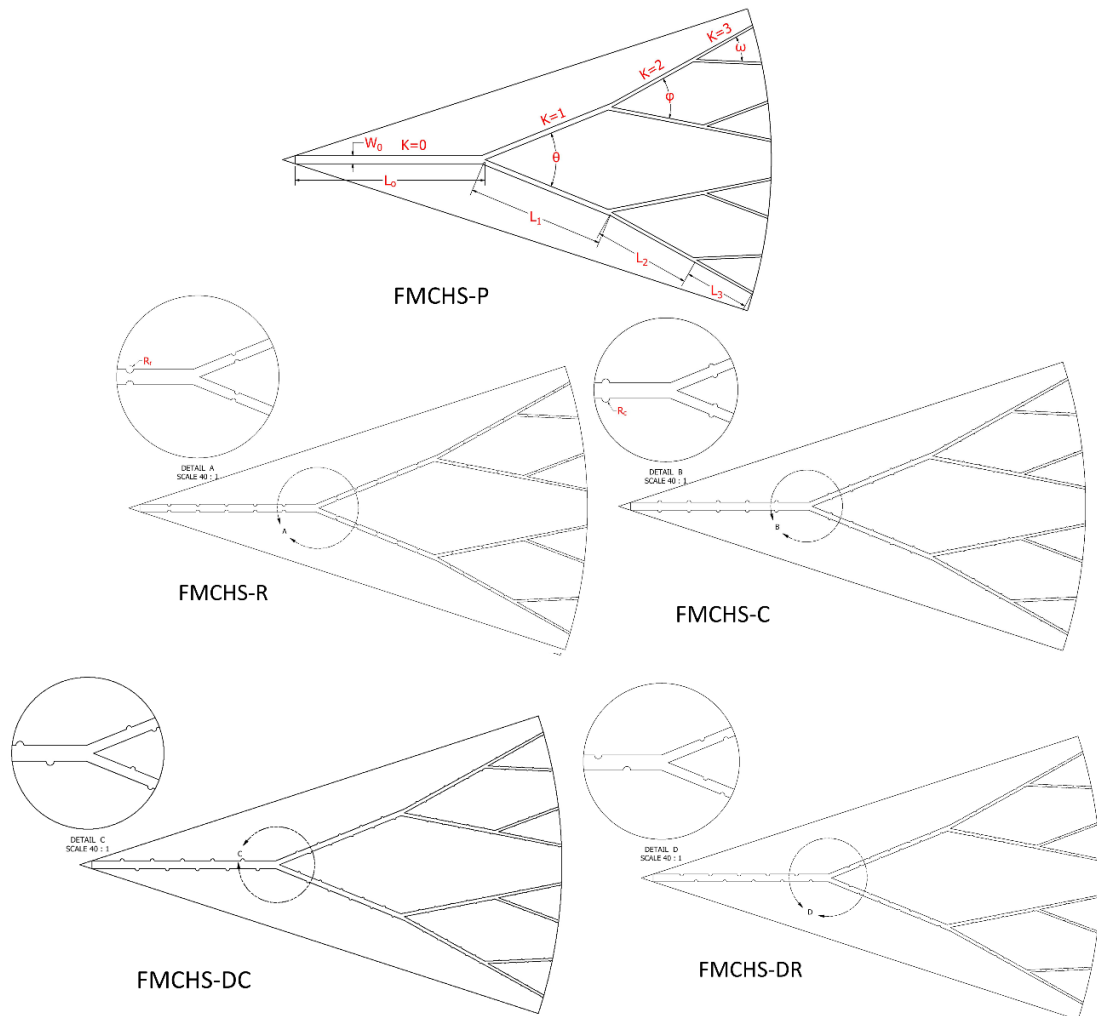


Figure 3.5 Model Schematic depicting all types of models.

68

Using the aforementioned conditions, channel dimensions have been calculated for the fractal microchannel, the same as the fractal dimensions used in Xu et al. [197] and are presented in Table 3.3. Channel Height ($H_k$) at each branching level is equal and is 0.250 mm. Branching angles $\theta$, $\varphi$, and $\omega$ are 44$^\circ$, 40$^\circ$, and 32$^\circ$. The diameter of MCHS in this study is 40 mm. Locations of Ribs and cavities made inside the channel follow the scaling laws. A number of ribs and cavities placed inside each channel of the simple FMCHS is 10, and this is placed at regular intervals. The diameter of circular ribs and cavities in each channel is considered as half of the width of that channel.

Table 3.3: Channel Dimension of the FMCHS (mm).

| Width | | Hydraulic Diameter | | Length | |
|---|---|---|---|---|---|
| $w_0$ | 0.333 | $D_0$ | 0.286 | $L_0$ | 8.01 |
| $w_1$ | 0.208 | $D_1$ | 0.227 | $L_1$ | 5.66 |
| $w_2$ | 0.141 | $D_2$ | 0.180 | $L_2$ | 4.00 |
| $w_3$ | 0.100 | $D_3$ | 0.143 | $L_3$ | 2.83 |

### 3.6.1 Numerical model

Using Autodesk Inventor, a three-dimensional model has been produced, which is depicted in Figure 3.5. As shown in Figure 3.5, the FMCHS having varied cross-sections is created by inserting semicircular cavities or ribs into each microchannel of the smooth FMCHS at regular intervals. The sizes of the ribs and cavities are designed to be equal to 50% of the associated microchannel's width. The scaling law is followed by the first cavity, the locations of the ribs, and the gaps between levels.

A 3D numerical study is done to better estimate the thermohydraulic performance of the fractal MCHS. The computational region,is cut down to be 1/N1 of the entire heat sink by leveraging geometric symmetry. For instance, if the ideal model contains 10 fractals, then the computational domain is chosen to be 1/10 of the entire MCHS, which consists of one fractal. Due to this structure, fewer nodes are required for analysis, which reduces processing costs.

69

### 3.6.2 Model assumptions and governing equations

Convective heat transfer is characterized using the Navier-Stokes and energy equations to examine the impact of variations in geometrical parameters and different flow rates on FMCHS working. In this context, the following presumptions are made:

   i.   It is assumed that the flow is three-dimensional and in a steady state.

   ii.   The flow is incompressible, laminar, and single phase.

   iii.   All types of body forces are ignored.

   iv.   Viscous dissipation and external heat transfer are neglected

The governing equations based on the aforementioned assumptions, describing fluid flow and energy interactions, are as follows:

Fluid flow:

$$\nabla.\bar{V} = 0 \tag{3.40}$$

$$\rho_f(\bar{V}.\nabla\bar{V}) = -\nabla P + \mu_f\nabla^2\bar{V} \tag{3.41}$$

Energy equation (fluid)

$$\rho_f C_{pf}(\bar{V}.\nabla T) = k_f\nabla^2\bar{V} \tag{3.42}$$

Energy equation (solid)

$$\nabla^2 T_s = 0 \tag{3.45}$$

In this context: $V$ represents the velocity field, $P$ represents the pressure field, $\rho_f$ fluid density, $\mu_f$ dynamic viscosity, $C_{pf}$ fluid specific heat, $T$ stands for the temperature, $k_f$ denotes the fluid thermal conductivity.

The boundary conditions for these equations are presented in Table 3.4

Table 3.4 Boundary conditions in various regions of the FMCHS

| Boundary condition | Zone | expression |
|---|---|---|
| Pressure outlet | FMCHS outlet | $z = L, P_f = P_{out} = 0$ |
| Velocity inlet | FMCHS inlet | $z = 0 : u = u_{in} \quad T_f = T_{in} \quad , \quad T_{in} = 293\ K$ |
| heat flux | At bottom plane (constant.) | $y = 0: -k_s\dfrac{\partial T_s}{\partial n} = q = 50\ W/cm^2$ |
| Symmetry | Sidewalls | $\dfrac{\partial T_s}{\partial n} = 0$ |
| No slip and Stationary | Interface | $u = v = w = 0$ |
| Adiabatic | Front and top wall | $\dfrac{\partial T_s}{\partial z} = 0$ or $\dfrac{\partial T_f}{\partial z} = 0$ |

70

Where $u_{in}$ represents the fluid velocity, $T_{in}$ represents the inlet temperature, $P_{out}$ is the outlet pressure, $q_w$ denotes the heat flux at the bottom wall of the MCHS, and $n$ denotes local coordinates perpendicular to the wall. The volumetric flow rate $(q)$ in the FMCH is equal to the product of the FMCHS's inlet area $(A_c)$ and the velocity at the inlet, which is the basis for calculating the inlet velocity $(u_{in} = q/A_c)$. Consequently, it is possible to compute the FMCHS inlet's velocity corresponding to each volumetric flow rate.

### 3.6.3 Comprehensive performance assessment

Nusselt number (Nu), pressure drop($\Delta$P), thermal resistance $(R_{th})$, Performance evaluation criteria (PEC) are employed to assess the performance of FMCHS. Nusselt number is calculated by

$$Nu = \frac{h\overline{D}_h}{K_f} \tag{3.46}$$

Where, h and $\overline{D}_h$ denote the average heat transfer coefficient and hydraulic diameter of FMCHS.

Heat transfer coefficient is evaluated by

$$h = \frac{Q_f}{A_c(T_w - T_f)} \tag{3.47}$$

Where, $T_w$ and $T_f$ are the avg. temperature of the microchannel wall and cooling fluid. $A_c$ represents heat transfer area, and $Q_f$ indicates heat absorbed by the fluid, which can be determined as follows:

$$Q_f = \dot{m}C_{Pf}(T_{out} - T_{in}) \tag{3.48}$$

Where $\dot{m}$ indicates the mass flow rate, $T_{out}$ is the temperature at the channel outlet. whereas $T_{in}$ is the inlet temperature of the working fluid.

The pressure drop is given by:

$$\Delta P = P_{in} - P_{out} \tag{3.49}$$

Where, $P_{in}$ and $P_{out}$ is the inlet and outlet pressure of FMCHS, respectively.

Thermal resistance R$_{th}$ of the FMCHS is defined as:

$$R_{th} = \frac{T_{w,max} - T_{in}}{Q_f} \tag{3.50}$$

Where, $T_{w,max}$ is the maximum wall temperature.

Pumping power is determined by,

71

$$\Omega = q.\Delta P \qquad (3.51)$$

Where, q is the volumetric flow rate (ml/min) in the FMCHS, and $\Delta P$ is in pressure drop across the FMCHS.

Performance evaluation criteria are termed to find the effective operation of FMCHS, i.e., to evaluate the relationship between friction factor and Nusselt number, it is described as

$$PEC = (Nu/Nusm)/(\Delta P/\Delta Psm)^{\wedge}(1/3) \qquad (3.52)$$

Nu is the Nusselt number of the modified FMCHS, and $Nu_{sm}$ is the Nusselt number of simple FMCHS. Similarly, $\Delta P$ and $\Delta Psm$ is the pressure drop of simple and modified FMCHS.

To compute performance indicators such as the Nu, $\Delta P$, $R_{th}$, and, $\Omega$ it is necessary to have information on the average temperatures of the microchannel wall temperature ($T_w$) besides the inlet and outlet pressures ($P_{in}$ and $P_{out}$) within the fractal microchannel. The governing equations are solved employing the finite volume method (FVM) by employing Ansys Fluent solver. This entails the following steps: converting and incorporating PDEs into equations of balance over an element and creating algebraic equations from the algebraic relations. A SIMPLE algorithm is used for pressure-velocity coupling. The pressure correlation, momentum, and energy equations have relaxation factors of 0.3, 0.7, and 0.6, respectively. Simulations were conducted throughout the iterative solution process until the residuals dropped below $10^{-7}$ for all flow variables and $10^{-8}$ for the energy equation. The most common material used in electronic chip devices is silicon, used in the present study. Thermophysical properties of the silicon are specific heat ($c_{p,s}$), density ($\rho_s$), thermal conductivity ($k_s$) and their values are 712 J/kg-K, 2329 kg/m$^3$, and 148 W/m-K, respectively. The working fluid is water, and its thermophysical properties include density ($\rho_l$), dynamic viscosity ($\mu_f$), specific heat ($c_{p,f}$), and thermal conductivity ($k_f$) and their values are 1000 kg/m$^3$, 8.55×10$^{-4}$ kg/m-s, 4179 J/kg-K and 0.613W/m-K.

### 3.6.4 Grid sensitivity test

A numerical grid is generated for solid and fluid regions spanning the computational domain. The structured and unstructured grids are designed using finite-sized hexahedral and tetrahedral mesh. A detailed view of the mesh of the fluid computational domain is illustrated in Figure 3.6.

To mitigate interpolation-related numerical inaccuracies arising from the intricate geometry of the FMCHS, supplementary boundary layers are incorporated at the solid-liquid conjugate boundary, effectively reducing the grid size in that area. To evaluate the sensitivity of the numerical findings on the obtained findings, four different-sized grids, 959676 (coarse), 1669648 (medium), 2491204 (fine), and 3541739 (very fine) elements-are taken into consideration. The grid independence test uses the $Nu_{avg}$, which is calculated as shown in Figure 3.7. The $Nu_{avg}$ results in Figure 3.7 demonstrate that the trend does not alter considerably even after a grid is progressively refined.

$$E\% = \frac{f_2 - f_1}{f_1} \tag{3.54}$$
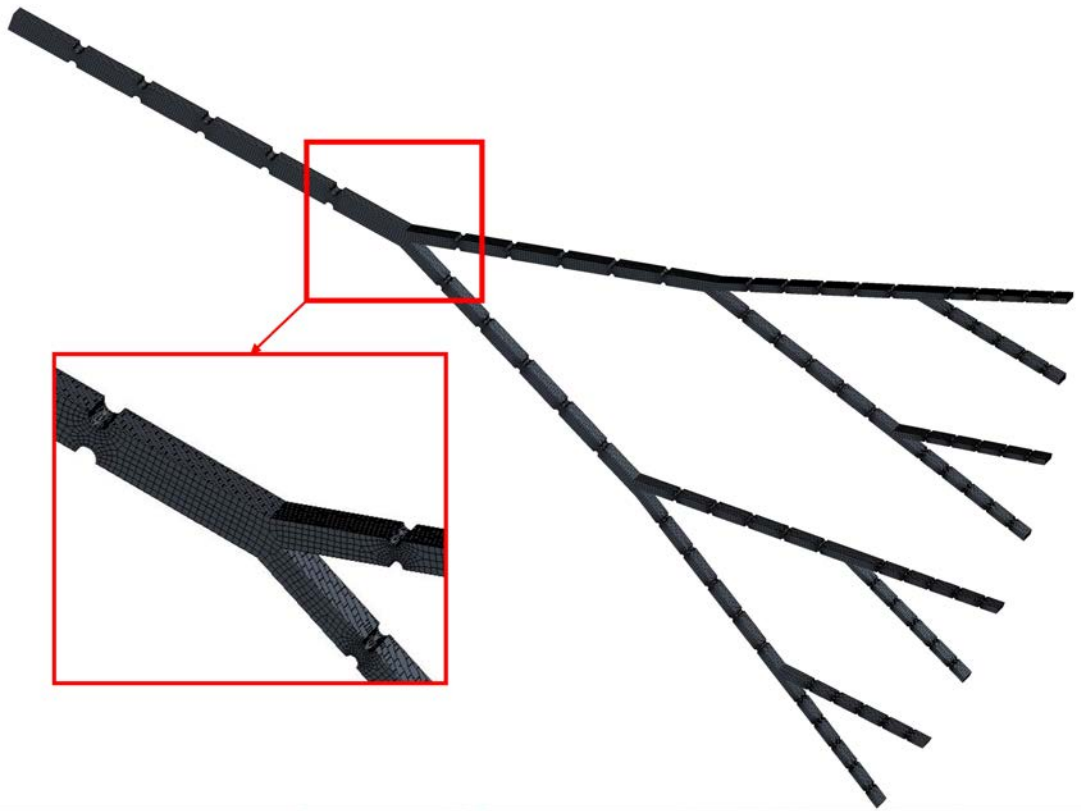


Figure 3.6 Mesh of the computational Domain.
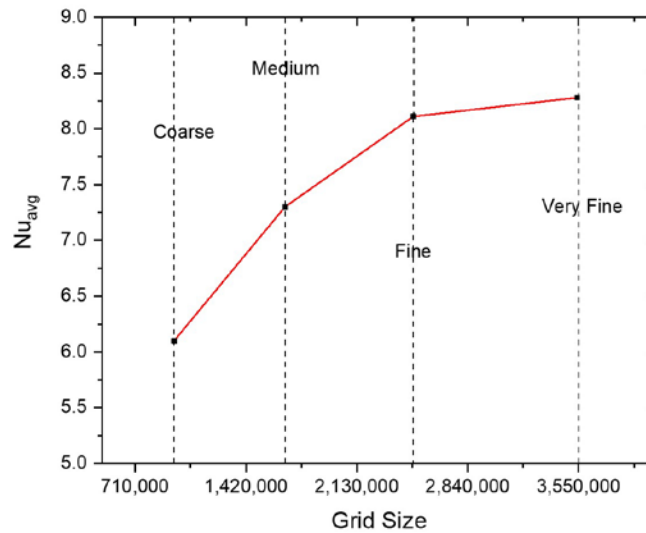
Figure 3.7: Grid sensitivity Test showing Average Nusselt number vs Grid Size.

Equation (3.54) is employed to calculate the percentage variations between fine ($f_2$) and very fine ($f_1$) grids, revealing changes within the range of approximately 2%. The percentage change in the Nu$_{avg}$ at various grid sizes is referred to as the relative percentage error, or E%. The findings of the grid independence testify to the fine-type grid's suitability and accuracy.

## 3.7    Heat transfer enhancement with nanofluids

The governing equations' assumptions are 3D fluid flow, laminar and incompressible, steady and irrotational, and thermo-physical properties that are temperature-dependent for nanofluid.

The finite volume mathematical framework was solved using ANSYS Fluent 2022 R1. The pressure-velocity coupling technique COUPLED, pressure interpolation equations PRESTO (Pressure Staggering Option), and momentum interpolation equations QUICK were used. The convergence criteria were $10^{-6}$ mass, $10^{-8}$ momentum, and $10^{-10}$ species concentration.

The thermos-physical properties of nanofluids have been determined using the following equations [245,246]:

$$\rho_{nf} = (1 - \emptyset)\rho_f + \emptyset\rho_{np} \tag{3.54}$$

$$(\rho C_p)_{nf} = (1 - \emptyset)(\rho C_p)_f + \emptyset(\rho C_p)_{np} \tag{3.55}$$

$$\mu_{nf} = \mu_f(1 + 2.5\emptyset) \tag{3.56}$$

74

Here, the indices $f$, $np$, and $nf$ represent the base fluid, nanoparticle, and nanofluid, respectively. Additionally, the thermal conductivity is determined using the following equation.

$$k_{nf} = k_{static} + k_{brownian} \tag{3.57}$$

$$k_{static} = k_f \left[ \frac{(k_{np} + 2k_f) - 1\emptyset(k_f - k_{np})}{(k_{np} + 2k_f) + \emptyset(k_f - k_{np})} \right] \tag{3.58}$$

$$k_{brownian} = 5 * 10^4 \, \beta\emptyset\rho_f C_{p,f} \sqrt{\frac{kT}{\rho_{np} D_{np}}} \, g(\emptyset, T) \tag{3.59}$$

Here, $k = 1.38 * 10^{-23} \, J/K$ and $\beta$ is a liquid fraction with the particle g(T, $\emptyset$) is model function as below;

$$g = (-6.04\emptyset + 0.4705)T + 1.722.3\emptyset - 134.63 \tag{3.60}$$

The ferrous oxide nanoparticles, with a diameter of 15 nm, are assumed to have a density of ρ = 4950 kg/m³. Additionally, their thermal conductivity and specific heat are considered k = 7 W/m·K and Cp = 640 J/kg·K, respectively.

Governing equations

   i.   Navier-Stokes Equation (Incompressible Flow)

$$\rho_{nf} \left( \frac{\delta u}{\delta t} + u.\nabla u \right) = -\nabla P + \mu_{nf} \nabla^2 u \tag{3.61}$$

   ii.   Energy Equation

$$\rho_{nf} C_{p,nf} \left( \frac{\delta T}{\delta t} + u.\nabla T \right) = k_{nf} \nabla^2 T \tag{3.62}$$

   iii.   Transport Model

$$\frac{\partial \varphi}{\delta t} + u.\nabla\varphi = \nabla.(D_B \nabla\varphi + D_T \nabla T) \tag{3.63}$$

## 3.8   Design optimization of MCHS

The geometry of microchannel heat sinks plays a critical role in determining thermal performance. Optimizing the channel configuration is essential to enhance heat transfer while minimizing flow resistance. However, improving heat transfer often results in increased pressure drop, making it vital to explore designs that balance thermal enhancement and hydraulic performance. Numerical optimization methods, integrated with CFD simulations, have proven effective for the design and analysis of MCHS. These approaches include both single- and multi-objective optimization techniques for geometric refinement.

75

### 3.8.1 Surrogate Model vs Convention- Based Optimization

Researchers have utilized various techniques to optimize systems with specific inputs and responses. One of the easiest methods is a parametric study, which systematically analyses the effect of particular design parameters on the system's behaviour while keeping all other factors constant. However, a more advanced and comprehensive approach involves applying design of experiments (DOE) methodologies. DOE techniques allow for the simultaneous variation of multiple parameters to assess their collective impact on system performance, leading to more efficient optimization. Standard DOE methods include factorial designs, which systematically evaluate interactions between parameters, and Latin hypercube sampling, which ensures a well-distributed exploration of the input space for improved statistical accuracy. These approaches enable researchers to gain deeper insights into system dynamics and optimize performance more effectively.

While these approaches can help identify acceptable or feasible designs, finding the optimal design remains crucial. Using appropriate algorithms, optimization makes it possible to thoroughly investigate the whole design space to maximize or decrease a system's response. This procedure may be carried out using gradient-based methods, which are helpful for restricted and unconstrained optimization, or heuristic approaches, such as particle swarm optimization, which are helpful for complicated, nonlinear, or high-dimensional search spaces. Both of these methods are effective for solving optimization problems effectively. By selecting the appropriate optimization technique, engineers and researchers can enhance system performance, improve efficiency, and achieve desired outcomes more effectively.

Two optimization strategies: conventional and surrogate-based optimization. When evaluating the objective function(s) for fluid and thermal system optimizations, one of the most important steps is analyzing the underlying physical processes by employing the Navier–Stokes equations and the transport equations for heat and mass transfer while applying the proper boundary conditions. The traditional and advanced optimization methodologies use this analysis as a vital component. The manner in which the numerical model interacts with the optimization algorithm is the fundamental factor that differentiates these two methodological approaches. Because the numerical model is directly integrated with the algorithm in traditional optimization, it is necessary to do multiple simulations for each design iteration. This

76

may be a time-consuming and computationally costly process. A significant disadvantage of this approach is the high computational cost associated with running the model repeatedly throughout the optimization process.

The use of surrogate modelling helps to alleviate this problem by lowering the amount of computer resources required and by providing a trustworthy approximation of the simulation data. A final surrogate model is generated by employing a suitable process that comprises training, testing, and validation, primarily when neural networks are utilized. This method is based on the results of the CFD simulation. Once validated, the surrogate model is used as a fitness function in the optimization algorithm, enabling faster and more efficient identification of the optimal design. To ensure the best results, the effectiveness of the surrogate model is evaluated in terms of its ability to explore the design space globally and exploit it locally before being coupled with the optimizer. Surrogate-based optimization has become widely used in the design optimization of MCHS.

### 3.8.2  Design of Experiment (DOE)

Investigation of the design variable space is accomplished through the use of Design of Experiments (DOE) methodologies. It is done to optimize the quantity of information obtained by determining the relationship between the multiple components that impact a process and the outcome of that process. In the optimisation process, the DOE techniques are utilized to generate design points, which are subsequently used in creating a surrogate model. When it comes to fitting different models, having a sample blueprint that is adequately built is quite necessary. Latin hypercube sampling, often known as LHS, is a type of stratified sampling that can be applied to a wide range of variables. It is one of the DOE methods that is utilized the most commonly.

### (a)  Latin Hypercube Sampling (LHS)

LHS is a stratified variant of Monte Carlo sampling. The sampling zone is systematically partitioned by segmenting the range of each x component. We will exclusively examine the scenario in which the parts of x are independent or may be converted into an independent basis. Furthermore, generating samples for coupled components with a Gaussian distribution is readily attainable. As previously outlined, LHS functions to produce a sample size N from the variables $x1, x2, x3, ..., xn$. The range of each variable is divided into N non-overlapping intervals with equal

77

probability size $1/N$. A value is randomly picked from each interval according to the probability density inside that interval. The N values acquired for $x1$ are randomly matched with the N values of $x2$. N pairings are randomly paired with the N values of $x3$ to create N-triplets, and this process continues until a collection of N-tuples is established. This collection of N-tuples constitutes the Latin hypercube sample. Therefore, for specified values of N and n, there are $(N!)$ $n-1$ potential interval combinations for an LHS. A 10-run Latin Hypercube Sampling (LHS) for three normalized variables (range [0, 1]) utilizing a uniform probability density function is presented below. The values separated at equal probabilities are 0, ..., 0.8, 1.

## (b) Surrogate Modelling

In optimising thermo-fluid, numerous numerical analyses are needed to assess objective function(s). Still, each simulation can be time-consuming due to the complexity of the non-linear governing differential equations. To reduce this burden, surrogate modelling is used to create approximation models that closely replicate the behaviour of the simulation model. Surrogate modelling's key advantages are its computing efficiency in assessing the goal function(s) and its correctness in reflecting the design space features. Both of these advantages are associated with surrogate modelling. In the following discussion, the mathematical formulas for a variety of surrogate models are presented.

## (c) Response Surface Approximation (RSM)

A mathematical model, often a polynomial equation, is used in RSM. This model is used to characterize the connection between the input variables and the response variable(s) that are of interest (Eq. 3.64). The model is fitted to experimental data from a series of designed experiments. A factorial design is often utilized in the execution of these studies. In this design, many combinations of input variables are evaluated to assess the influence that these combinations have on the response variable.

$$Y = b_o + \sum_{i=1}^{3} b_i x_i + \sum_{i=1}^{3} b_i x_i^2 + \sum_{i=1j=1}^{3} b_i x_i x_j \tag{3.64}$$

$$d_n = \begin{bmatrix} 0 & n < L_n \\ \dfrac{n - L_n}{G_n - L_n} & L_n < n < G_n \\ 1 & n > G_n \end{bmatrix} \tag{3.65}$$

78

$$d_n = \begin{bmatrix} 0 & n > H_n \\ \dfrac{n - H_n}{G_n - H_n} & G_n < n < H_n \\ 1 & n < G_n \end{bmatrix} \qquad (3.66)$$

$$\text{Desirability} = [\pi(d_n w_n)]^{\frac{1}{w}} \qquad (3.67)$$

Here, n, $G_n$, $L_n$, $H_n$, and $r_n$ the forecast value, the target value, the lower suitable value, the higher suitable value, and the desirability function weight when it comes to the nth output, respectively. The variable $w_n$ is used to denote the significance of the nth output, and the value of W is equal to the sum of $w_n$. The value of the desirability factor can range from 0 to 1, with 1 indicating the ideal choice that is desired the most and 0 indicating the one that is desired the least.

RSM aims to determine the optimal input variables for maximising or minimising the output variable(s) within a specified range. ANOVA was used to assess the relevance of each input variable's role in influencing output responses and the model's dependability. From the 3D response surface plot, the interaction influence of input parameters on output was observed.

Using RSM in conjunction with a desirability function, one may locate the best possible answer for a response with several objectives. According to the framework of the desirability approach, the solution that is considered to be the best alternative is the one that holds the highest combined desire factor. The Eq. (3.65) is used to determine the individual desirability (dn) for an output parameter that is intended to maximize the output, whereas the equation (3.66) is utilized to minimize the output. The combined desirability is determined as described in Eq. (3.67).

The simulation results are statistically analysed using ANOVA, a method based on the principle of general variance, employed to assess differences among all the findings in a sample. Using ANOVA is quite helpful and illuminating when comparing data across many categories. The p-value, F-value, $R^2$, Adj $R^2$, and Pred $R^2$ values in the ANOVA test, which represent the variance of the data from the mean, are indications of the validity and quality of the results.

### 3.8.3 Artificial neural network (ANN)
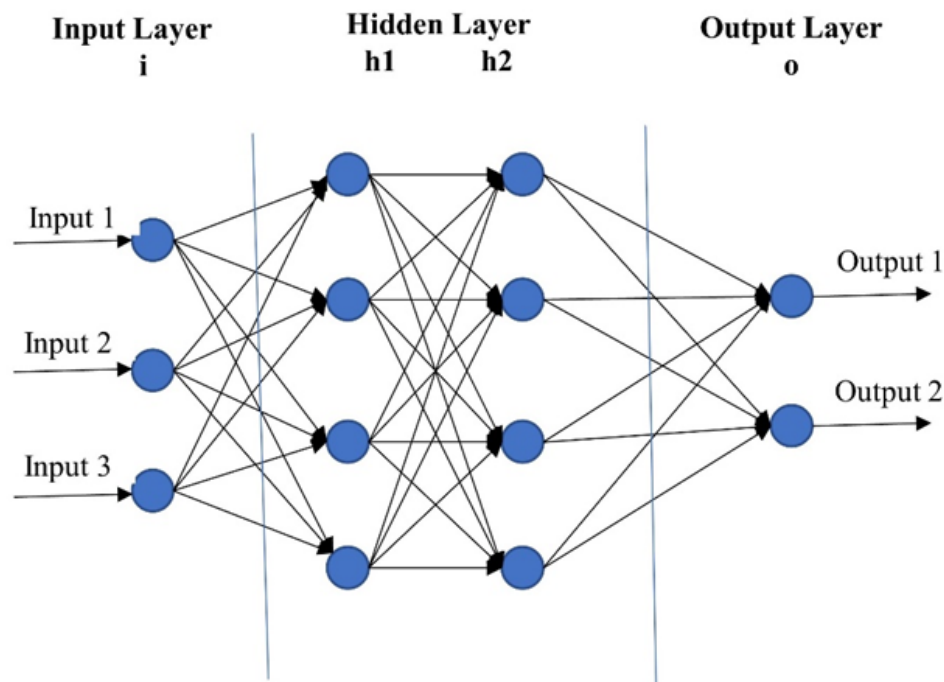


Figure 3.8 ANN Schematic.

An analytical tool called ANN is used to validate the correlation between input and output variables and verify the data's predictive regression. The multilayer perceptron (MLP) neural network architecture and the backpropagation technique are used in this ANN study. MATLAB R2020a is used for coding and execution. MLP planning, as shown in Figure 3.8 is in the format of A-H1-H2-Z, where A and Z indicate the input and output layers, and H1 and H2 are hidden layers. For each output, a network is built to train the DOE findings. Each hidden layer neuron in the network ranges from 1 to 10, and many neuron combinations are used during training. Then, the neuronal pairings with the lowest RMSE are chosen. The best neuron combination discovered is then utilised to build a new network for each output. Mean square error (MSE) was used as the performance function, while Levenberg Marquardt (trainlm) was used as the training function. The hidden layer uses the Tan-sigmoid, and the output layer is handled by Log-sigmoid functions of transfer, respectively. From datasets, train network 70%, test 15%, and the rest to validate was used.

### 3.8.4  Moth Flame Optimization (MFO)

The MFO algorithm was modelled after moths' navigational strategy [247]. Moths have a highly efficient mechanism for flying at night that maintains their orientation relative to the moon and makes them move long distances in a straight line. Solutions

80

proposed for the MFO method are moths and the variables in the space. The moths may change their location vectors and fly in 1-D, 2-D, 3-D, or multidimensional space. The population-based nature of the MFO method requires the pair of moths to be described in a matrix (equation (3.67)) as mentioned below:

$$M = \begin{bmatrix} m_{1,1} & \cdots & m_{1,d} \\ \vdots & \ddots & \vdots \\ m_{n,1} & \cdots & m_{n,d} \end{bmatrix} \qquad (3.68)$$

$$S(M_i, F_j) = D_i . e^{bt} cos(2\pi t) + F_j \qquad (3.69)$$

Here, n is the moth number, d is the variable, S is the spiral function, $M_i$ and $F_j$ are ith moth and jth flame and D is the distance of $i^{th}$ moth and $j^{th}$ flame; equation (3.68) shows the spiral moth path simulations, as depicted in Figure 3.9a. The variable t indicates the adjacent position of the moth to the flame ($t = -1$ is proximate and $t = 1$ is farthest), displayed in Figure 3.9.

By increasing moths, the probability of finding the global minimum is higher. However, it has been shown that 30 is an appropriate number of months for resolving optimisation issues.

### 3.8.5 Harris Hawk Optimization (HHO)

HHO is a metaheuristic optimization algorithm inspired by the hunting behaviour of Harris's hawks, a species of raptors depicted in Figure 3.9. The algorithm mimics these birds' cooperative hunting strategy to search for and capture Prey.

In HHO, the optimization problem is represented as a population of hawks. Every Hawk symbolises a prospective solution to the problem, and its location within the search space corresponds to the values of the decision variables. The Hawks collaborate and share information to improve the overall search process. Given that HHO is a population-based, gradient-free optimization method, any optimization issue may be addressed with it with the correct formulation. All of the HHO stages are depicted in Figure 3.11. They are discussed in the following sections [248].

   i.   Exploration phase

Here, hawks explore and trail prey using their instinct. The Harris hawks in HHO huddle at isolated spots and use one of two methods to watch for Prey to appear.

81

$$X(t+1)$$
$$= \begin{cases} X_{random}(t) - r_1|X_{random}(t) - 2r_2X(t)| & q \leq 0.5 \\ X_{prey}(t) - X_m(t) - r_3\big(Lb + r_4(Ub - Lb)\big) & q < 0.5 \end{cases} \quad (3.70)$$

X(t+1) denote the Hawks position vector for iteration. $X_{prey}$ denotes prey location, X(t) symbolises hawks' current location, and $r_1$, $r_2$, $r_3$, $r_4$, and q are arbitrary numbers between [0,1], which changes with iteration. Ub and Lb symbolise variables of upper and lower bonds. $X_{random}(t)$ is the arbitrarily chosen Hawk's location and $X_m$ is the average current location of the hawks' population.

$$X_m(t) = \frac{1}{N}\sum_{i=1}^{N} X_j(t) \quad (3.71)$$

$X_i(t)$ is every hawk location in iteration, and N is the total hawk.

The HHO technique exploits Prey's behaviour to escape. Hence, the energy of Prey diminishes. The energy of Prey is represented by equation 3.71 to illustrate this step:

$$E = 2E_o(1 - \frac{t}{T}) \quad (3.72)$$

E denotes the energy of Prey fleeing, and $E_o$ is the initial energy state.

ii.    Exploitation phase

When Hawk attacks Prey, they try to escape, and the probability of fleeing is $|r| < 0.5$, getting caught $|r| \geq 0.5$.



(a)                                        (b)
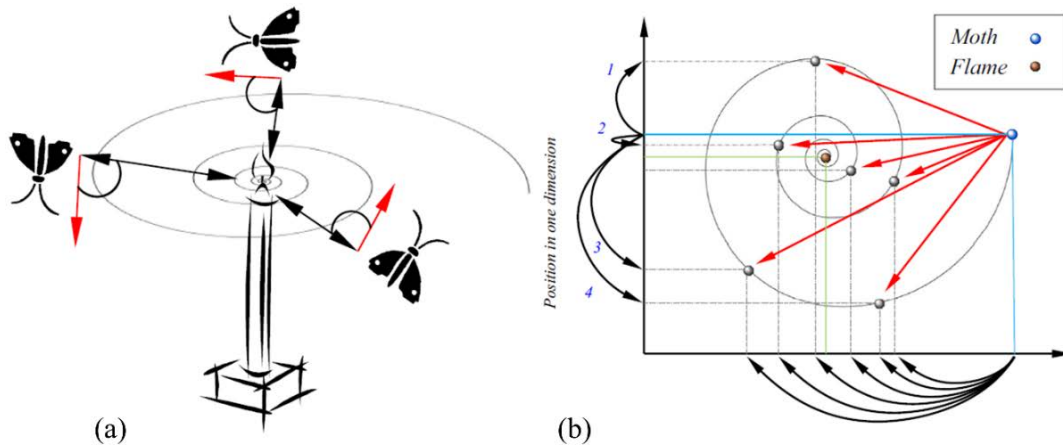
Figure 3.9 (a) Moth mechanism on the flame (b) Possible logarithmic spiral path of the moth with flame [247].

iii.    Soft besiege

Here $r \geq 0.5$ and $|E| \geq 0.5$, Prey jumps arbitrarily here and there to flee. This action can be explained in the following equations 3.72 and 3.73.

82

$$X(t + 1) = \Delta X(t) - E\big[JE_{prey}(t) - X(t)\big] \tag{3.73}$$

$$\Delta X(t) = X_{prey}(t) - E[\Delta X(t)] \tag{3.74}$$

Equation 3.73 and Equation 3.74 depict the exploits of this model. $\Delta X(t)$ indicates the distinction between the prey location and the current location of iteration t.

   iv.    Hard besiege

Here $r \geq 0.5$ and $|E| < 0.5$, Prey wear out and its present location is depicted in equation 3.74.

$$X(t + 1) = X_{prey}(t) - E[\Delta X(t)] \tag{3.75}$$

   v.    Soft besiege with progressive dive

In this stage, $|E| \geq 0.5$ and $r < 0.5$, Prey has sufficient energy to flee. Hawks' movement is described by equation 3.75

$$Y = X_{prey}(t) - E\big|X_{prey}(t) - X(t)\big| \tag{3.76}$$

   vi.    Hard besiege with progressive dives.

Here $|E| < 0.5$ and $r < 0.5$ prey not able to prey, hawk ambush and kill the Prey. For this challenging besiege, conditions are described in equations 3.76, 3.77 and 3.78

$$X(t + 1) = \begin{cases} Y & if\ F(Y) < F(t) \\ Z & if\ F(Z) < F(t) \end{cases} \tag{3.77}$$

$$Y = X_{prey}(t) - E\big|X_{prey}(t) - X_m(t)\big| \tag{3.78}$$

$$Z = Y + S * Lf \tag{3.79}$$

83
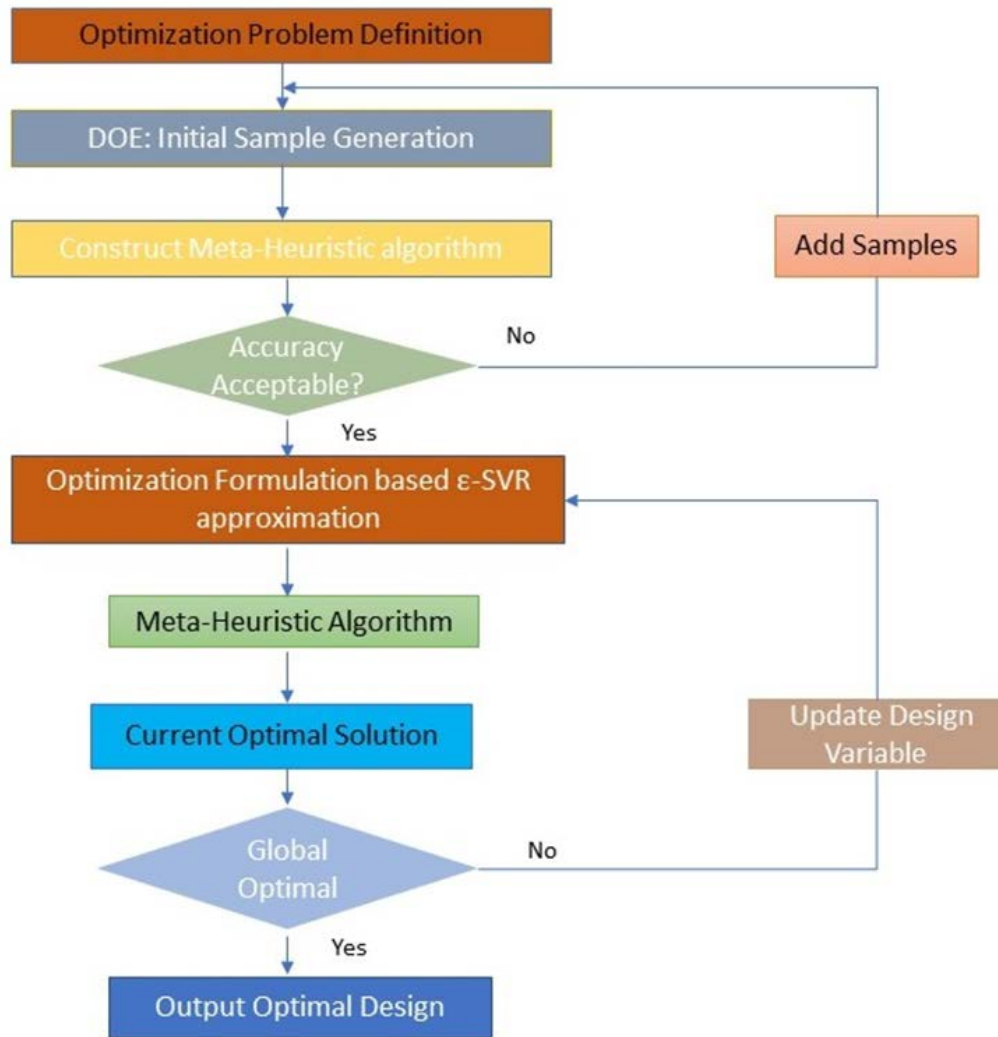
Figure 3.10 Optimization Flow Chart.

## 3.9    Multi-objective optimization

A multi-objective optimization issue is one in which numerous objectives are optimized at the same time. Figure 3.10. shows the flow chart for multi-objective optimization. This instance illustrates this approach in the following equation 3.80:

$$
\begin{cases}
Max: \eta = fn_1(Re, Bend.Twist) \\
Min: \Delta P = fn_2(Re.Bend, Twist) \\
\quad\quad Subject: \\
\quad\quad 0.05 \leq Re \leq 450 \\
\quad\quad 30^\circ \leq Model \leq 70^\circ \\
\quad\quad 1 \leq Twist \leq 4
\end{cases}
\tag{3.80}
$$

The term "Pareto-optimal solutions" refers to the various solutions that are generated by a problem that has several objectives. Within the context of a multi-objective optimization problem, solutions can be categorized as either dominated or non-dominated, depending on whether or not they are viable sets of solutions. When

84

determining dominance, the following requirements are considered: a design x1 is considered superior to another design x2 if it is superior to x2 in all goals and is superior to x2 in at least one objective. The Pareto-optimal set is comprised of all designs that are not dominated by any other design. The Pareto-optimal set's representation in functional space is called the Pareto-optimal front. It illustrates the trade-offs among conflicting objectives, allowing analysis of the compromises between designs. Since each solution in the Pareto-optimal set is globally optimal, none is superior to the others across all objectives. Therefore, selecting a Pareto-optimal solution that meets specific requirements depends on the designer's judgment.
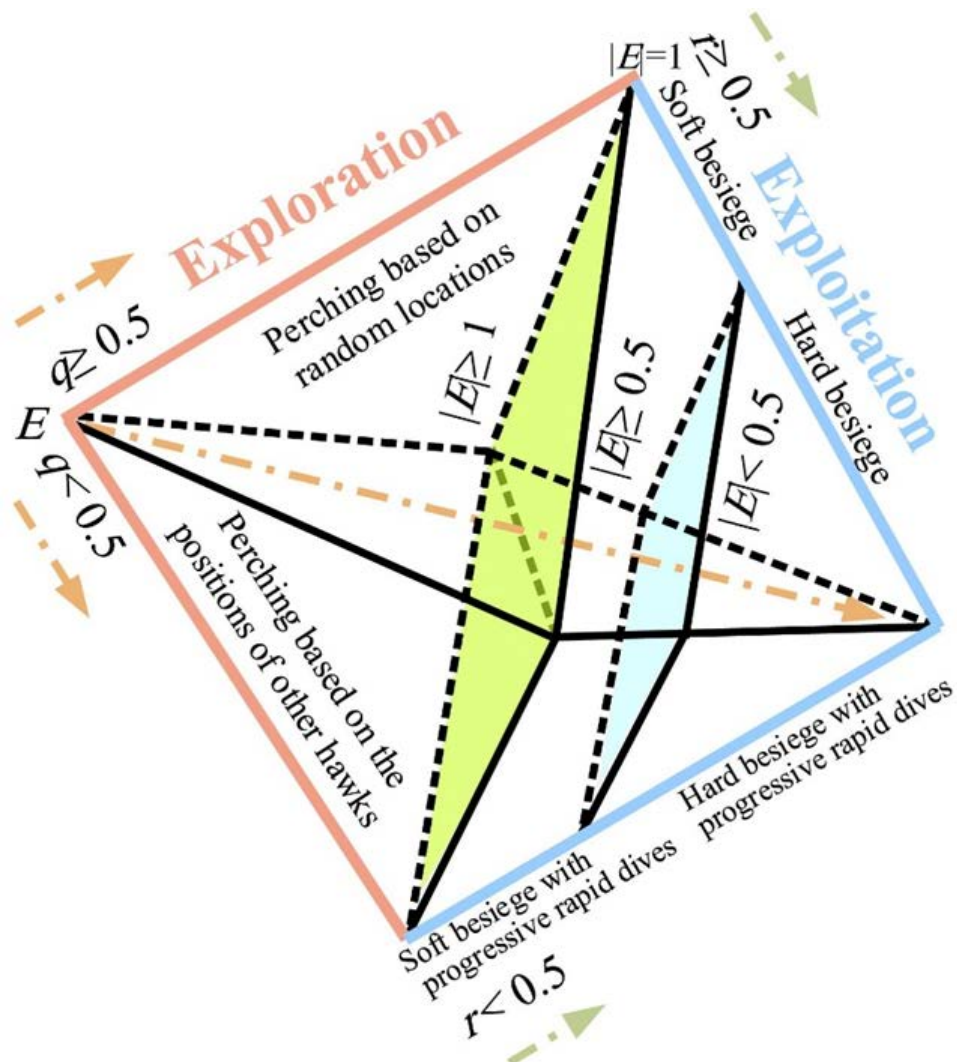


Figure 3.11 Various Stages of HHO [248]

Optimization of the MCHS is derived from meta-heuristic algorithms that were selected and coded in MATLAB software: Response Surface Methodology (RSM) and Haris Hawk Optimization (HHO), whose steps are shown in Figure 3.10 as a flowchart.

85

## 3.10    Summary of methodology

This chapter presents the computational framework and provides an in-depth analysis of numerical methods used to investigate fluid flow and heat transfer in microchannel heat sinks. The analyses are performed using both Eulerian and Lagrangian approaches, with a discussion on their respective advantages, limitations, and applicability to different thermal management scenarios. The chapter also addresses key aspects of numerical schemes, including discretization errors, mesh independence, and grid resolution requirements. Given the widespread use of commercial CFD software in thermal simulations, relevant modelling considerations specific to MCHS are outlined. The chapter concludes by detailing techniques for evaluating thermal performance, such as calculating temperature distribution and Nusselt number from computational data, thereby establishing a basis for assessing and optimizing various MCHS configurations. The chapter is organized into three main sections.

Multi-objective evolutionary algorithms (MOEA) aim to find the best trade-offs between conflicting objectives. However, real-world optimization problems (e.g., in engineering, finance, and AI) often involve expensive simulations or experiments. Surrogate modelling helps make MOEA more efficient by approximating complex functions.

# Chapter 4 RESULTS AND DISCUSSION

With an emphasis on improving thermal and hydraulic performance, this chapter discusses and examines the simulation results for various microchannel heat sink (MCHS) topologies. To evaluate the effects of geometric modifications on fluid mixing and heat transfer properties, a conventional MCHS design with square ribs with fillets and double fillets was first examined. A fractal microchannel heat sink (FMCHS) was then assessed employing various rib and cavity configurations with the goal of utilising surface area augmentation and flow disruption for improved thermal performance. Additionally, the application of $Al_2O_3$-water nanofluid in the FMCHS was investigated, emphasising the complementary impact of fractal-induced secondary flows and nanoparticle-enhanced thermal conductivity on overall performance. Ultimately, to determine the ideal design and operating parameters of the FMCHS while balancing pressure drop penalties and heat transfer enhancement, an optimisation framework incorporating Artificial Neural Networks (ANN) and Moth Flame Optimisation (MFO) was put into place. The results are thoroughly examined, contrasting thermal resistance, pumping power, Nusselt number, and performance enhancement criteria (PEC) in each scenario.

## 4.1    Conventional MCHS

### 4.1.1 Validation of the results of conventional MCHS

Pressure drop in a simple MCHS in region of laminar flow is computed as [249]:

$$\Delta P = \frac{2(fRe)\mu_f u_m L_T}{D_h} + \frac{K\rho_f u_m^2}{2} \tag{4.1}$$

When the Hagenbach factor and Poiseuille number (fRe) are represented as:

$$Po = fRe = 24(1 - 1.3553\,\alpha_c + 1.9467\,\alpha_c^2 - 1.7012\,\alpha_c^3 \tag{4.2}$$
$$+ 0.9564\alpha_c^4 - 0.2537\alpha_c^5)$$

$$K = 0.6796 + 1.2197\alpha_c + 3.3089\alpha_c^2 - 9.5921\alpha_c^3$$
$$+ 8.9089\alpha_c^4 - 2.9959\alpha_c^5 \tag{4.3}$$

Where, $\alpha_c$ (aspect ratio of the channel) = width /height

Theoretical findings have been matched with the current numerical findings of an S-MCHS in Figure 4.1. Equation 4.1 is used to compute the pressure drop. The numerical data and the theoretical data [250] show good agreement. Therefore, the

88

performance of ribbed MCHS with filleted ribs is presently being evaluated using the current numerical approach.
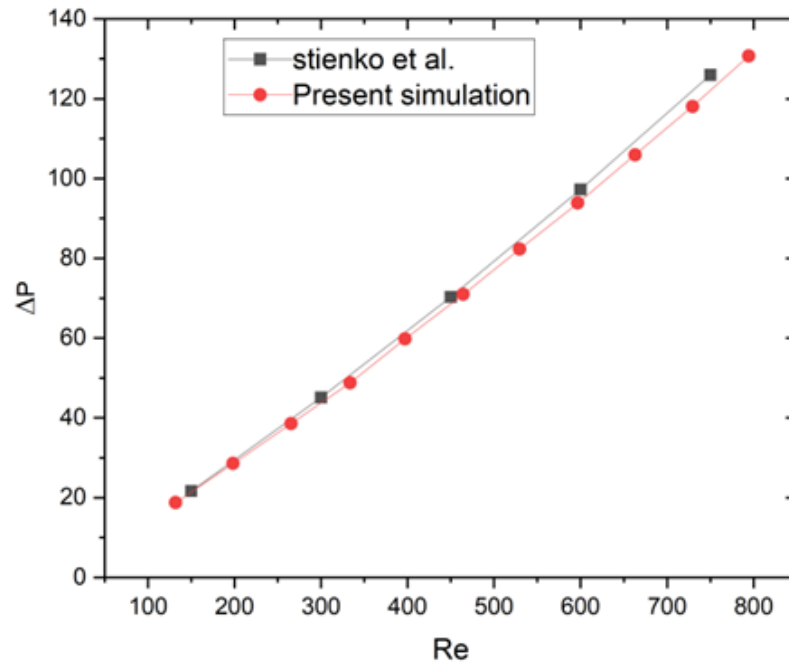


Figure 4.1 Comparison of pressure drop predictions made by the theoretical correlations of Steinke et al. [250] and current simulation result.

### 4.1.2   Effect of filleted ribs behaviour of fluid flow
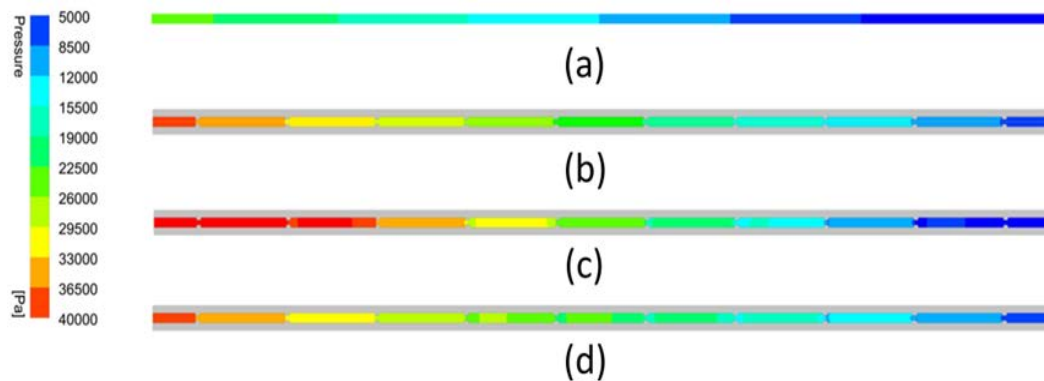


Figure 4.2 Pressure contour for MCHS with various geometrical arrangement in x-z plane (a) S-MC (b) MC-SQ (c) MC-SQ-FR, and (d) MC-SQ-DFR

This part of the study is devoted to evaluating the hydrodynamic analysis of MCHS with various geometrical designs, including MC-SQ, MC-SQ-FR, MC-SQ-DFR, and S-MC. This is because the flow field is crucial to the effectiveness of MCHS. Figure 4.2, illustrates the pressure distribution in MC-SQ, MC-SQ-FR, MC-SQ-DFR, and S-MCHS configurations in x-z plane at the mid of the channel height at inlet velocity of 1.5 m/s. While vortices development increases pressure loss in ribbed arrangements, friction losses along the channel cause a linear pressure

89

reduction in S-MCHS. The fluid flow increases, and the pressure begins to drop as soon as the water flow constricts and enters the channel's convergent region. On the other hand, when the fluid expands after leaving the channel's converging section, its velocity decreases and its pressure steadily rises.
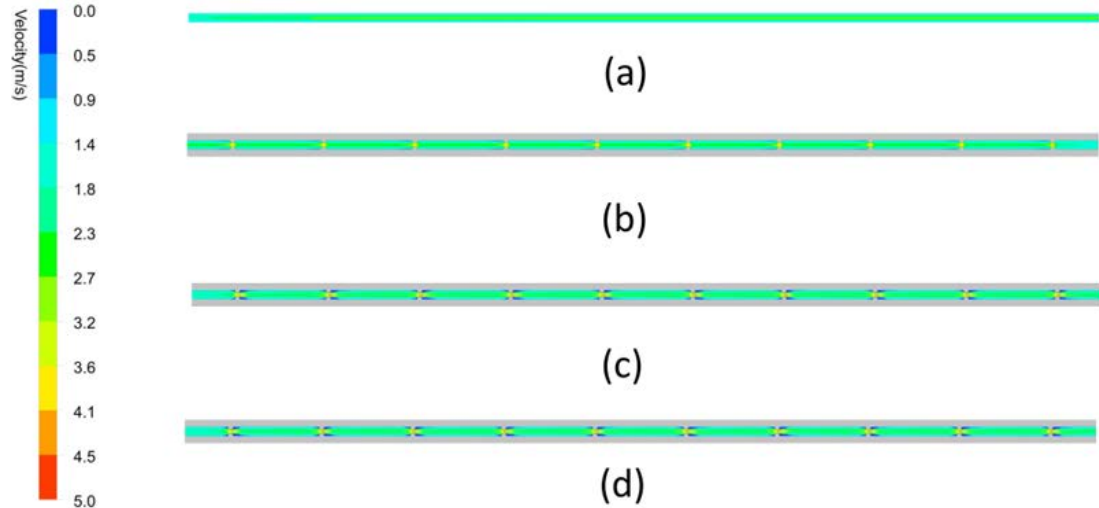


Figure 4.3 Velocity contours for different MCHS in x-z plane (at the mid height of channel) and u=1.5 m/s for (a) S-MC (b) MC-SQ (c) MC-SQ-FR, and (d) MC-SQ-DFR.

Figure 4.3, shows effects of different ribs configuration on velocity distribution along microchannels length in x-z plane (at the mid height of channel)) at 1.5 m/s of inlet velocity for different configurations. Ribs inside the MCHS dramatically change the velocity distribution, as depicted. Fluid velocity continuously rises and falls as it flows through the length of ribbed microchannels because their surface cross-section area rapidly reduces and increases. The inter-ribs region of microchannels with ribs has the highest velocity. The velocity gradient at the ribs is also improved in the direction normal to the microchannel wall, which indicates improved blending of the centre cold fluid and the near-wall hot fluid. This value is highest for MC-SQ-FR when compared to other variants. A stagnation zone with low thermal performance is created due to low velocity downstream of the ribs. In this area, recirculating streamlines are also seen. The way the ribs are shaped directly affects how these vortices develop. In contrast to MC-SQ and S-MCHS, where greater vortices occur, both MC-SQ-FR and MC-SQ-DFR have smaller stagnation zones in the downstream due to the presence of fillets in the rib corners. The thermal boundary layer thickness declines, mixing is enhanced, and the thermohydraulic performance of MCHS is improved as a result of the disruption of the boundary layer, creation and growth of secondary flows etc.

90

Figure 4.4 also depicts the local pressure variation throughout the MCHS length (z axis) at an inlet velocity of 1.5 m/s to help with understanding the pressure drop within the microchannels. It turns out that the pressure difference in ribbed microchannel heatsinks is larger than that in S-MCHS. Varied rib shapes result in varied pressure drops as a result of the flow's differing behaviour as it expands and contracts in the space between the ribs. Figure 4.4, shows that the pressure loss varies in the fluid flow direction for all designs when the ribs are inserted into the microchannels.
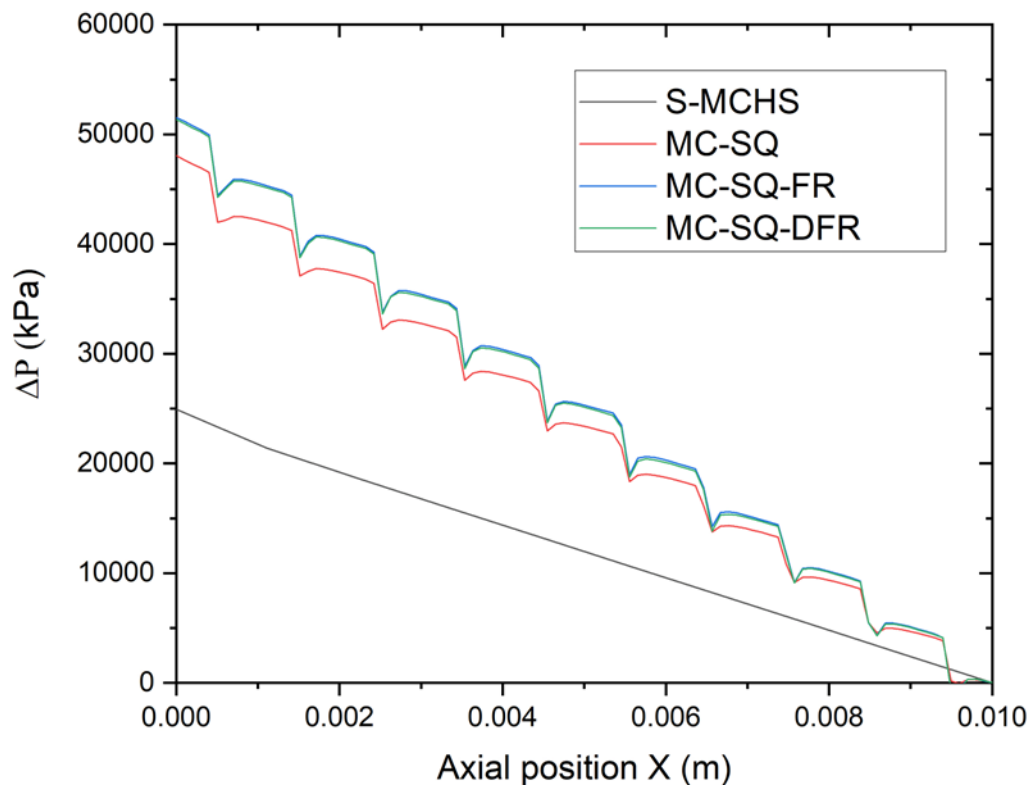


Figure 4.4 Variation in the drop in pressure along the MCHS's centre line for channels with various geometrical configurations at 1.5 m/s inlet velocity.

### 4.1.3 Effect of fillets at rib corner on heat transfer

Figure 4.5 depicts the temperature contour along the channel length for all design. In comparison to all other configurations, the temperature is higher in S-MCHS because of the growth of the thermal boundary along the fluid flow. The temperature difference between the centre and the channel walls is significantly reduced when ribs are present inside the channels. Due to the efficient mixing of centre colder fluid and near-wall hot fluid, this temperature reduction is realised. Additionally, the coolant stagnation zone downstream of the ribs, where the temperature is nearly identical to the adjacent wall, exhibits a reasonably uniform temperature distribution.

91

Reduced fluid velocity and inadequate fluid mixing are to blame for the region's decreased heat transfer rate. Combining ribbed structures with filleted corners improves heat transfer compared to MC-SQ in both MC-SQ-FR and MC-SQ-DFR configurations. As pointed out in the section above, different MCHS designs result in varied velocity and pressure distributions, which affect the heat transfer performance. Figure 4.6a shows that when ribbed MCHS is employed instead of simple microchannels, the bottom surface's maximum temperature is significantly lower. The bottom surface temperature has a big impact on how long micro-electric devices last and how well they work. Lower base temperature ($T_b$) implies that ribs can significantly improve heat transfer coefficient. The mean temperature was lower in both the ribbed MCHS with filleted ribs (MC-SQ-FR and MC-SQ-DFR) than in all other configurations.
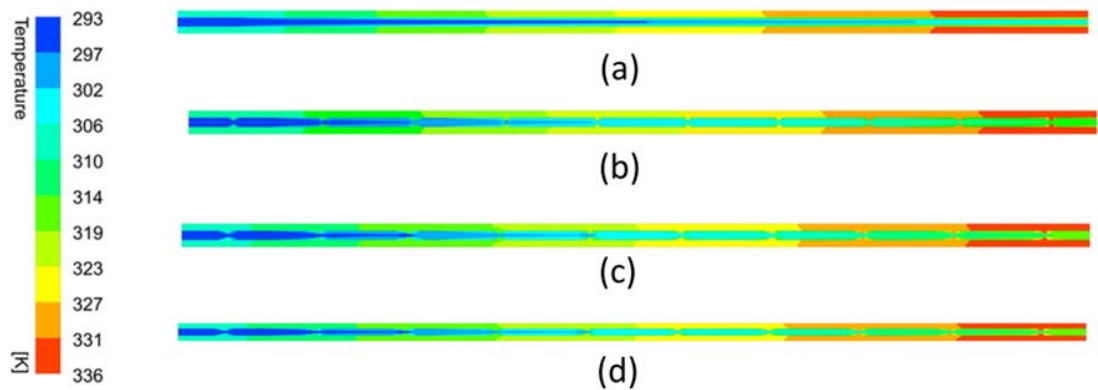


Figure 4.5 Temperature contour for MCHS with different geometrical configuration and inlet velocity of 1.5 m/s for (a) S-MC (b) MC-SQ (c) MC-SQ-FR, and (d) MC-SQ-DFR.

Figure 4.6b depicts the variation of the mean Nu for all geometrical configurations as the inlet velocity varies within the range of 0.5-3 m/s. Corresponding Re is 66<Re<396. When Re ≤132, the average heat transfer coefficient for both filleted ribs configurations are nearly similar. However, when Re > 132, the use of fillets at corners in both the configurations raises Nu and lowers the surface temperature at the bottom of the heat sink. Within the investigated range of Re, the increase in Nusselt numbers for the MC-SQ, MC-SQ-DFR, and MC-SQ-FR configurations are 5-47%, 25-52%, and 25-58%, respectively. Therefore, it may be said that filleted ribs operate better as a heat sink. The improvement in thermal performance for MCHS with ribs and fillets at the corner of the ribs, can therefore be described as: The use of ribs and fillets in

92

ribs improves the heat transfer area and the rate of heat transfer between fluid and substrate material.

When ribs and filleted ribs are used, they create vortices inside microchannels, which improves the heat transfer coefficient. After contracting, fillets reroute the fluid flow towards the channel walls, temperature decreases along the channel wall as depicted in Figure 8.
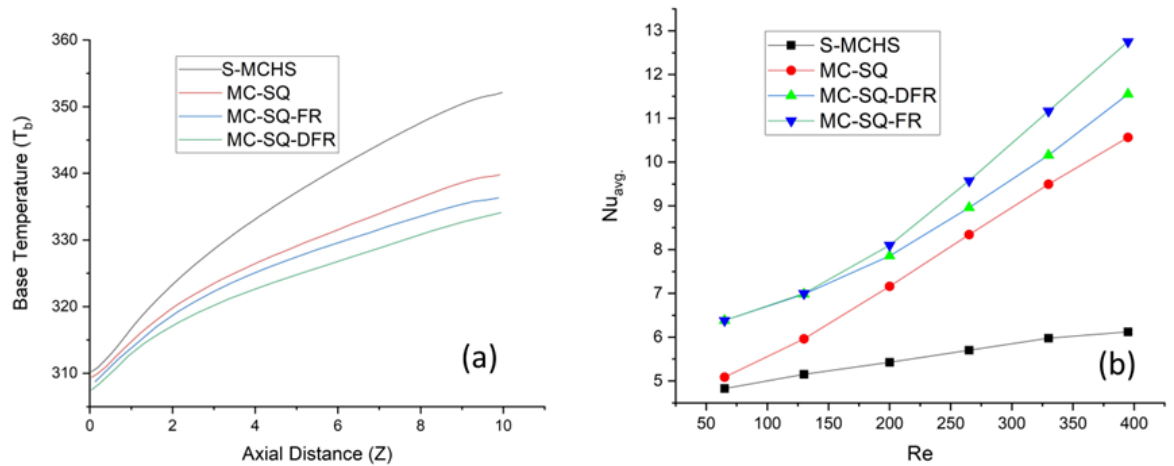


Figure 4.6 (a)Temperature distribution over the axial length (mm) of bottom surface of the MCHS (b) Average Nu variation in microchannels with various geometrical arrangements.

## 4.2  Thermohydraulic performance of FMCHS

Different thermal and hydraulic performance parameters have been critically analyzed and discussed in this section. Volumetric flow rates of 200 ml/min to 400 ml/min are chosen in this study.

### 4.2.1 Validation

The experimental findings of Xu et al. [197] is used to validate the numerical results and confirm the current study's correctness. The experimental setup includes a liquid reservoir, a microchannel specimen, a gear pump, a pump, a strainer, a liquid trap, and a pressure and temperature tester. A cartridge heater was utilized to deliver a consistent heat flux in the aluminium block. Previously investigated heat transfer and fluid flow in the FMCHS, and a comparison between the pressure drop and temperature is shown in Figure 4.7. As depicted, the current study and the experimental data show the same trend, indicating the correctness of the numerical approach used in the current study.

93

Figure 4.7b indicates that the maximum error, as shown by the error bars, is below 2.28%. Similarly, Figure 4.7a demonstrates that when compared with the results of Xu et al. [197], the maximum error is less than 2.61%. Moreover, the numerical results in both Figure 4.7a and Figure 4.7b exhibit a consistent pattern and are in good agreement with the experimental data.
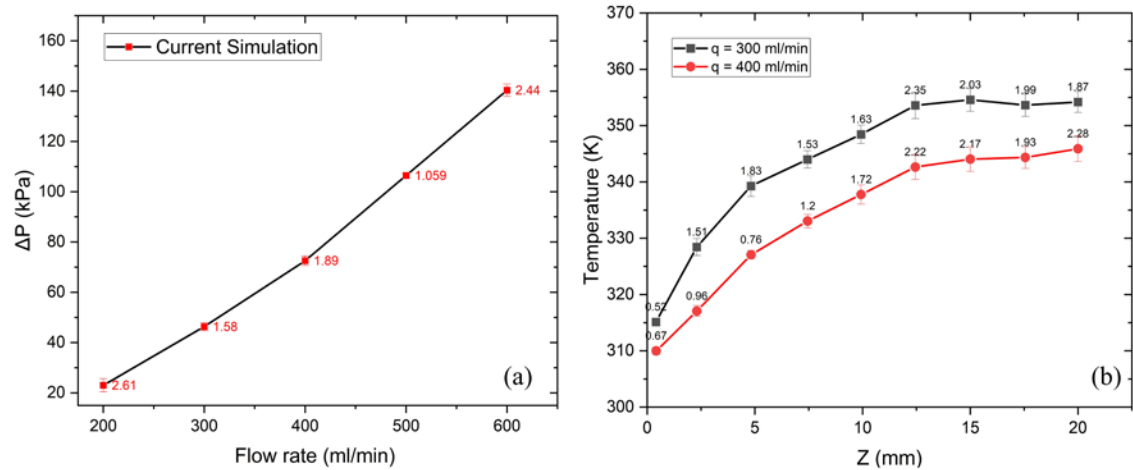


Figure 4.7: Error bar depicting the deviation of current simulation data from Xu et al. [197] (a)Variation of pressure drop vs flow rates, and (b) wall temperature along the channel length.

### 4.2.2 Flow performance

Parameters involved in the fluid flow influence the thermohydraulic performance in MCHS. These characteristics are examined in detail in this study. The velocity contours of all the models are shown in Figure 4.8. These contours are taken at half the channel depth at the volumetric flow rate of 350 ml/min. highest velocity is seen at the center of the MCHS, and the lowest velocity is seen near the sidewall of the primary channel in FMCHS-P, as illustrated in Figure 4.8a. As the cooling fluid streams into the branching channel, its peak velocity relocates towards the inner sidewalls, creating a stagnation zone near the outer sidewall. This effect enhances heat transfer on the inner sidewall compared to the outer sidewall due to fluid flow through the subsequent branches. These whole phenomena increase the heat transfer efficiency.

94
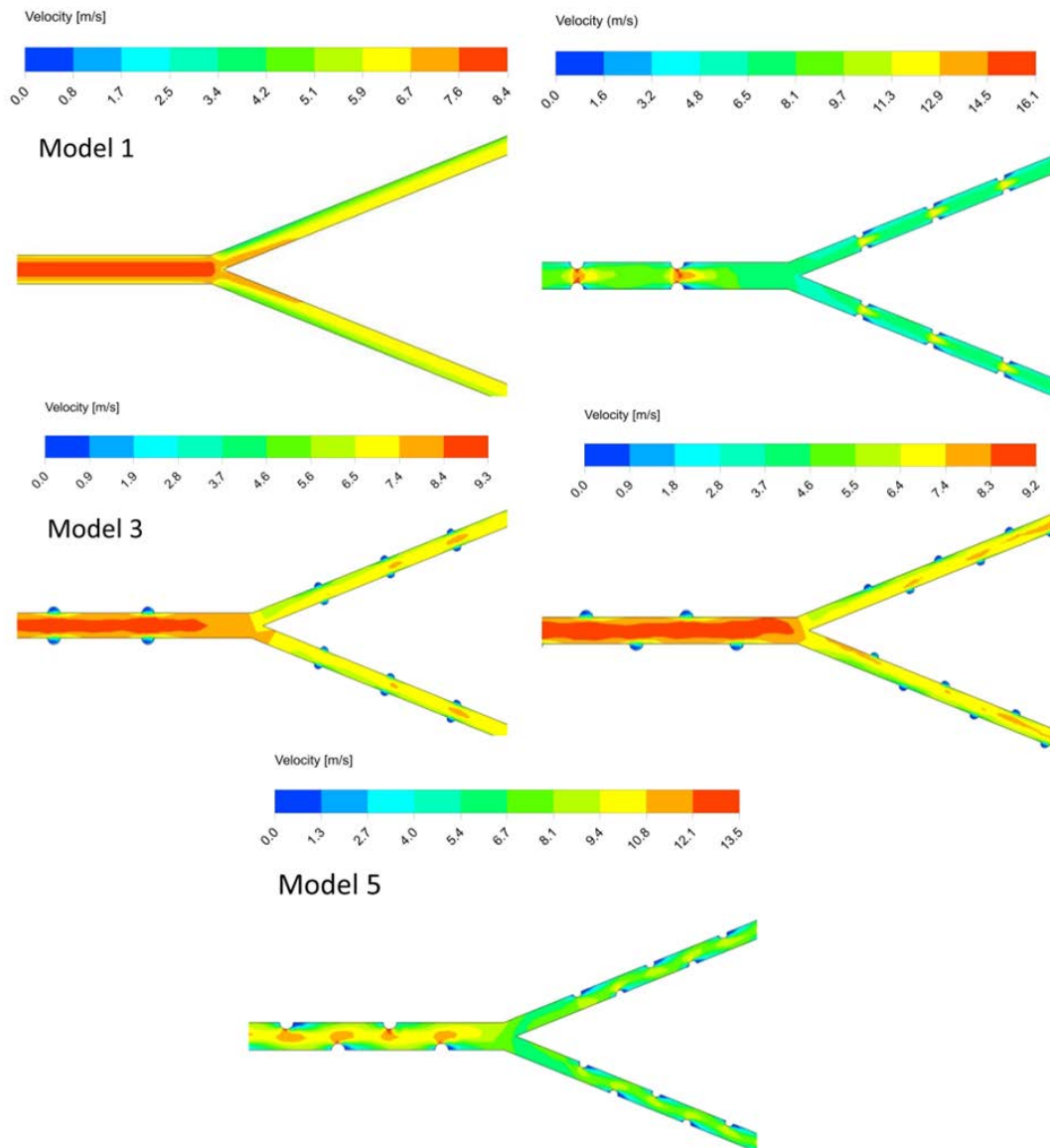
Figure 4.8: Velocity contour at center plane of the channel height at q=350 ml/min (branching level k=0,1).

Velocity contours of FMCHS-R and FMCHS-DR are shown in Figure 4.8b and Figure 4.8e. Maximum velocity rises closer to the ribs. This is due to the flow restriction in the fluid path, which leads to sharp increases in the fluid velocity. This increment in the velocity is more profound in FMCHS-R than in FMCHS-DR, where the flow path is partially restricted due to the diagonal position of the ribs. Thus, the maximum velocity value is less than the FMCHS-R. The velocity curve along the channel k=0,1,2, and 3, as shown in Figure 4.9, depicts that the magnitude of velocity fluctuation is more rapid in FMCHS-R, whereas FMCHS-DR shows comparatively less fluctuation. When cavities are added to the channel, the cross-sectional area increases locally. However, during fluid flow, cavities cause the fluid to swirl and

95

mix, creating secondary flows in the cavity. Higher localized velocity and better heat transfer are the outcomes of these secondary flows.

Furthermore, it is worth noting that the inclusion of ribs in both models, i.e., in FMCHS-R and FMCHS-DR, not only increases the flow velocity but also alters the flow direction, speeding up the development of fluid flow.  As far as the FMCHS-C and FMCHS-DC are concerned, the inclusion of creation leads to the creation of a localized flow recirculation zone, which leads to the continuous formation and destruction of the boundary layer. This phenomenon also induces the creation of secondary flow recirculation within these regions, facilitating the constant transfer of heat at the boundary to the main flow and contributing to the conversion of fluid resistance with solid to fluid-fluid resistance. Thus, the inclusion of a cavity can efficiently improve heat transfer. Notably, the stagnation zone has expanded in both FMCHS-C and FMCHS-DC. Therefore, it hampers the heat transfer from the outer sidewalls and enhances it near the inner sidewalls. Moreover, FMCHS and FMCHS-DC show steady velocity fluctuations compared to their ribbed counterparts, thus minimizing the loss.
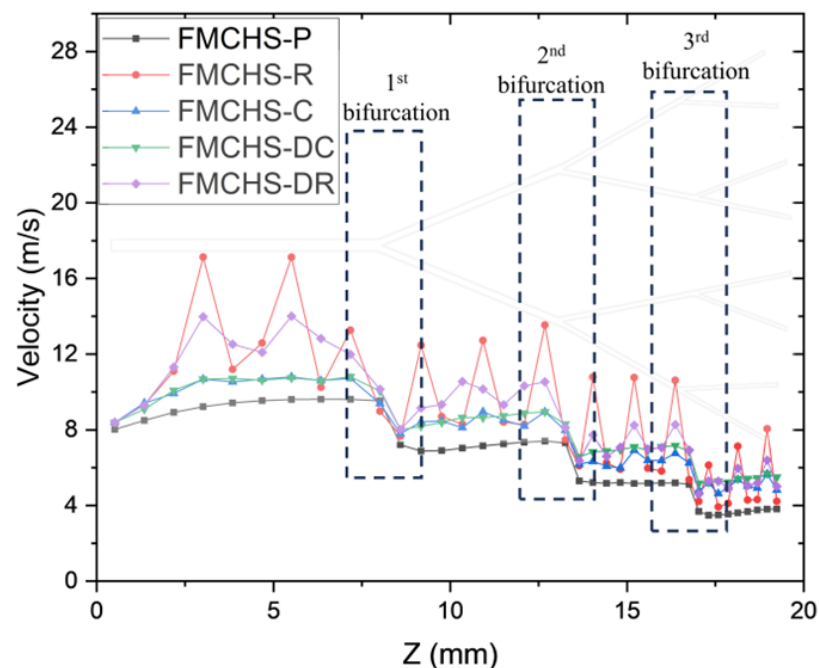


Figure 4.9: Plot of velocity vs axial length (Z) along the channel length at q=400 ml/min.

### (a) Pressure drops and thermal resistance.

Figure 4.10 shows the pressure distribution at q=200 to 400 ml/min along the channel length (k=0,1,2,3). Pressure loss in the microchannel is evident due to the

96

frictional losses. Modified flow direction and expanding flow channels are prominent reasons for pressure drop along the flow direction of the channel apart from the flow resistance; as can be seen in Figure 4.10a, at branching nodes, there is an increase in the pressure to the turning effect and also because of the abrupt fall in the velocity at the node. After adding cavities, the main flow channel experiences a jet shrinkage action, creating an adverse pressure gradient and secondary flows. This generation of secondary flows converts the solid-fluid resistance to the fluid-fluid resistance, which leads to a decrease in the pressure drop. Introducing cavities within the primary channel may lead to a slight pressure drop decrement, but the uneven pressure distribution can ultimately raise the overall pressure drop. This results in an increment in pressure drop in FMCHS-C and FMCHS-DC compared to FMCHS-P. As evident from Figure 4.10b, the incorporation of ribs in the flow channel has a more significant impact on the pressure drop than the cavity. The total pressure drop of all models with flow rate configuration is presented in Figure 4.10a. This gives a clearer picture of the pressure drop scenarios for all models. The FMCHS-P has the lowest pressure drop, whereas FMCHS-C and FMCHS-DC have the same $\Delta$P plot, i.e., it hardly differs when moving along the channel length. Pressure drops in ribbed configuration, i.e., FMCHS-R and FMCHS-DR, are much more extensive than other configurations. As evident from the figure, the pressure drop also grows when the flow rate rises.
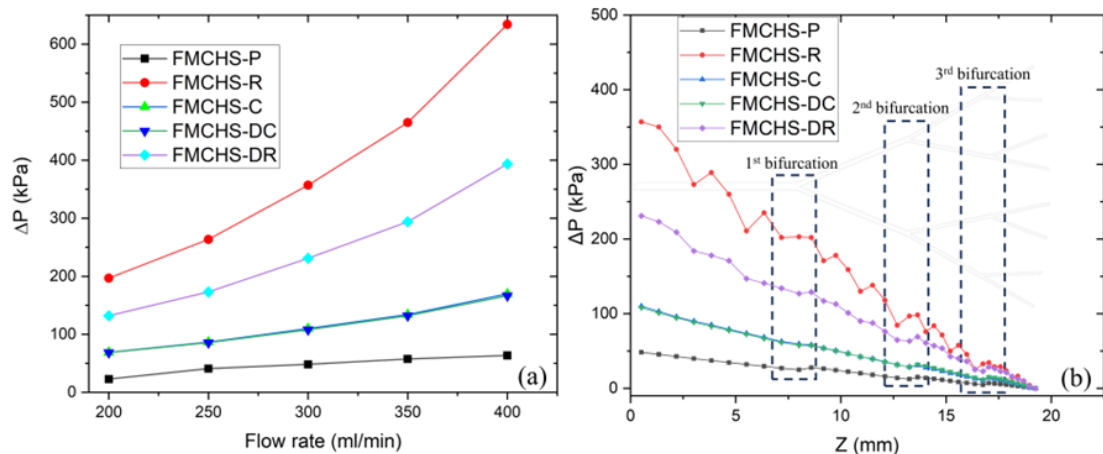


Figure 4.10: Plot of (a) pressure drop vs flow rate and (b) pressure drop vs Z at the flow rate of 300 ml/min.

Figure 4.11 shows the variation of thermal resistance with the flow rate. FMCHS-P shows the highest thermal resistance with $R_{th}$ = 1.57 K-cm$^2$/W). A monotonic decrease in thermal resistance was seen as the flow rate increased. In the case of FMCHS-DC, thermal resistance is lower than FMCHS-P but higher than the

97

remaining configurations. FMCHS-DR has the least $R_{th}$. However, this difference is very minimal.
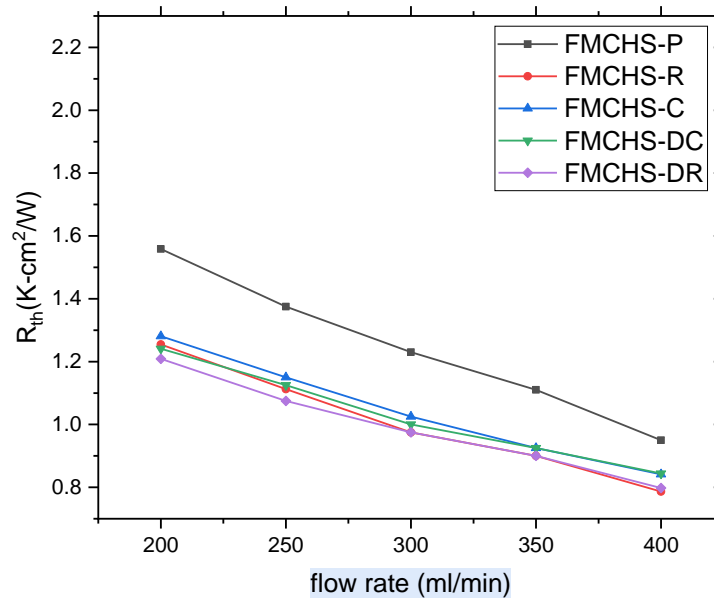


Figure 4.11 : Variation of thermal resistance with flow rate.

### 4.2.3 Thermal performance analysis

### (a) Temperature distribution
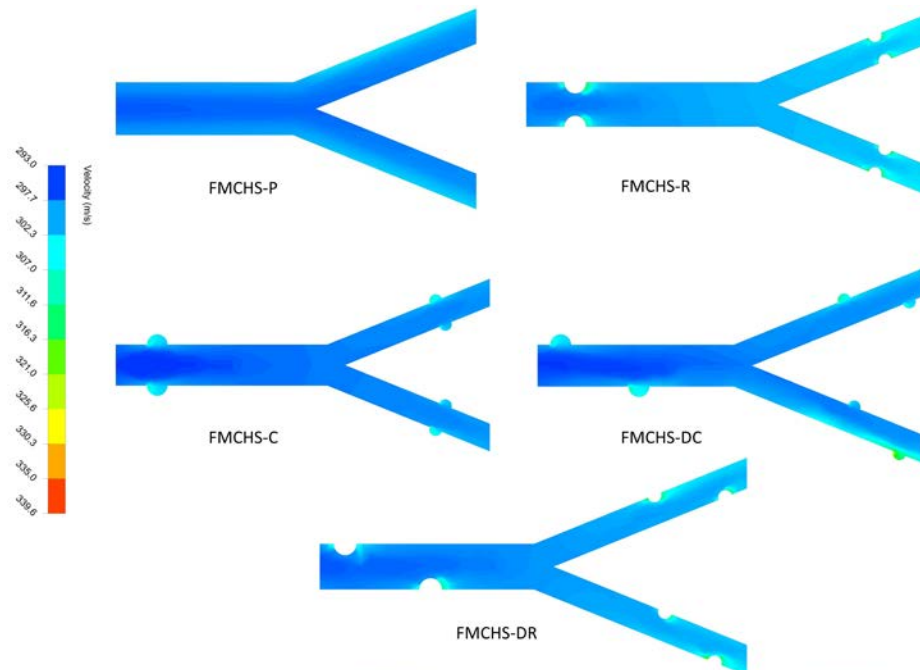


Figure 4.12 : Temperature contour along the central planes of the channels at q= 350 ml/min for various configurations at branching levels k=0, 1.

The temperature contour taken from half of the microchannel height with varying Z at the flow rate of 400 ml/min is depicted in Figure 4.12. There are temperature

98

gradients, with the MCHS walls experiencing higher temperatures and the channel center experiencing relatively lower temperatures. Due to the increased stagnation zone, a relatively small temperature gradient exists at the outer sidewall as the fluid passes through the channel branch after the main channel. When cavities are created, a high-temperature gradient exists near the cavity due to thermal boundary layer redevelopment. Furthermore, secondary flow generation causes the transfer of hot fluid from the boundary to the main channel, resulting in a slightly higher temperature at the outlet in the primary flow channel compared to FMCHS-P.
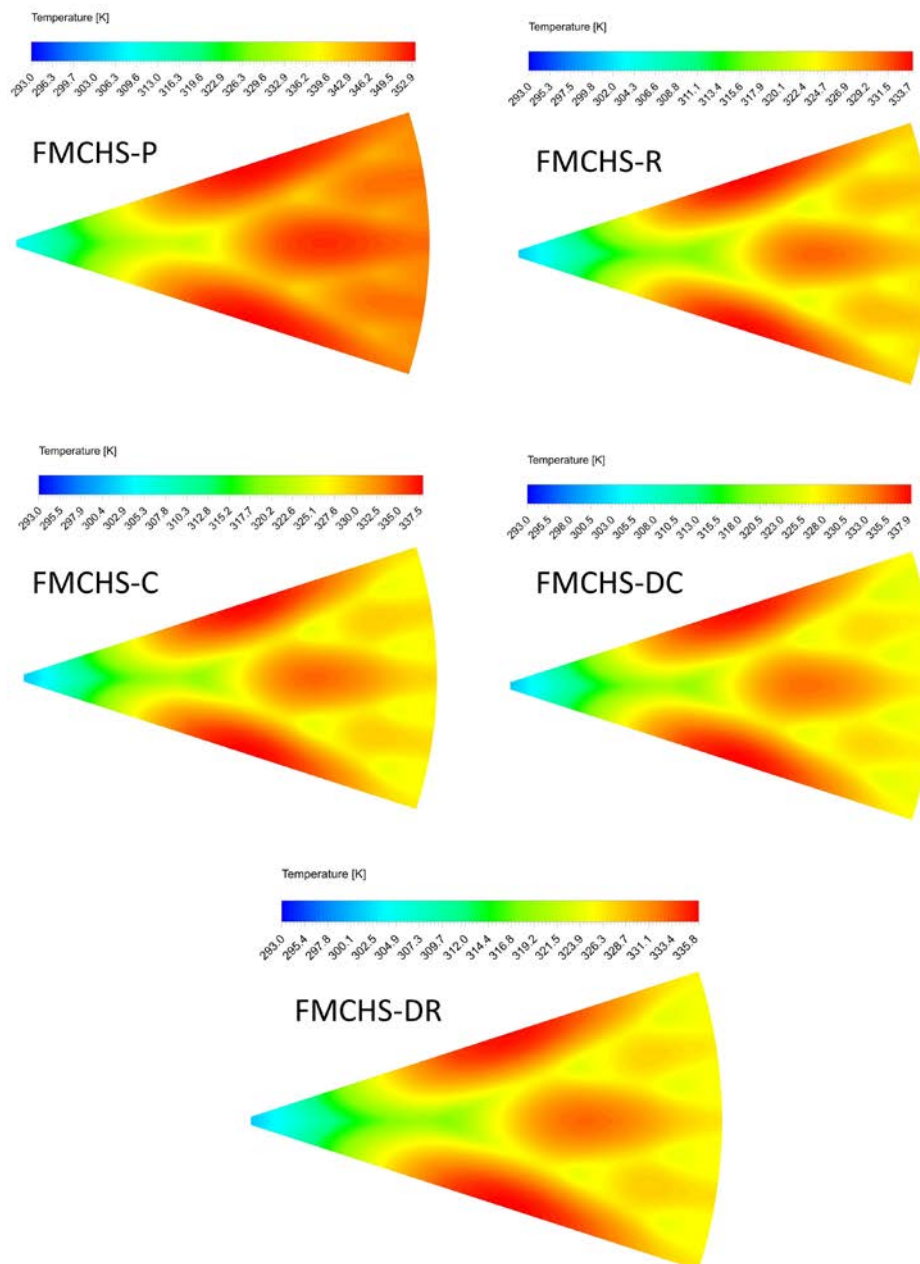


Figure 4.13: Temperature contours across the base wall of the FMCHS at q= 400 ml/min for various configurations.

99

Figure 4.12b and Figure 4.12c shows the temperature contour for FMCHS-R and FMCHS-DR. As observed, the temperature difference between the center and walls decreases as ribs in the main channel create constriction and expansion effects, leading to increased velocity. Hence, flow recirculation was established to mitigate this temperature variation. This results in better heat transfer efficiency due to lower thermal resistance. FMCHS-R and FMCHS-DR have substantial impacts on heat transfer compared to other models. The ribbed configuration also helped maintain uniform temperature gradients in the channel. Figure 4.13 depicts the temperature contour at the FMCHS base at q = 400 ml/min. To understand the FMCHS's performance, the temperature uniformity at the base must be examined. Lower base temperatures and more consistent base wall temperatures result from the addition of ribs and cavities.

**(b) Nusselt number**

Nusselt number vs. flow rate plot shown in Figure 4.14 demonstrate that FMCHS-R and FMCHS-DR have the highest Nu in this configuration for all flow rate ranges. This increase in Nu is prominent at higher flow rates. This indicates that heat transfer is more favourable at higher flow rates.
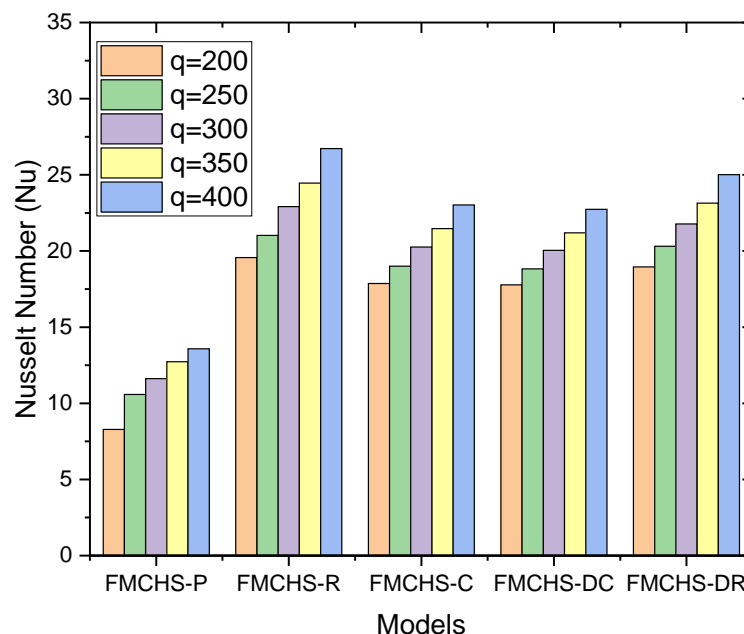


Figure 4.14: Nu at different flow rates for all the models.

**(c) Comprehensive performance**

The best heat transfer efficiency has been reported in FMCHS with ribbed designs, albeit at the expense of significant pressure drops. So, we need to have a performance

100

analysis parameter that asses the thermal performance as well as pressure drop. The FMCHS's overall performance is examined using performance evaluation criteria (PEC). Figure 4.15a depicts the plot of PEC vs flow rate. With the rise in flow rate, PEC also increases. This indicates that with the higher inlet velocity, FMCHS with ribs and cavities in all arrangements will perform better. The reason is that high velocity leads to secondary flow generation; hence, the heat transfer effect dominates over the viscous effect of fluid. It is also worth noting that when the flow rate is less than 300 ml/min, the PEC value of FMCHS-R is less than 1, which suggests that although the thermal performance of FMCHS-R is highest among all, but comprehensive performance is worse than FMCHS-P. However, FMCHS-DR shows PEC>1 in all flow rate ranges and performs better than FMCHS-R. FMCHS-C and FMCHS-DC give better comprehensive performance than their ribbed counterpart.

Figure 4.15b shows that with increased pumping power, Nu increases, and hence heat transfer performance increases. At low pumping power, i.e., $\Omega<150$ mW, the Nu value is more significant for FMCHS-C and FMCHS-DC, followed by FMCHS-DR, FMCHS-R, and FMCHS-P. However, when $\Omega>200$ mW, the Nu of FMCHS-DR is highest, but after $\Omega>300$ mW, FMCHS-R dominates and has the highest Nu. This concludes that FMCHS-C and FMCHS-DC are better choices at lower pumping power, and at higher pumping power, FMCHS-R is a better choice. In the intermediate range of pumping power, FMCHS-DR is a better choice.
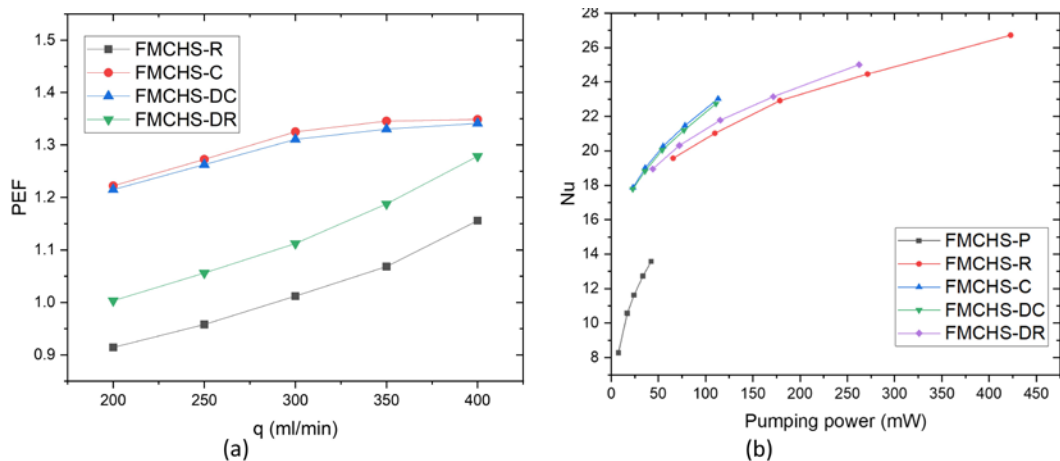


Figure 4.15: Variation of (a) PEC vs q; (b) Nusselt number vs Pumping power.

## 4.3    Effects of nanofluid on thermohydraulic performance of FMCHS

The results of the fractal microchannel heat sink (FMCHS) using an $Al_2O_3$-water nanofluid as the working fluid are discussed in this section, with a focus on how it affects flow behaviour and heat transfer. When combined with the fractal design, the

101

use of Al$_2$O$_3$ nanoparticles greatly increases the base fluid's thermal conductivity, which facilitates more efficient heat dissipation by increasing convective heat transfer and disrupting flow. Under various Reynolds numbers and nanoparticle volume fraction, the results are examined in terms of Nusselt number, pressure drop, wall temperature, and overall performance evaluation criteria (PEC). The trade-off between improved heat transfer and pressure drop brought on by the nanofluid's enhanced viscosity is given special consideration. Performance comparison with water-based FMCHS is also covered, emphasising the circumstances in which Al2O$_3$ nanofluids provide the best thermohydraulic results. Figure 4.16 represent the simple FMCHS model used in this study.
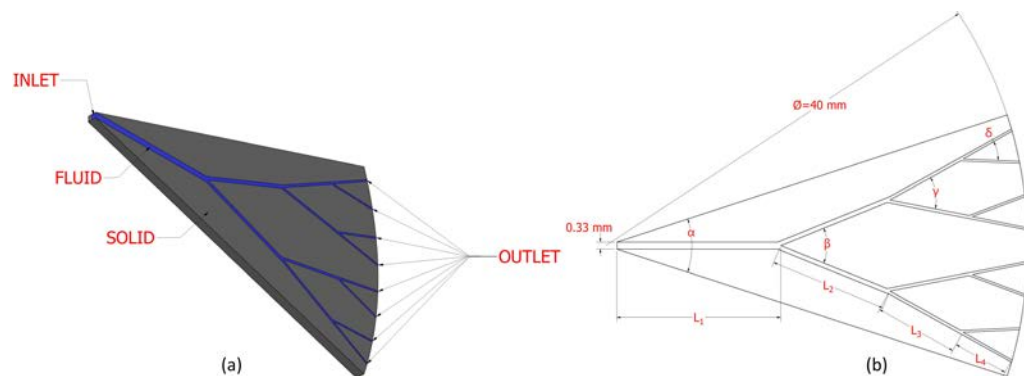


Figure 4.16 Model of the 3-D FMCHS, including its geometry and schematic perspective.

### 4.3.1 Validation of the result
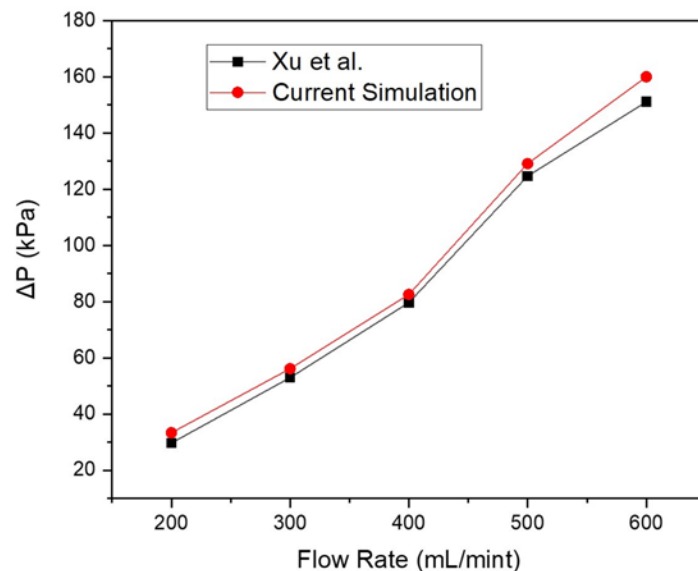


Figure 4.17 Comparison of pressure drop value with experimental data and simulation findings.

The present numerical result is juxtaposed with the experimental findings of Xu et al [197]. The thermohydraulic performance of FMCHS was examined through both

102

experimental and numerical methods by the researchers. Figure 4.17 illustrates the comparison of pressure drop across varying volume flow rates.   The current simulation results are in close agreement with the experimental data, demonstrating the accuracy of the present numerical study.

### 4.3.2 Effect on Wall temperature

Figure 4.18 depicts, for pure water, how the Reynolds number affects the distribution of wall temperatures along paths L1, L2, L3, and L4. The wall temperature rose along the course, as can be observed. In other words, when the fluid and wall temperatures declined along the path, the rate of heat transfer also decreased. The last branch (L4) experiences the highest temperature, as shown in Figure 4.18 where the entrance wall temperature is lower than the output temperature. This effect is caused by the path's decreased mass flow rate due to the flow being divided between the branches, which reduces heat dissipation and raises the temperature of the channel wall. Additionally, Figure 4.18 can be used to assess the impacts of the Re on the temperature variation along the channel. The heat transfer coefficient rises with increasing fluid velocity. Additionally, delaying the development of the thermal boundary layer is a result of lengthening the cooling fluid's development time. By raising the fluid's velocity in response to this behaviour, the temperature of the walls has been dramatically lowered; for water, the maximum temperature at Re = 1,500 is 380 K, while the maximum temperature at Re = 3,000 is 348 K.
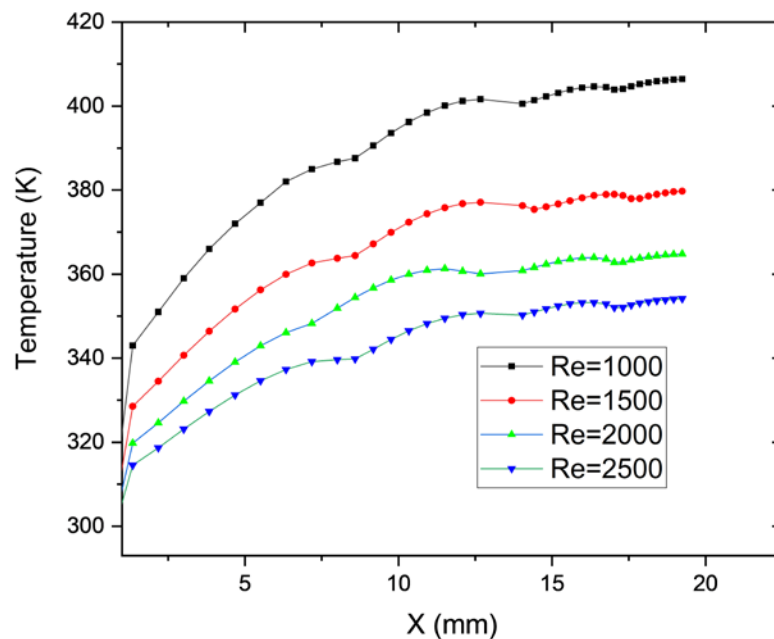


Figure 4.18 Wall temperature distribution along the channel length at different Reynolds number.

103

Figure 4.19 shows the impact of introducing $Al_2O_3$ nanoparticles to the base fluid i.e. water with φ=4% and at Re values between 1,500 and 3,000 on the wall temperature distribution. As shown in the addition of solid nanoparticles improves the thermophysical characteristics of the cooling fluid, such as thermal conductivity, which results in better heat dissipation. Lowering the temperature gradient is caused by increasing fluid velocity (Re) at a certain volume percent of solid nanoparticles. As a result, the maximum temperature of the wall will decrease, and its temperature distribution will be uniform.
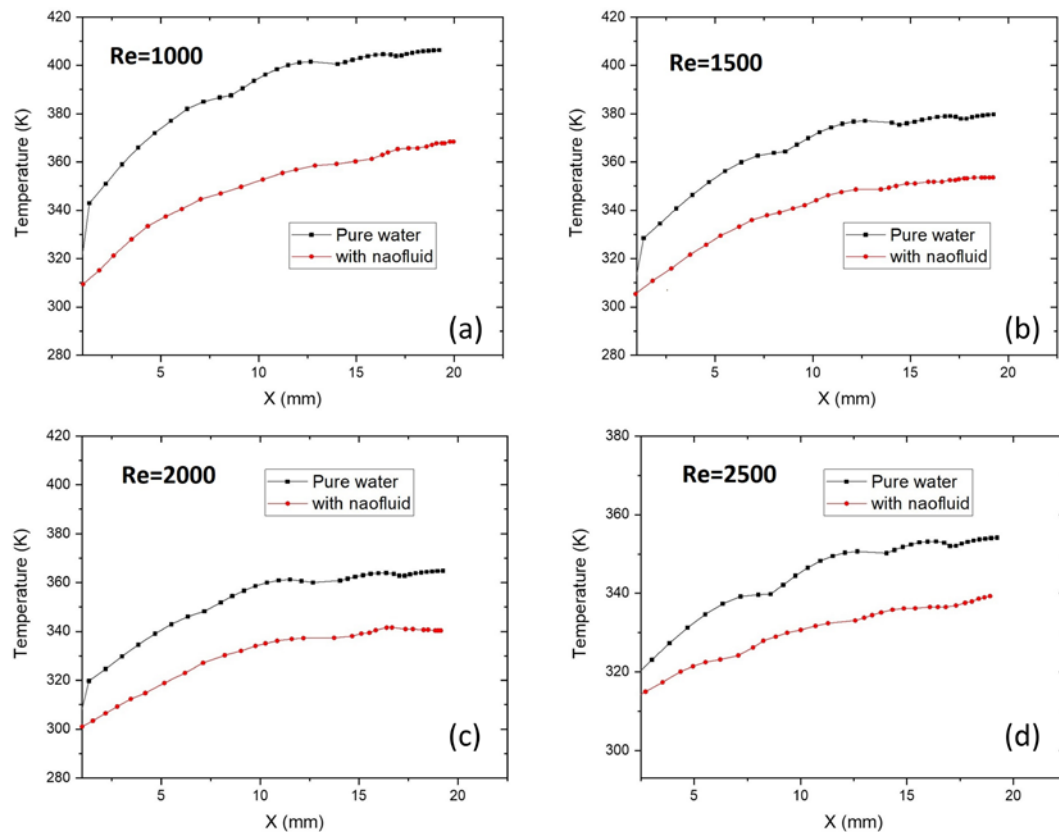


Figure 4.19 Effect on nanofluid on the wall temperature Distribution at different Reynolds number.

### 4.3.3 Effect on Nusselt number

Figure 4.20a shows the average Nu for a water-$Al_2O_3$ nanofluid for various Re values and a given solid volume φ. The volume fractions of the base fluid and solid are represented by the difference in behaviours (Nu number). Comparing the Nu numbers of water and water-$Al_2O_3$ nanofluid reveals that the rate of heat transfer has been significantly influenced using nanofluid because, for the same φ and Re, the average $Nu_{avg}$ in case of nanofluid quadrupled as compared to water.

104

### 4.3.4 Effect on PEC

In the base fluids under study (water), Figure 4.20b depicts the PEC when nanoparticle volume concentration is 4%. The PEC gives the thermal efficiency of FMCHS as it compares the Nu increment to the increment in friction coefficient. With the variation of Reynolds number, Nusselt number as well as friction coefficient changes. Which will ultimately change the PEC. Main factors which is involved in heat transfer augmentation are nanoparticles concentration, fluid velocity, thermal conductivity of base fluid etc. The factors which have been chosen for heat transfer augmentation will change the behaviour of friction coefficient and consequently PEC will vary. In Figure 4.20b, PEC rises with the addition of nanoparticles due the increase in Nu. PEC is doubled when nanofluid is employed as compared to water as base fluid. At Re=2000, PEC is maximum, however when is greater than 2000, PEC decreases as friction coefficient parameter starts dominating.
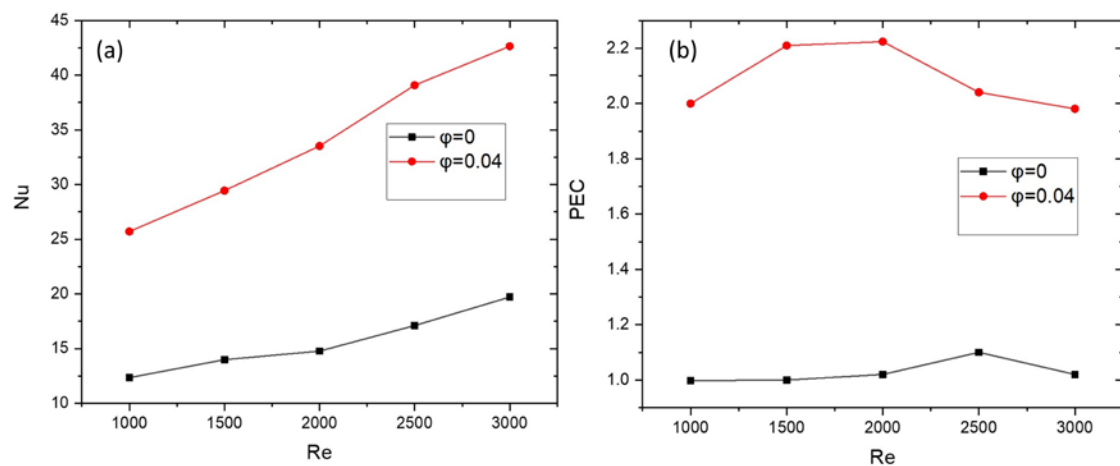


Figure 4.20 Variation Re for pure water and nanoparticle, φ=0.04 with (a) Nu (b) Performance evaluation criteria (PEC)

### 4.3.5 Effect on pressure drop.

The pressure loss grows as the fluid's velocity rises. By reducing the microchannel's diameter, the pressure drop is likewise enhanced. This behaviour is especially pronounced as we move from inlet to the branch closer to the outlet of the channel. The pressure loss is maximised when the Re number increases in relation to the behaviour of the pressure contours in Figure 4.21

### 4.3.6 Velocity and temperature contours

Figure 4.22 shows the static temperature distribution for pure water at various Re values. With the increase in Re, heat dissipation from the wall of the channel has

105

increased and temperature of the channel wall has decreased. At the starting of the FMCHS, heat transfer was highest because of large difference between cold inlet fluid and high temperature channel wall. As the number of fractal branches increases, temperature distribution becomes more uniform in these regions, thus preventing the development of dramatic temperature gradient. Additionally, thermal gradients are removed as the Re number rises, especially at the outlet region.
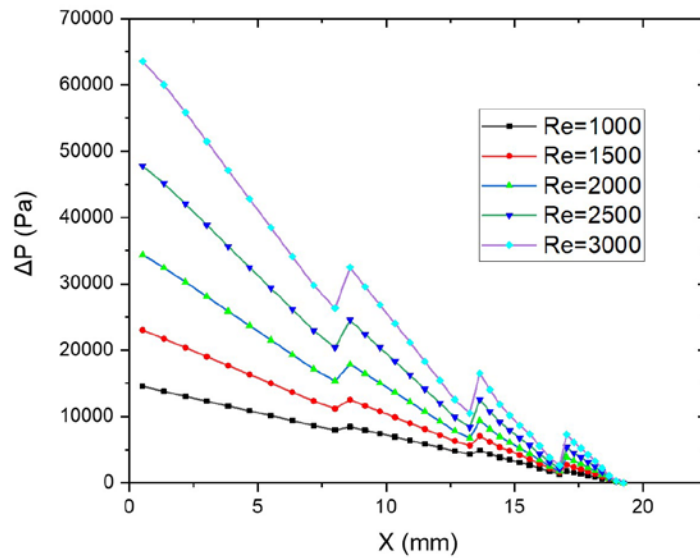


Figure 4.21  Variation of pressure drops along the channel length at different Re.

106
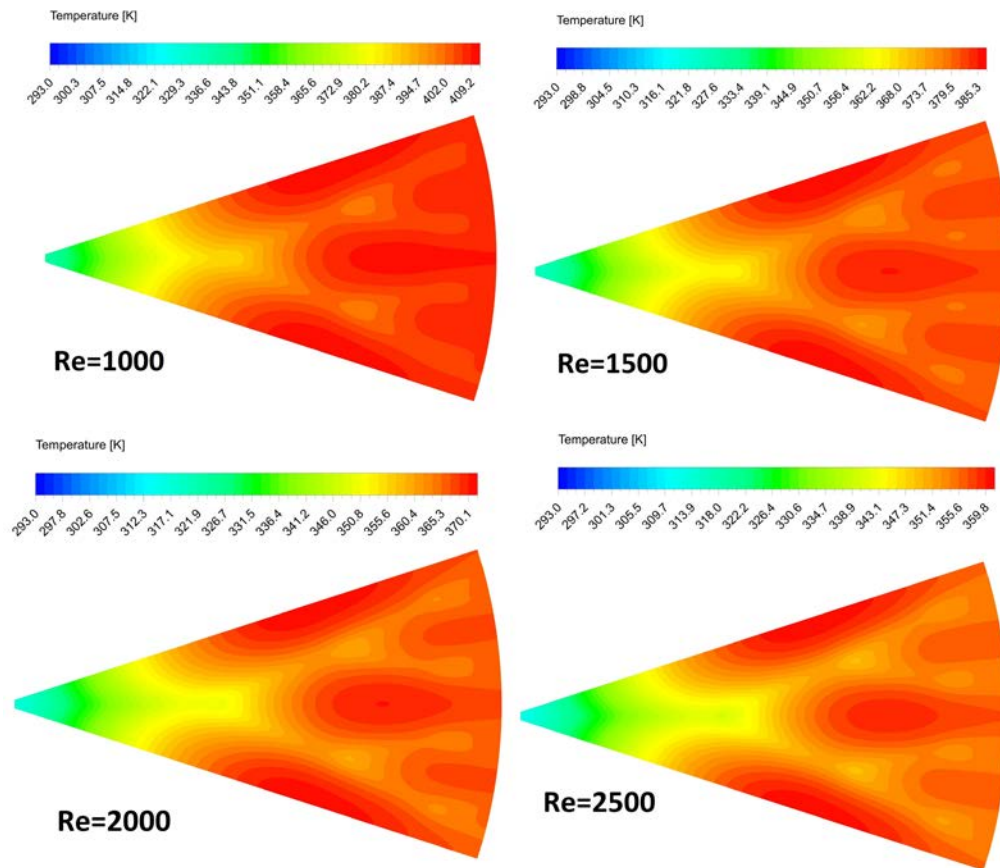
Figure 4.22 Temperature contour of the base of FMCHS at different value of Re.

Hot spots that can be enhanced by using more tree-like structures have been seen in some places without fluid flow pathways. Higher solid volume fraction nanoparticle content will considerably improve the thermophysical characteristics, particularly the cooling fluid's thermal conductivity, which speeds up heat transfer and ensures temperature distribution uniformity. the base fluid's density and viscosity are increased by the addition of the nanoparticles, which results in a larger pressure drop. The main benefit of utilising nanofluid is an increase in transfer of heat, whereas the main drawback is an increase in pressure drop, with the PEC serving as the benchmark for measuring its performance.

Figure 4.23 depicts the contour of the velocity distribution at various Re when pure water is the working flow. As can be seen, the main branch has the highest velocity, while the sub-branch has a divided flow and a decreasing velocity. By reducing velocity, the wall temperature on a branch close to the outlet rose and the rate of heat transfer decreased.

107
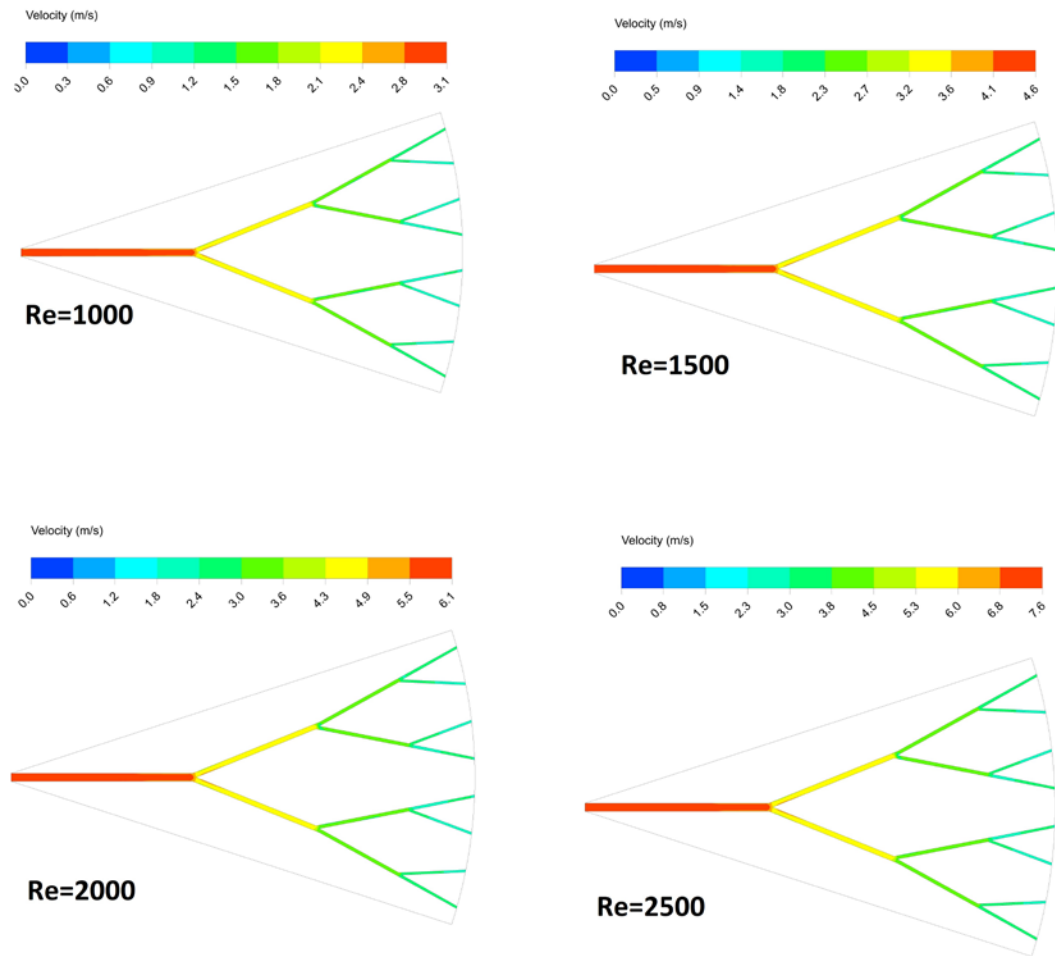
Figure 4.23 Velocity contours for different Reynolds number.

## 4.4    Optimisation results

The dataset was formed using Figure 4.14 and Figure 4.15 to train artificial neural networks (ANNs), which produced a prediction model. The geometrical modification and flow rates were used as input and $\Omega$, R, and, Nu as output variables to arrange and prepare the simulation data for use in the NN. Data was split into three parts for training: 70%, validate 15% and test 15% were utilized for the training process. All input and output variables are treated similarly during training and have an equal influence on the model thanks to this normalization. The data architect with ANN training is displayed in Figure *4.24*. This data aligns with excellent training outcomes for artificial neural networks, as evidenced by the test and validation curves. An artificial neural network was chosen to define the neural network's architecture during formation. One can accomplish this by looking at the training and validation curves. Test data may be used to verify the ANN's accuracy after training the model. The outcomes demonstrated a mean squared error of <2% for the prediction of $\Omega$, <1.5% for the prediction of Nu, and <2% for $R_{th}$ emulated from the simulations result (Figure

108

4.10, Figure 4.11, Figure 4.14, and Figure 4.15) performed using Ansys fluent 2022 R1.

Table 4.1 Optimization and simulation results at the optimal values for FMCHS.

|  | Model (FMCHS-R) | Flow rate (ml/min) | Nu | $\Omega$ (mW) | $R_{th}$ (K-cm$^2$/W) |
|---|---|---|---|---|---|
| Simulation | 26% of the radius of ribs along all the paths | 200 | 18.4869 | 7.2695 | 2.1105 |
| Optimal | 26% of the radius of ribs along all the paths | 200 | 18.1014 | 7.4813 | 2.0736 |

The optimization process is conducted through the utilization of MFO (Multi-Objective Function). Three optimization objectives requiring maximizing (Nu) and minimizing ($\Omega$, $R_{th}$) for varied working fluid flow rates and distinct models were considered. A multi-objective function combined Nu, $1/\Omega$, and $1/R_{th}$ to create the neural network model. This function was picked as the target for optimization to reach the required result. The nature of the problem being addressed from the available data and the needs of the system or application were all considered when choosing this objective function. The proper objective function is first specified, and then the evolutionary algorithm is executed. Iterations and sample size for this method were specified precisely as they substantially impact their performance. The MFO algorithm was used to optimize the multi-objective Functions. It was observed that the Nu, $\Omega$, and $R_{th}$ monotonously increase with flow rates. The number of ribs and grooves enhances the thermohydraulic performance, but it comes at a higher $\Delta P$. While there is a noticeable enhancement in Nu for flow rates in the intermediate range, the accompanying increase in pressure drop is negligible.

Figure 4.24: Regression performance for trained ANN for (a) Thermal Resistance ($R_{th}$), (b) Nusselt number (Nu), and (c) Pumping Power ($\Omega$).

The correlation was found between $Nu_{max}$, $\Omega_{max}$, and $R_{th, max}$. Similarly, the relationship between $Nu_{min}$, $\Omega_{min}$, and $R_{th,min}$ was obtained. The optimized shape corresponds to the anticipated outcomes; with the Model FMCHS-R, the optimized value is 26% of the rib radius of FMCHS-R along all the paths at a 200 ml/min flow rate. Through optimization, errors concerning the predicted value of Nu, $\Omega$, and $R_{th}$ were found to be 2.13%, 2.83%, and 1.78% respectively for the optimized case. These findings are exact, especially in the optimized scenario, where the estimated values of Nu, $\Omega$, and $R_{th}$ are almost the same as the actual values. The inaccuracies related to the maximum and minimum scenarios may be ascribed to the constraints of the multi-variable optimization technique. Optimization and simulation Results for Nu, $\Omega$, and $R_{th}$ are outlined and compared in Table 4.1.

110

### 4.4.1 RSM Modelling

Subsequently, RSM aids in equating how factors and their interactions affect the results. Figure 4.26 illustrates the recursive behaviour of the flow rate and model design variables and how they affected the $R_{th}$, $\Omega$, $\eta$, and Nu. For all model design, the $\eta$ and Nu increases with increasing flow rates, as seen in Figure 4.26. By examining the charts in Figure 4.25, it can be concluded that increasing flow rates in all FMCHS geometrical models results in a drop in $R_{th}$ and that altering the models' geometrical design also aids in achieving the best possible outcome for FMCHS (Table 4.2).

Table 4.2. DOE with responses.

| Model configuration | Flow Rate (mL/min) | Thermal Resistance (K-cm$^2$/W) | Pumping Power (kW) | Efficiency | Nu |
|---|---|---|---|---|---|
| FMCHS-C | 300 | 1.02798 | 55 | 0.916414 | 20.2661 |
| FMCHS-R | 400 | 0.786906 | 422.689 | 0.920341 | 26.7227 |
| FMCHS-P | 200 | 1.55819 | 8.78705 | 0.932767 | 8.28367 |
| FMCHS-P | 300 | 1.17587 | 24.1639 | 0.944616 | 11.6253 |
| FMCHS-R | 300 | 0.979932 | 178.5 | 0.957962 | 22.9118 |
| FMCHS-P | 300 | 1.17587 | 24.1639 | 0.944616 | 11.6253 |
| FMCHS-P | 300 | 1.17587 | 24.1639 | 0.944616 | 11.6253 |
| FMCHS-R | 200 | 1.25447 | 65.5865 | 0.919479 | 19.5731 |
| FMCHS-C | 400 | 0.840837 | 113.156 | 0.887001 | 23.0242 |
| FMCHS-C | 200 | 1.28087 | 22.9786 | 0.900985 | 17.8652 |
| FMCHS-P | 400 | 0.949899 | 42.3773 | 0.88316 | 13.5799 |
| FMCHS-P | 300 | 1.17587 | 24.1639 | 0.944616 | 11.6253 |
| FMCHS-P | 300 | 1.17587 | 24.1639 | 0.944616 | 11.6253 |

The ANOVA model (Table 4.3) for the output parameter is statistically significant, with P-values less than 0.05 for both the model and the current inputs. All output responses had high $R^2$ and adjusted $R^2$ values, indicating that the model provides data

111

that is very similar to the experimental data. The adj. $R^2$ values were less than 2% for all replies, showing high prediction reliability. The lack of fit is insignificant as the P value is more prominent than 0.05.

Table 4.3 ANOVA F-value and p-value for Rth, $\Omega$, $\eta$ and Nu.

| Source | Thermal Resistance ($R_{th}$) | | Pumping Power($\Omega$) | | Efficiency ($\eta$) | | Nu | |
|---|---|---|---|---|---|---|---|---|
| | F-value | p-value | F-value | p-value | F-value | p-value | F-value | p-value |
| Model | 74.67 | < 0.0001 | 14.09 | 0.0015 | 11.97 | 0.0025 | 705.72 | < 0.0001 |
| A-Groove | 2.10 | 0.1906 | 18.92 | 0.0034 | 13.98 | 0.0073 | 93.83 | < 0.0001 |
| B-Flow rate | 292.82 | < 0.0001 | 19.33 | 0.0032 | 6.31 | 0.0403 | 448.51 | < 0.0001 |
| AB | 0.1448 | 0.7148 | 8.94 | 0.0202 | 0.5302 | 0.4901 | 8.60 | 0.0219 |
| $A^2$ | 77.75 | < 0.0001 | 17.04 | 0.0044 | 0.4984 | 0.5030 | 2593.06 | < 0.0001 |
| $B^2$ | 7.15 | 0.0318 | | | 29.92 | 0.0009 | 1.60 | 0.2458 |
| Std. Dev. | 0.0362 | | 44.65 | | 0.0102 | | 0.3394 | |
| Mean | 1.12 | | 79.22 | | 0.9262 | | 16.18 | |
| C.V % | 3.23% | | 56.36 | | 1.10 | | 2.10 | |
| $R^2$ | 0.9816 | | 0.9096 | | 0.8953 | | 0.9980 | |
| Adjusted $R^2$ | 0.9685 | | 0.8451 | | 0.8205 | | 0.9966 | |
| Adequate Precision | 29.5265 | | 13.7545 | | 11.3848 | | 78.5345 | |
| Lack of Fit | 0.0031 | | 0.003 | | 0.0002 | | 0.005 | |

112
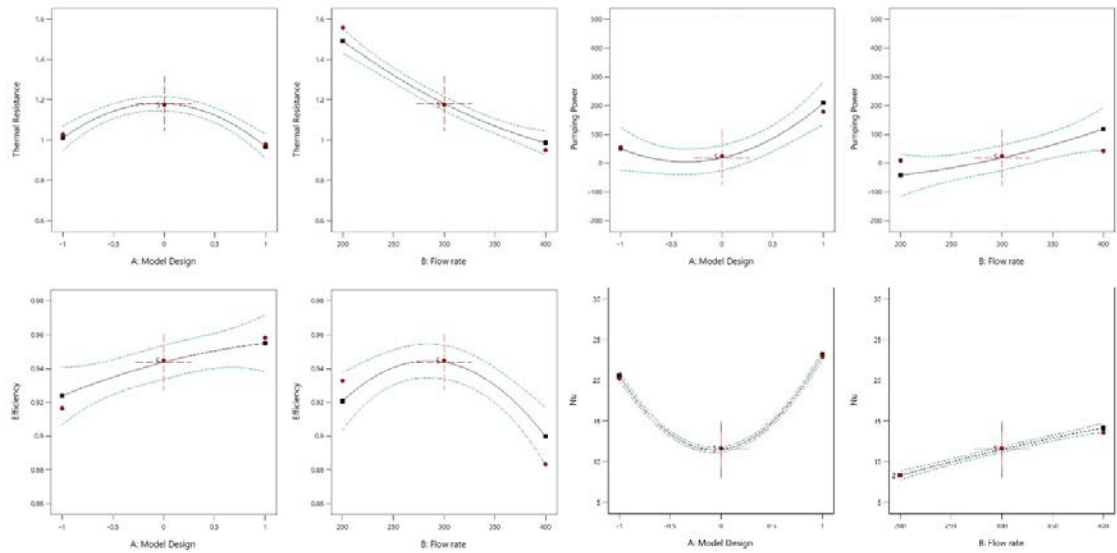
Figure 4.25 All factor desirability of RSM.
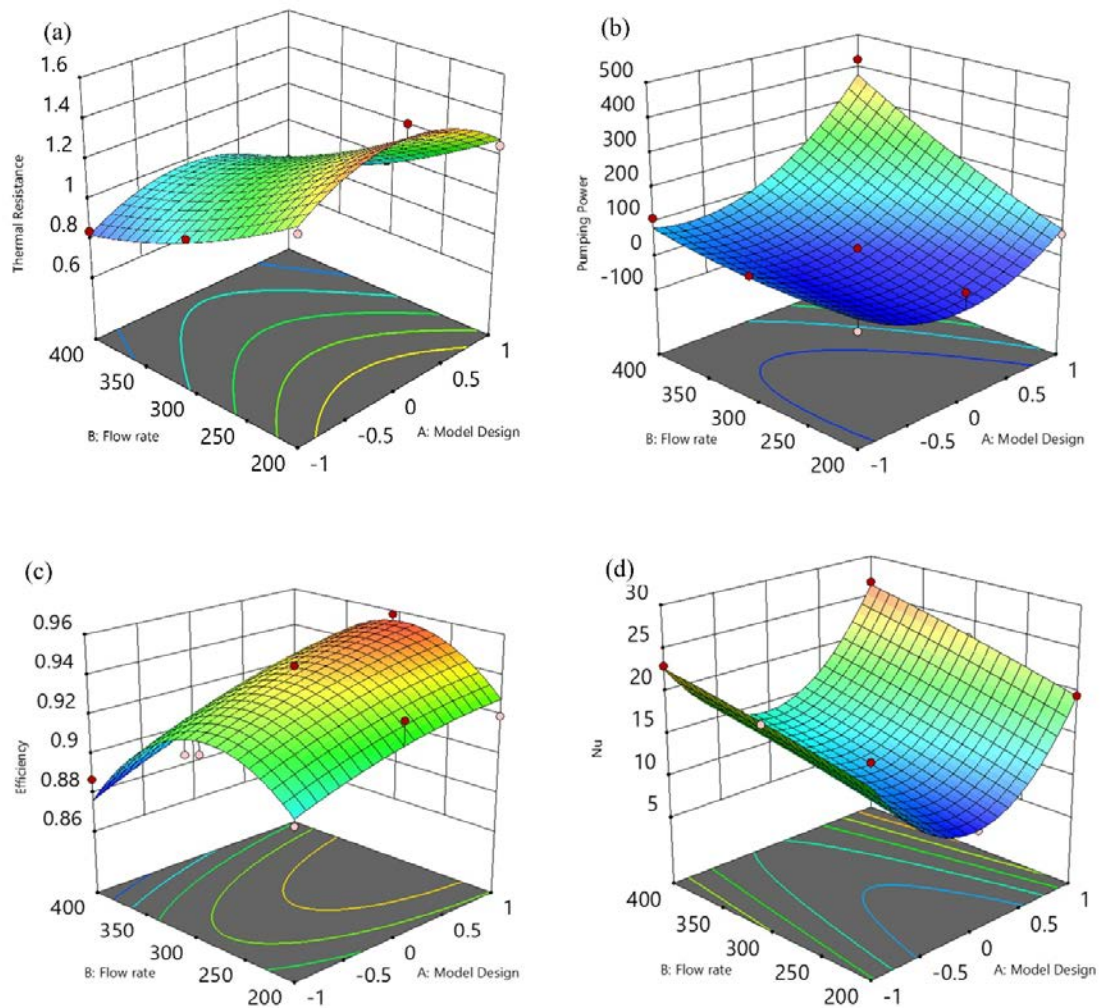


Figure 4.26 Surface response for Model Design and Flow rates a) $R_{th}$ b) $\Omega$ c) $\eta$, and (d) Nu.

113

Re-alterations have been significantly more effective than other variables in minimising the $R_{th}$ and $\Omega$.

## 4.4.2 Artificial Neural Network (ANN)
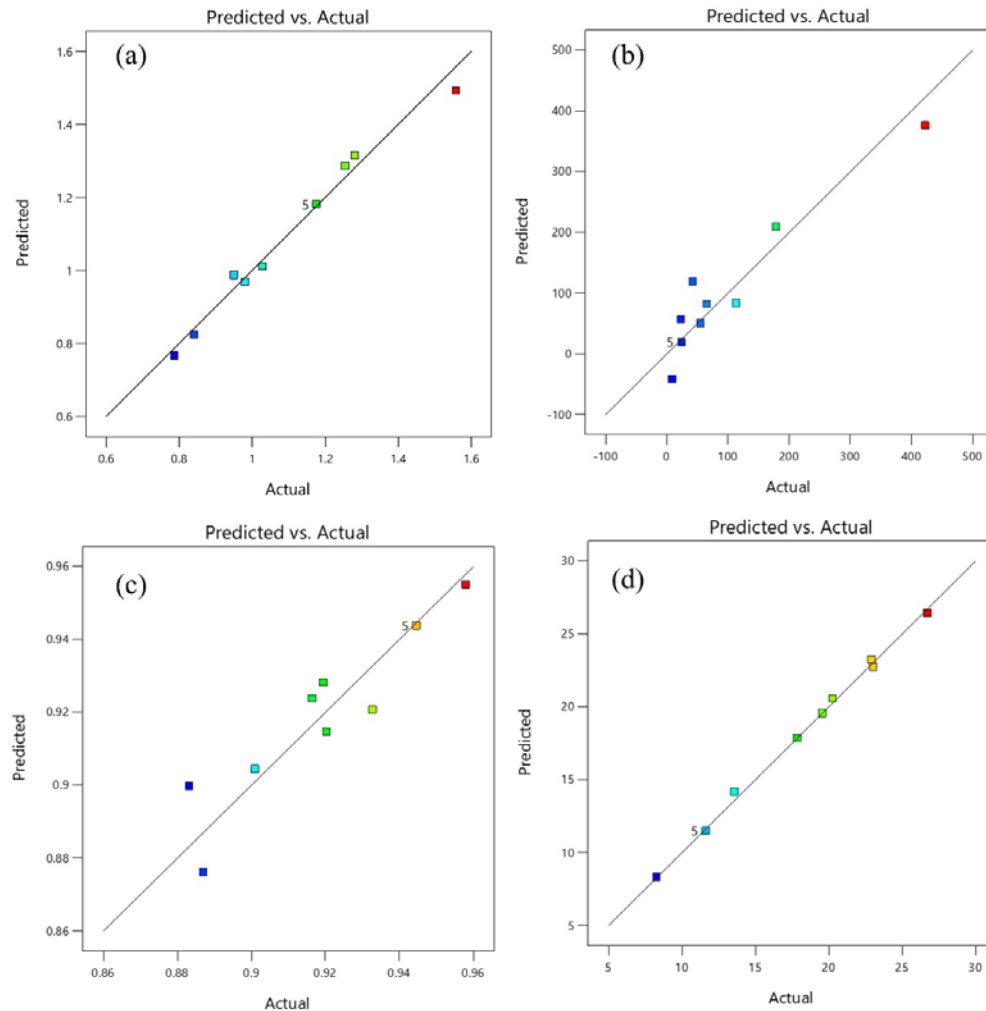


Figure 4.27: Goodness fit curve (a) Rth  (b) $\Omega$ (c) $\eta$, and (d) Nu.

The linear fitting is displayed in Figure *4.27* with $R^2$ values for Rth, $\Omega$, $\eta$, and Nu are 0.9816, 0.9096, 0.8953, and 0.9980 respectively. The relationship between observed and expected data is displayed on linear fit graphs. In our instance, the HHO response surface provides the anticipated data, while simulations provide the observed values. Our observation sets' closeness to this line suggests that we can reply to areas with good precision.

## 4.4.3 HHO modelling

Through the utilization of HHO (Multi-Objective Function), the optimization process is conducted. Three optimization scenarios requiring maximizing ($\eta$, Nu) and

114

minimizing ($\Omega$, $R_{th}$) for varied working fluid flow rates and distinct models were taken into consideration. A multi-objective function was formed combining, Nu, $\eta$, $1/\Omega$ and $1/R_{th}$ to create the neural network model. To reach the required result, this function was picked as the target for optimization. The nature of the problem being addressed from the available data, and the needs of the system or application were all taken into consideration when choosing this objective function. The proper objective function is first specified, and then the evolutionary algorithm is executed. Iterations and sample size for this method was specified precisely as they have a substantial impact on their performance. HHO algorithm was used to optimize multi-objective Function. It was observed that the Nu, $\eta$, $\Omega$ and $R_{th}$ monotonously increases with flow rates. With the number of ribs and grooves enhances the thermohydraulic performance; but it comes at higher $\Delta P$. While there is a noticeable enhancement in Nu for flow rates in the intermediate range, the accompanying increase in pressure drop is negligible.
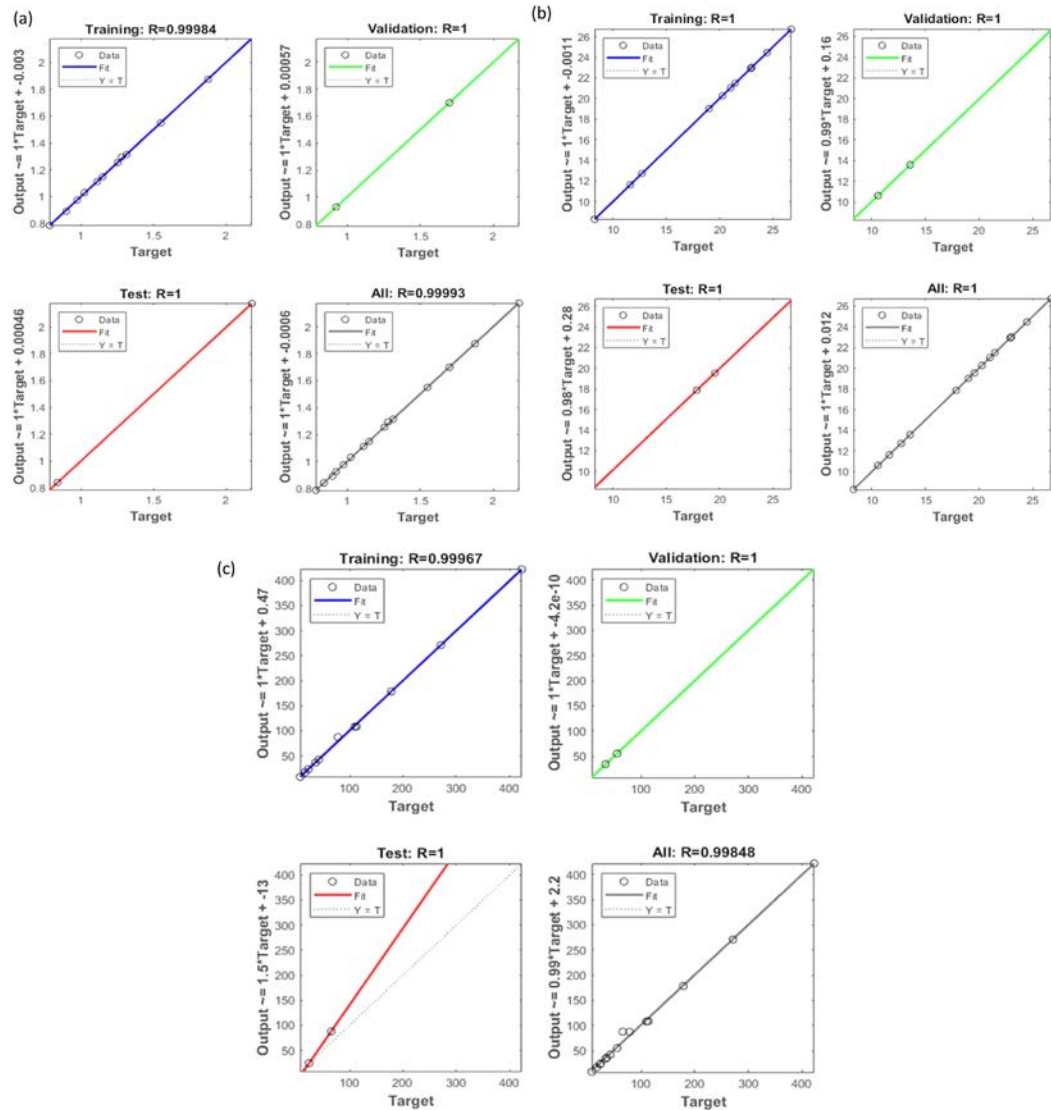
The correlation between $Nu_{max}$ and $\eta_{max}$, $\Omega_{max}$, and $R_{th,max}$ was found. Similarly, the relationship between $Nu_{min}$, $\eta_{min}$, $\Omega_{min}$, and $R_{th,min}$ was obtained. The optimized shape corresponds to the anticipated outcomes, with the Model FMCHS-R, the optimized value is 64.5% of rib radius of FMCHS-R along all the path at a flow rate of 400 ml/mint. Error with respect to the predicted value of $\eta$, Nu, $\Omega$, $R_{th}$, through optimisation were found to be 0.46%, 1.56%, and 1.73%, and 0.85% resp., for the optimized case. These findings are exceptionally precise, especially in the optimized scenario, where the estimated values of $\eta$, Nu, $\Omega$, and $R_{th}$ are almost same as the actual values.

Table 4.4 Optimization and simulation results at the optimal values for FMCHS.

|  | Model (FMCHS-R) | Flow rate (ml/min) | Nu | $\eta$ | $\Omega$ (mW) | $R_{th}$ (K-cm$^2$/W)) |
|---|---|---|---|---|---|---|
| Simulation | 64.5% of the radius of ribs along all the paths | 400 | 21.27 | 0.879 | 373.95 | 0.767 |
| Optimal | 64.5% of the radius of ribs along all the paths | 400 | 21.6075 | 0.8836 | 367.60 | 0.7609 |

The inaccuracies related to the maximum and minimum scenarios may be ascribed to the constraints of the multi-variable optimization technique employed. Optimization and simulation Results for $\eta$, Nu, $\Omega$, and $R_{th}$ is outlined and compared in Table 4.1.

115
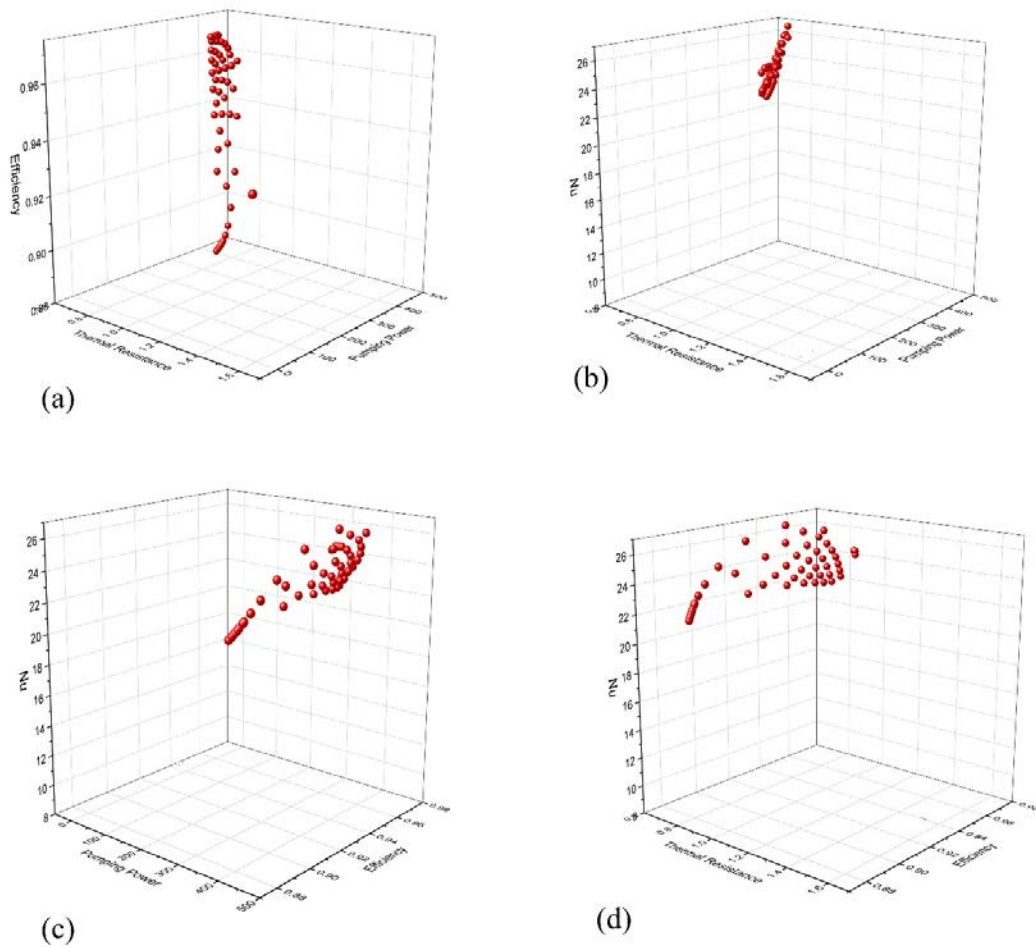
Figure 4.28: Pareto optimal front (a) $\Omega$, $R_{th}$, $\eta$  (b) $\Omega$, $R_{th}$,Nu (c) $\eta$, $\Omega$, Nu (d) $\eta$, $R_{th}$, Nu.

Table 4.5 Comparison of RSM and HHO Optimality.

|  | Model Design | Flow rate (ml/min) | Thermal Resistance (K-cm$^2$/W) | Pumping Work (mW) | Efficiency | Nu |
|---|---|---|---|---|---|---|
| RSM | 1 | 295 | 0.983 | 201.112 | 0.955 | 23.053 |
| HHO | 0.645 | 400 | 0.7609 | 376 | 0.8835 | 21.59 |

The HHO optimization process involves five phases: Initial Population, Fitness function, Selection, Crossover, and Mutation. The HHO is responsible for evaluating and choosing the solution based on the objective function derived from the ANN. Table 4.4 compares the best results from simulation and optimization for the variables. Table 4.5 Compares the results of RSM and HHO. Figure 4.28 discusses the variation between the target objectives ($R_{th}$, $\Omega$,$\eta$, and  Nu).

116

# Chapter 5 CONCLUSIONS, FUTURE SCOPE

# AND SOCIAL IMPACT

## 5.1      Conclusions

### 5.1.1      Numerical study of conventional MCHS

On the thermohydraulic performance of novel ribbed microchannel designs with filleted corners, a CFD investigation is done. MCHS with square ribs (MC-SQ), MCHS with square ribs and fillets at the corners (MC-SQ-FR), and MCHS with square ribs and double fillets at the corners (MC-SQ-DFR) are among the configurations that were studied. This paper's primary conclusions can be summed up as follows:

i.    Relating the benefits of using both ribs and corners with fillets results in notable improvements in the performance of the microchannel.

ii.   It has been demonstrated that filleted ribs have a greater effect on improving overall performance. Fillet ribs can lower the temperature at the bottom of MCHS by reducing the impact of the stagnation zone and rerouting the flow towards channel walls.

iii.  corners with fillets in ribbed MCHS somewhat enhance pressure drops, and a significant enhancement in heat transfer is anticipated. Nu increases by 15–22% when MC–SQ–FR setups are used. Compared to MC-SQ arrangement, the pressure drop rises by 2-10%.

iv.  When compared to the MC-SQ configuration, filled ribs in MC-SQ-FR topologies enhance the Nusselt number by 1–10%.

### 5.1.2   Numerical study of Fractal microchannel heat sink

In this research, a fractal-shaped microchannel heat sink (FMCHS) with ribs and a cavity is designed. A 3-D numerical model is employed to examine the thermohydraulic performance of FMCHS for the flow rate of 200-400 ml/min. Numerical results are validated with the experimental findings and show good agreement. Furthermore, different parameters, such as pressure drop, Nu, base temperature, PEC, etc., are analyzed. The MFO algorithm finds the optimum value of output parameters $\Omega$, Nu, and $R_{th}$. Based on the present study, the following conclusions are drawn:

117

i. FMCHS-C and FMCHS-DC favour the generation of secondary flows, and FMCHS-R and FMCHS-DR favour the high velocity in the channel flow path, which promotes recirculation leading to the redevelopment of the boundary layer, which ultimately improves heat transfer.

ii. FMCHS geometry led to fluid going from the main channel to the branching channel forming a stagnation zone near the outer sidewalls, hampering the heat transfer. In contrast, it promotes heat transfer at the inner sidewalls.

iii. FMCHS-R and FMCHS-DR have the highest heat transfer efficiency and maintain uniform temperatures at the cost of very high-pressure drops.

iv. At lower flow rates, FMCHS-R has PEC<1, indicating that it has comprehensive performance worse than FMCHS-P. However, FMCHS-DR shows PEC>1 for all flow rate ranges, so it has the best performance overall. FMCHS-C and FMCHS-DC have better PEC than their ribbed counterparts.

v. At low pumping power, FMCHS-C and FMCHS-DC are recommended, whereas at high pumping power ($\Omega$>300 mW), FMCHS-R is recommended. For an intermediate range of Pumping power, FMCHS-DR is recommended.

vi. Further, the simulation data is used to test and train a neural network, which predicted $\Omega$, Nu, and Rth with greater than 98% accuracy.

### 5.1.3 Optimization of FMCHS

A global optimization strategy using model types and flow rates was used to find the ideal model. The output variable predicted by MFO and the result from the simulation revealed a small error (less than 3%). With the MFO algorithm, the optimal input value is 26% of the ribs radius along all the paths of FMCHS with ribs (FMCHS-R) at the flow rate of 200 ml/min. With this, the optimum rib radius for path k=0 is 0.02158 mm, and for path k=3, it is 0.0065 mm.

A thermal performance-thermal efficiency trade-off was shown for the fractal microchannel heat sink (FMCHS) with ribs and cavities using RSM and HHO optimisation. RSM chose an FMCHS with ribs (model value 1) and 295 ml/min moderate flow. Thermal resistance was 0.983, pumping work 201.112 mW, high efficiency 0.955, and Nusselt number 23.053. In contrast, HHO chose a 400 ml/min rib-dominant hybrid design (model value 0.645). This design reduced thermal resistance to 0.7609 K-cm$^2$/W, improving cooling, but it also increased pumping work

118

(376 mW) and decreased efficiency (0.8835). Nusselt number was marginally lower at 21.59.

### 5.1.4 Effects of nanofluid on the performance of FMCHS

The current computational study uses water and a water-$Al_2O_3$ nanofluid at a $\varphi=0.04$ solid volume fraction to assess the thermohydraulic performance of a fractal microchannel heat sink (FMCHS). Simulations with Reynolds numbers between 1000 and 3000 show that using nanofluids improves thermal performance. Higher Reynolds numbers lead to lower wall temperatures because of improved convective effects, but the fluid temperature rises throughout the channel length, decreasing heat transfer close to the outlet. Although there is a greater pressure drop, the addition of $Al_2O_3$ nanoparticles results in a notable drop in temperature and enhanced heat transfer. Overall, the performance evaluation criterion (PEC) is improved by the addition of nanoparticles, suggesting that the FMCHS performs better thermally.

## 5.2      Future Scope

As MEMS and electronic devices have evolved so quickly, heat management has always been a    significant concern. As a result, the following investigations should be pursued in the future:

i.   Optimizations of the different wavy designs could be carried out in FMCHS to find their optimal geometry and improve heat transfer performance.

ii.  There is future scope for incorporating magnetohydrodynamic and electrohydrodynamic effects into the secondary flow channels.

iii. The majority of fractal channels design approaches are based on scaling laws; hence, further research is needed to investigate other methods.

iv.  The feasibility of fabricating a heat sink is still questionable; microfeatures smaller than 100 µm are still difficult to fabricate using conventional methods [53]. Because of the limitations and complexity of MCHS production, the distinct and complicated structures of MCHS cannot be realised. So, the development of a suitable fabrication method remains a future challenge for engineers.

v.   It is necessary to handle effective system integration, such as micropump on ICs and direct heat sink integration on chips. This may address the thermal management of hotspots.

119

vi. Effective cooling of hotspots, which are randomly present in ICs and microelectronic devices, still remains a major challenge, as there is no effective method available for the cooling of hotspots.

vii. Hybrid cooling schemes, which combine the benefits of microchannel with those of other cooling schemes such as spray cooling, jet impingement, etc., can be a very effective way to achieve cooling performance. Moreover, active and passive cooling techniques can also be combined for further heat transfer augmentation.

viii. One of the most promising fluids for improving the thermal performance of micro heat sinks is nanofluids. As a result, enhancing the stability of nanoparticle dispersion in the base fluid is a promising research area.

ix. Dispersion and random motion of particles, clustering, and other factors should all be considered while developing a flow model for nanofluids flow and thermal properties in micro heat sinks.

x. In future research, other nanofluids with different volume fractions can be examined in the study of Double layered MCHS, as well as the effect of magnetic and electric fields on the cooling performance of the Double layered MCHS.

## 5.3    Social  Impact

### i.   Energy Efficiency and Sustainability

- MCHS and FMCHS improve electronics thermal management, decreasing the requirement for bulky, power-consuming cooling systems.

- FMCHS improves the thermal performance of renewable energy devices like solar inverters and battery systems, boosting cleaner energy.

- Power consumption decreases with efficient cooling, minimising greenhouse gas emissions.

### ii.  Healthcare and Biomedical Applications

- Advanced Medical Device Cooling: MRI machines, lasers, and diagnostic systems need efficient cooling to work and stay safe.

120

- Lab-on-a-Chip Systems: Point-of-care devices use microchannel cooling to improve quick diagnoses in underserved areas.

### iii. Industrial and Technological Advancement

- FMCHS enable compact cooling in microelectronic devices, aiding IoT, wearable tech, and healthcare device miniaturisation.

- Aerospace electronics, electric cars, and power electronics last longer with good heat dissipation.

- Increases HPC: Allows denser processor packaging and more powerful computers for science, AI, and space exploration.

### iv. Economic and Social Development

- Encourages Technological Innovation: Helps startups and companies create next-gen electronics and bio-device cooling.

- More microfabrication, nanotechnology, and thermal management engineers needed in high-tech sectors.

- Efficiency for Consumers: Longer device life and energy savings lower electronics ownership costs.

### v. Education and Research Impact

- Encourages interdisciplinary fluid dynamics, heat transport, MEMS, and fractal geometry instruction.

- Inspires STEM Research: Fractal microchannel structures in thermofluidic inspire young engineers and scientists.

### vi. Resource Optimization and Environmental Management

- Minimal Material Waste: FMCHS optimise channel designs to reduce material and machining stages.

- Water Conservation: FMCHS increase thermal performance in liquid-cooled systems with reduced coolant volume, which is important in resource-scarce settings.

121

# REFERENCES

[1] A. Bar-Cohen, P. Wang, Thermal management of on-chip hot spot, J. Heat Transfer. 134 (2012) 1–15. https://doi.org/10.1115/1.4005708.

[2] I. Mudawar, D. Bharathan, K. Kelly, S. Narumanchi, Two-phase spray cooling of hybrid vehicle electronics, IEEE Trans. Components Packag. Technol. 32 (2009) 501–512. https://doi.org/10.1109/TCAPT.2008.2006907.

[3] EXECUTIVE SUMMARY, INTERNATIONAL ROADMAP FOR DEVICES AND SYSTEMS 2021UPDATE, 2021. https://irds.ieee.org/images/files/pdf/2021/2021IRDS_ES.pdf (accessed May 2, 2022).

[4] M.A. Ebadian, C.X. Lin, A review of high-heat-flux heat removal technologies, J. Heat Transfer. 133 (2011). https://doi.org/10.1115/1.4004340.

[5] G.E. MOORE, Cramming More Components onto Integrated Circuits, Proc. IEEE. 86 (1998) 399–415. https://doi.org/10.1111/j.1467-9469.2011.00765.x.

[6] D. Burgid, J.H. Ausubelid, Moore's Law revisited through Intel chip density, (2021). https://doi.org/10.1371/journal.pone.0256245.

[7] X. Luo, Y. Liu, W. Liu, A honeycomb microchannel cooling system for microelectronics cooling, in: Heat Transf. Eng., 2011: pp. 616–623. https://doi.org/10.1080/01457632.2010.509755.

[8] J.R. Black, Electromigration—A Brief Survey and Some Recent Results, IEEE Trans. Electron Devices. 16 (1969) 338–347. https://doi.org/10.1109/T-ED.1969.16754.

[9] Thermal Management Technologies Market Size Report, 2024, (n.d.). https://www.grandviewresearch.com/industry-analysis/thermal-management-technologies-industry (accessed April 3, 2022).

122

[10]   Z. Khattak, H.M. Ali, Air cooled heat sink geometries subjected to forced flow: A critical review, Int. J. Heat Mass Transf. 130 (2019) 141–161. https://doi.org/10.1016/j.ijheatmasstransfer.2018.08.048.

[11]   J.L. Smoyer, P.M. Norris, Brief Historical Perspective in Thermal Management and the Shift Toward Management at the Nanoscale, Heat Transf. Eng. 40 (2019) 269–282. https://doi.org/10.1080/01457632.2018.1426265.

[12]   B. Agostini, M. Fabbri, J.E. Park, L. Wojtan, J.R. Thome, B. Michel, State of the art of high heat flux cooling technologies, Heat Transf. Eng. 28 (2007) 258–281. https://doi.org/10.1080/01457630601117799.

[13]   T.G. Karayiannis, M.M. Mahmoud, Flow boiling in microchannels: Fundamentals and applications, Appl. Therm. Eng. 115 (2017) 1372–1397. https://doi.org/10.1016/J.APPLTHERMALENG.2016.08.063.

[14]   A. Abdoli, G. Jimenez, G.S. Dulikravich, Thermo-fluid analysis of micro pin-fin array cooling configurations for high heat fluxes with a hot spot, Int. J. Therm.            Sci.            90            (2015)            290–297. https://doi.org/10.1016/j.ijthermalsci.2014.12.021.

[15]   S. Feng, Y. Yan, H. Li, L. Zhang, S. Yang, Thermal management of 3D chip with non-uniform hotspots by integrated gradient distribution annular-cavity micro-pin    fins,    Appl.    Therm.    Eng.    182    (2021)    116132. https://doi.org/10.1016/J.APPLTHERMALENG.2020.116132.

[16]   K.P. Drummond, D. Back, M.D. Sinanis, D.B. Janes, D. Peroulis, J.A. Weibel, S. V. Garimella, Characterization of hierarchical manifold microchannel heat sink arrays under simultaneous background and hotspot heating conditions, Int. J.    Heat    Mass    Transf.    126    (2018)    1289–1301. https://doi.org/10.1016/j.ijheatmasstransfer.2018.05.127.

123

[17]  I. Mudawar, Assessment of High-Heat-Flux Thermal Management Schemes, 2001.

[18]  T.A. Shedd, Next generation spray cooling: High heat flux management in compact spaces, Heat Transf. Eng. 28 (2007) 87–92. https://doi.org/10.1080/01457630601023245.

[19]  I. Mudawar, Two-phase microchannel heat sinks: Theory, applications, and limitations, J. Electron. Packag. Trans. ASME. 133 (2011). https://doi.org/10.1115/1.4005300.

[20]  T.C. Hung, Y.X. Huang, W.M. Yan, Thermal performance analysis of porous-microchannel heat sinks with different configuration designs, Int. J. Heat Mass Transf. 66 (2013) 235–243. https://doi.org/10.1016/j.ijheatmasstransfer.2013.07.019.

[21]  Z. Soleymani, M. Rahimi, M. Gorzin, Y. Pahamli, Performance analysis of hotspot using geometrical and operational parameters of a microchannel pin-fin hybrid heat sink, Int. J. Heat Mass Transf. 159 (2020) 120141. https://doi.org/10.1016/j.ijheatmasstransfer.2020.120141.

[22]  G. V. Kewalramani, G. Hedau, S.K. Saha, A. Agrawal, Empirical correlation of laminar forced convective flow in trapezoidal microchannel based on experimental and 3D numerical study, Int. J. Therm. Sci. 142 (2019) 422–433. https://doi.org/10.1016/j.ijthermalsci.2019.05.001.

[23]  S. V. Garimella, V. Singhal, D. Liu, On-chip thermal management with microchannel heat sinks and integrated micropumps, Proc. IEEE. 94 (2006) 1534–1548. https://doi.org/10.1109/JPROC.2006.879801.

[24]  J. Kim, Spray cooling heat transfer: The state of the art, Int. J. Heat Fluid Flow. 28 (2007) 753–767.

124

https://doi.org/10.1016/J.IJHEATFLUIDFLOW.2006.09.003.

[25]  B. Basinger, G. Aguilar, J.S. Nelson, Effect of Skin Indentation on Heat Transfer during Cryogen Spray Cooling, Lasers Surg. Med. 34 (2004) 155–163. https://doi.org/10.1002/lsm.20011.

[26]  X. Wei, Y. Joshi, M.K. Patterson, Experimental and numerical study of a stacked microchannel heat sink for liquid cooling of microelectronic devices, J. Heat Transfer. 129 (2007) 1432–1444. https://doi.org/10.1115/1.2754781.

[27]  C. Zhang, Z. Tang, Z. Zhang, J. Shi, J. Chen, M. Zhang, Impact of airside fouling on microchannel heat exchangers, Appl. Therm. Eng. 128 (2018) 42–50. https://doi.org/10.1016/j.applthermaleng.2017.08.163.

[28]  B. Xu, Y. Wang, J. Chen, F. Li, D. Li, X. Pan, Investigation of domestic air conditioner with a novel low charge microchannel condenser suitable for hydrocarbon refrigerant, Measurement. 90 (2016) 338–348. https://doi.org/10.1016/J.MEASUREMENT.2016.04.034.

[29]  J. Shi, X. Qu, Z. Qi, J. Chen, Investigating performance of microchannel evaporators with different manifold structures, Int. J. Refrig. 34 (2011) 292–302. https://doi.org/10.1016/j.ijrefrig.2010.08.008.

[30]  J.J.L. Lee, B.S. Haynes, Process intensification writ large with microchannel absorption in nitric acid production, Chem. Eng. Sci. 169 (2017) 140–150. https://doi.org/10.1016/J.CES.2017.01.015.

[31]  S.A. Khashan, S. Dagher, A. Alazzam, B. Mathew, A. Hilal-Alnaqbi, Microdevice for continuous flow magnetic separation for bioengineering applications, J. Micromechanics Microengineering. 27 (2017) 055016. https://doi.org/10.1088/1361-6439/AA666D.

[32]  S. Jakhar, M.S. Soni, N. Gakkhar, Historical and recent development of

concentrating photovoltaic cooling technologies, Renew. Sustain. Energy Rev. 60 (2016) 41–59. https://doi.org/10.1016/j.rser.2016.01.083.

[33]   A.E.M. Mora, A.L.F. de Lima e Silva, S.M.M. de Lima e Silva, Numerical study of the dynamics of a droplet in a T-junction microchannel using OpenFOAM, Chem. Eng. Sci. 196 (2019) 514–526. https://doi.org/10.1016/j.ces.2018.11.020.

[34]   T. Stevens, M. Baelmans, Optimal pressure drop ratio for micro recuperators in small sized gas turbines, Appl. Therm. Eng. 28 (2008) 2353–2359. https://doi.org/10.1016/J.APPLTHERMALENG.2008.01.018.

[35]   V.T. Karathanos, N.K. Kanellopoulos, V.G. Belessiotis, Development of porous structure during air drying of agricultural plant products, J. Food Eng. 29 (1996) 167–183. https://doi.org/10.1016/0260-8774(95)00058-5.

[36]   A. Vittoriosi, J.J. Brandner, P. Ruther, O. Paul, R. Dittmeyer, Design and Characterization of Integrated Microsensors for Heat Transfer Studies in Microchannels, Http://Dx.Doi.Org/10.1080/08916152.2013.849465. 27 (2014) 389–402. https://doi.org/10.1080/08916152.2013.849465.

[37]   A.M. Hayes, J.A. Khan, A.H. Shaaban, I.G. Spearing, The thermal modeling of a matrix heat exchanger using a porous medium and the thermal non-equilibrium model, Int. J. Therm. Sci. 47 (2008) 1306–1315. https://doi.org/10.1016/J.IJTHERMALSCI.2007.11.005.

[38]   K.S. Udell, Heat transfer in porous media considering phase change and capillarity—the heat pipe effect, Int. J. Heat Mass Transf. 28 (1985) 485–495. https://doi.org/10.1016/0017-9310(85)90082-1.

[39]   R. Greenkorn, Flow phenomena in porous media: fundamentals and applications in petroleum, water and food production, (1983).

126

https://www.osti.gov/biblio/6291726 (accessed July 19, 2021).

[40] K. Vafai, Preface: Porous media and its applications in science, engineering, and industry, AIP Conf. Proc. 1453 (2011) 1–7. https://doi.org/10.1063/1.4711145.

[41] O.A. Akbari, D. Toghraie, A. Karimipour, Impact of ribs on flow parameters and laminar heat transfer of water-aluminum oxide nanofluid with different nanoparticle volume fractions in a three-dimensional rectangular microchannel, Adv. Mech. Eng. 7 (2015) 1–11. https://doi.org/10.1177/1687814015618155.

[42] B. Kwon, T. Foulkes, T. Yang, N. Miljkovic, W.P. King, Air Jet Impingement Cooling of Electronic Devices Using Additively Manufactured Nozzles, IEEE Trans. Components, Packag. Manuf. Technol. 10 (2020) 220–229. https://doi.org/10.1109/TCPMT.2019.2936852.

[43] D.B. Tuckerman, R.F.W. Pease, High-Performance Heat Sinking for VLSI, IEEE Electron Device Lett. EDL-2 (1981) 126–129. https://doi.org/10.1109/EDL.1981.25367.

[44] N. Gilmore, V. Timchenko, C. Menictas, Microchannel cooling of concentrator photovoltaics: A review, Renew. Sustain. Energy Rev. 90 (2018) 1041–1059. https://doi.org/10.1016/j.rser.2018.04.010.

[45] G. Kumaraguruparan, R.M. Kumaran, T. Sornakumar, T. Sundararajan, A numerical and experimental investigation of flow maldistribution in a micro-channel heat sink, Int. Commun. Heat Mass Transf. 38 (2011) 1349–1353. https://doi.org/10.1016/J.ICHEATMASSTRANSFER.2011.08.020.

[46] M. Zunaid, A. Jindal, D. Gakhar, A. Sinha, NUMERICAL STUDY OF PRESSURE DROP AND HEAT TRANSFER IN A STRAIGHT

127

RECTANGULAR AND SEMI CYLINDRICAL PROJECTIONS MICROCHANNEL HEAT SINK, Yildiz Technical University Press, 2017.

[47]    R. Wu, X. Zhang, Y. Fan, R. Hu, X. Luo, A Bi-Layer compact thermal model for uniform chip temperature control with non-uniform heat sources by genetic-algorithm optimized microchannel cooling, Int. J. Therm. Sci. 136 (2019) 337–346. https://doi.org/10.1016/j.ijthermalsci.2018.10.047.

[48]    A. Radwan, S. Ookawara, M. Ahmed, Thermal management of concentrator photovoltaic systems using two-phase flow boiling in double-layer microchannel heat sinks, Appl. Energy. 241 (2019) 404–419. https://doi.org/10.1016/j.apenergy.2019.03.017.

[49]    S.G. Kandlikar, W.J. Grande, Evolution of microchannel flow passages-thermohydraulic performance and fabrication technology, Heat Transf. Eng. 24 (2003) 3–17. https://doi.org/10.1080/01457630304040.

[50]    K.M. Dowling, A.J. Suria, Y. Won, A. Shankar, H. Lee, M. Asheghi, K.E. Goodson, D.G. Senesky, Inductive coupled plasma etching of high aspect ratio silicon carbide microchannels for localized cooling, ASME 2015 Int. Tech. Conf. Exhib. Packag. Integr. Electron. Photonic Microsystems, InterPACK 2015, Collocated with ASME 2015 13th Int. Conf. Nanochannels, Microchannels, Minichannels. 3 (2015). https://doi.org/10.1115/IPACK2015-48409.

[51]    L. Chai, G. Xia, L. Wang, M. Zhou, Z. Cui, Heat transfer enhancement in microchannel heat sinks with periodic expansion-constriction cross-sections, Int. J. Heat Mass Transf. 62 (2013) 741–751. https://doi.org/10.1016/j.ijheatmasstransfer.2013.03.045.

[52]    A.K. Sahu, S. Jha, Microchannel fabrication and metallurgical characterization

128

on titanium by nanosecond fiber laser micromilling, Mater. Manuf. Process. 35 (2020) 279–290. https://doi.org/10.1080/10426914.2020.1718702.

[53]   F. Zhou, W. Ling, W. Zhou, Q. Qiu, X. Chu, Heat transfer characteristics of Cu-based microchannel heat exchanger fabricated by multi-blade milling process, Int. J. Therm. Sci. 138 (2019) 559–575. https://doi.org/10.1016/J.IJTHERMALSCI.2019.01.007.

[54]   D. Sreehari, A.K. Sharma, On thermal performance of serpentine silicon microchannels, Int. J. Therm. Sci. 146 (2019) 106067. https://doi.org/10.1016/j.ijthermalsci.2019.106067.

[55]   H. Liu, Y. Hovanski, D.D. Caldwell, R. Williford, Low-cost manufacturing of flow channels with multi-nozzle abrasive-waterjets: a feasibility investigation, Undefined. (2008).

[56]   P. Sarma, P.K. Patowari, Fabrication of Metallic Micromixers using WEDM and EDM for Application in Microfluidic Devices and Circuitries, Micro Nanosyst. 11 (2018). https://doi.org/10.2174/1876402911666181128125409.

[57]   M.A. Arie, A.H. Shooshtari, M.M. Ohadi, Experimental characterization of an additively manufactured heat exchanger for dry cooling of power plants, Appl. Therm. Eng. 129 (2018) 187–198. https://doi.org/10.1016/j.applthermaleng.2017.09.140.

[58]   L. Gong, K. Kota, W. Tao, Y. Joshi, Parametric numerical study of flow and heat transfer in microchannels with wavy walls, J. Heat Transfer. 133 (2011). https://doi.org/10.1115/1.4003284/468060.

[59]   S. Mehendale, A. Jacob, R. Shah, Fluid flow and heat transfer at micro-and meso-scales with application to heat exchanger design, 2000. http://appliedmechanicsreviews.asmedigitalcollection.asme.org/.

129

[60] P.A. Kew, K. Cornwell, Correlations for the prediction of boiling heat transfer in small-diameter channels, Appl. Therm. Eng. 17 (1997) 705–715. https://doi.org/10.1016/S1359-4311(96)00071-3.

[61] P. Cheng, H.Y. Wu, Mesoscale and Microscale Phase-Change Heat Transfer, Adv. Heat Transf. 39 (2006) 461–563. https://doi.org/10.1016/S0065-2717(06)39005-3.

[62] D. Wen, G. Lin, S. Vafaei, K. Zhang, Review of nanofluids for heat transfer applications, Particuology. 7 (2009) 141–150. https://doi.org/10.1016/j.partic.2009.01.007.

[63] H.A. Mohammed, P. Gunnasegaran, N.H. Shuaib, Influence of various base nanofluids and substrate materials on heat transfer in trapezoidal microchannel heat sinks, Int. Commun. Heat Mass Transf. 38 (2011) 194–201. https://doi.org/10.1016/j.icheatmasstransfer.2010.12.010.

[64] R. Muwanga, I. Hassan, Flow and heat transfer in a cross-linked silicon microchannel heat sink, J. Thermophys. Heat Transf. 22 (2008) 333–341. https://doi.org/10.2514/1.33952.

[65] S.W. Kang, S.C. Tseng, Analysis of effectiveness and pressure drop in micro cross-flow heat exchanger, Appl. Therm. Eng. 27 (2007) 877–885. https://doi.org/10.1016/j.applthermaleng.2006.09.002.

[66] G. Türkakar, T. Okutucu-Özyurt, Dimensional optimization of microchannel heat sinks with multiple heat sources, Int. J. Therm. Sci. 62 (2012) 85–92. https://doi.org/10.1016/J.IJTHERMALSCI.2011.12.015.

[67] T.C. Hung, W.M. Yan, Effects of tapered-channel design on thermal performance of microchannel heat sink, Int. Commun. Heat Mass Transf. 39 (2012) 1342–1347. https://doi.org/10.1016/j.icheatmasstransfer.2012.08.008.

130

[68]  M. Reyes, J.R. Arias, A. Velazquez, J.M. Vega, Experimental study of heat transfer and pressure drop in micro-channel based heat sinks with tip clearance, Appl. Therm. Eng. 31 (2011) 887–893. https://doi.org/10.1016/J.APPLTHERMALENG.2010.11.011.

[69]  J. Zhao, S. Huang, L. Gong, Z. Huang, Numerical study and optimizing on micro square pin-fin heat sink for electronic cooling, Appl. Therm. Eng. 93 (2016) 1347–1359. https://doi.org/10.1016/j.applthermaleng.2015.08.105.

[70]  G.D. Xia, J. Jiang, J. Wang, Y.L. Zhai, D.D. Ma, Effects of different geometric structures on fluid flow and heat transfer performance in microchannel heat sinks, Int. J. Heat Mass Transf. 80 (2015) 439–447. https://doi.org/10.1016/J.IJHEATMASSTRANSFER.2014.08.095.

[71]  A.J. Shkarah, M.Y. Bin Sulaiman, M.R.B.H. Ayob, H. Togun, A 3D numerical study of heat transfer in a single-phase micro-channel heat sink using graphene, aluminum and silicon as substrates, Int. Commun. Heat Mass Transf. 48 (2013) 108–115. https://doi.org/10.1016/J.ICHEATMASSTRANSFER.2013.08.006.

[72]  M.I. Hasan, Investigation of flow and heat transfer characteristics in micro pin fin heat sink with nanofluid, Appl. Therm. Eng. 63 (2014) 598–607. https://doi.org/10.1016/j.applthermaleng.2013.11.059.

[73]  M. Liu, D. Liu, S. Xu, Y. Chen, Experimental study on liquid flow and heat transfer in micro square pin fin heat sink, Int. J. Heat Mass Transf. 54 (2011) 5602–5611. https://doi.org/10.1016/j.ijheatmasstransfer.2011.07.013.

[74]  H. Shafeie, O. Abouali, K. Jafarpur, G. Ahmadi, Numerical study of heat transfer performance of single-phase heat sinks with micro pin-fin structures, Appl. Therm. Eng. 58 (2013) 68–76. https://doi.org/10.1016/j.applthermaleng.2013.04.008.

131

[75]   Y. Li, F. Zhang, B. Sunden, G. Xie, Laminar thermal performance of microchannel heat sinks with constructal vertical Y-shaped bifurcation plates, Appl. Therm. Eng. 73 (2014) 185–195. https://doi.org/10.1016/J.APPLTHERMALENG.2014.07.031.

[76]   G. Xie, S. Li, B. Sunden, W. Zhang, H. Li, A numerical study of the thermal performance of microchannel heat sinks with multiple length bifurcation in laminar liquid flow, Numer. Heat Transf. Part A Appl. 65 (2014) 107–126. https://doi.org/10.1080/10407782.2013.826084.

[77]   G. Xie, F. Zhang, B. Sundén, W. Zhang, Constructal design and thermal analysis of microchannel heat sinks with multistage bifurcations in single-phase liquid flow, Appl. Therm. Eng. 62 (2014) 791–802. https://doi.org/10.1016/J.APPLTHERMALENG.2013.10.042.

[78]   Y. Chen, C. Zhang, M. Shi, J.W.-I.C. in H. and,  undefined 2009, Three-dimensional numerical simulation of heat and fluid flow in noncircular microchannel heat sinks, Elsevier. (n.d.). https://www.sciencedirect.com/science/article/pii/S0735193309001444?casa_token=ZqheJOQxmlMAAAAA:zgV5QgVfnq8Vz_4Nlm9a2ah5Z3weMyJdITD_R-QHx6aTZqr7rTG-h0bklZ5uL9YG_gWBPlg (accessed September 19, 2021).

[79]   H.A. Mohammed, P. Gunnasegaran, N.H. Shuaib, Influence of channel shape on the thermal and hydraulic performance of microchannel heat sink, Int. Commun. Heat Mass Transf. 38 (2011) 474–480. https://doi.org/10.1016/J.ICHEATMASSTRANSFER.2010.12.031.

[80]   A.A. Alfaryjat, H.A. Mohammed, N.M. Adam, M.K.A. Ariffin, M.I. Najafabadi, Influence of geometrical parameters of hexagonal, circular, and

132

rhombus microchannel heat sinks on the thermohydraulic characteristics, Int. Commun. Heat Mass Transf. 52 (2014) 121–131. https://doi.org/10.1016/J.ICHEATMASSTRANSFER.2014.01.015.

[81]  L. Biswal, S. Chakraborty, S.K. Som, Design and optimization of single-phase liquid cooled microchannel heat sink, IEEE Trans. Components Packag. Technol. 32 (2009) 876–886. https://doi.org/10.1109/TCAPT.2009.2025598.

[82]  C.H. Hsu, H.S. Dang, T.A.T. Nguyen, The application of Fibonacci sequence and Taguchi method for investigating the design parameters on spiral micro-channel, in: 2016 Int. Conf. Appl. Syst. Innov. IEEE ICASI 2016, Institute of Electrical and Electronics Engineers Inc., 2016. https://doi.org/10.1109/ICASI.2016.7539784.

[83]  S. Ahmad, S. Gangwar, P.C. Yadav, D.K. Singh, Optimization of process parameters affecting surface roughness in magnetic abrasive finishing process, Mater. Manuf. Process. 32 (2017) 1723–1729. https://doi.org/10.1080/10426914.2017.1279307.

[84]  A. Yildizeli, S. Cadirci, Multi objective optimization of a micro-channel heat sink through genetic algorithm, Int. J. Heat Mass Transf. 146 (2020) 118847. https://doi.org/10.1016/j.ijheatmasstransfer.2019.118847.

[85]  S. Ahmad, R.M. Singari, R.S. Mishra, Tri-objective constrained optimization of pulsating DC sourced magnetic abrasive finishing process parameters using artificial neural network and genetic algorithm, Mater. Manuf. Process. 36 (2021) 843–857. https://doi.org/10.1080/10426914.2020.1866196.

[86]  L.K. Gallos, C. Song, H.A. Makse, A review of fractality and self-similarity in complex networks, Phys. A Stat. Mech. Its Appl. 386 (2007) 686–691. https://doi.org/10.1016/j.physa.2007.07.069.

133

[87]    M. CD, The Physiological Principle of Minimum Work: I. The Vascular System and the Cost of Blood Volume, Proc. Natl. Acad. Sci. U. S. A. 12 (1926) 207–214. https://doi.org/10.1073/PNAS.12.3.207.

[88]    X. Zheng, G. Shen, C. Wang, Y. Li, D. Dunphy, T. Hasan, C.J. Brinker, B.L. Su, Bio-inspired Murray materials for mass transfer and activity, Nat. Commun. 8 (2017) 1–9. https://doi.org/10.1038/ncomms14921.

[89]    A. Bejan, L.A.O. Rocha, S. Lorente, Thermodynamic optimization of geometry: T- and Y-shaped constructs of fluid streams, Int. J. Therm. Sci. 39 (2000) 949–960. https://doi.org/10.1016/S1290-0729(00)01176-5.

[90]    P. Xu, A.P. Sasmito, B. Yu, A.S. Mujumdar, Transport Phenomena and Properties in Treelike Networks, Appl. Mech. Rev. 68 (2016). https://doi.org/10.1115/1.4033966.

[91]    B.B. Mandelbrot, How long is the coast of Britain? Statistical self-similarity and fractional dimension, Science (80-. ). 156 (1967) 636–638. https://doi.org/DOI: 10.1126/science.156.3775.636.

[92]    G.M. Hutchins, M.M. Miner, J.K. Boitnott, Vessel caliber and branch-angle of human coronary artery branch-points., Circ. Res. 38 (1976) 572–576. https://doi.org/10.1161/01.RES.38.6.572.

[93]    M. LaBarbera, Principles of design of fluid transport systems in zoology, Science (80-. ). 249 (1990) 992–1000. https://doi.org/10.1126/SCIENCE.2396104.

[94]    Z. M, B. N, Arterial branching in various parts of the cardiovascular system, Am. J. Anat. 163 (1982) 295–307. https://doi.org/10.1002/AJA.1001630403.

[95]    T.A. WILSON, Design of the Bronchial Tree, Nat. 1967 2135077. 213 (1967) 668–669. https://doi.org/10.1038/213668a0.

134

[96]  H. K, C. G, Angles of branching and diameters of branches in the human bronchial tree, Bull. Math. Biophys. 29 (1967) 245–259. https://doi.org/10.1007/BF02476898.

[97]  K.A. McCulloh, J.S. Sperry, F.R. Adler, Water transport in plants obeys Murray's law, Nature. 421 (2003) 939–942. https://doi.org/10.1038/nature01444.

[98]  Y. Chen, P. Cheng, Heat transfer and pressure drop in fractal tree-like microchannel nets, Int. J. Heat Mass Transf. 45 (2002) 2643–2648. https://doi.org/10.1016/S0017-9310(02)00013-3.

[99]  A. Bejan, S. Lorente, Constructal theory of generation of configuration in nature and engineering, J. Appl. Phys. 100 (2006). https://doi.org/10.1063/1.2221896.

[100]  X.Q. Wang, P. Xu, A.S. Mujumdar, C. Yap, Flow and thermal characteristics of offset branching network, Int. J. Therm. Sci. 49 (2010) 272–280. https://doi.org/10.1016/j.ijthermalsci.2009.07.019.

[101]  B.B. Mandelbrot, The Fractal Geometry of Nature, Freeman, New York, 1982. https://ejournal.unisba.ac.id/index.php/kajian_akuntansi/article/view/2615%0Ahttp://scholar.unand.ac.id/60566/.

[102]  A. Bejan, M.R. Errera, Deterministic tree networks for fluid flow: Geometry for minimal flow resistance between a volume and one point, Fractals. 5 (1997) 685–695. https://doi.org/10.1142/S0218348X97000553.

[103]  A. Bejan, The tree of convective heat streams: Its thermal insulation function and the predicted 3/4-power relation between body heat loss and body size, Int. J. Heat Mass Transf. 44 (2001) 699–704. https://doi.org/10.1016/S0017-9310(00)00138-1.

135

[104]  A. Bejan, Shape and structure, from engineering to nature, (2000) 324.

[105]  A.K. Da Silva, S. Lorente, A. Bejan, Constructal multi-scale tree-shaped heat exchangers, J. Appl. Phys. 96 (2004) 1709–1718. https://doi.org/10.1063/1.1766089.

[106]  D. Pence, Reduced pumping power and wall temperature in microchannel heat sinks with fractal-like branching channel networks, Microscale Thermophys. Eng. 6 (2003) 319–330. https://doi.org/10.1080/10893950290098359.

[107]  S.M. Senn, D. Poulikakos, Laminar mixing, heat transfer and pressure drop in tree-like microchannel nets and their application for thermal management in polymer electrolyte fuel cells, J. Power Sources. 130 (2004) 178–191. https://doi.org/10.1016/j.jpowsour.2003.12.025.

[108]  X.Q. Wang, A.S. Mujumdar, C. Yap, Thermal characteristics of tree-shaped microchannel nets for cooling of a rectangular heat sink, Int. J. Therm. Sci. 45 (2006) 1103–1112. https://doi.org/10.1016/j.ijthermalsci.2006.01.010.

[109]  T.F. Sherman, On connecting large vessels to small. The Meaning of Murray's Law, J. Gen. Physiol. 78 (1981) 431–453. https://doi.org/10.1085/jgp.78.4.431.

[110]  J. Kou, Y. Chen, X. Zhou, H. Lu, F. Wu, J. Fan, Optimal structure of tree-like branching networks for fluid flow, Phys. A Stat. Mech. Its Appl. 393 (2014) 527–534. https://doi.org/10.1016/j.physa.2013.08.029.

[111]  H. UYLINGS, Optimization of diameters and bifurcation angles in lung and vascular tree structures, Bull. Math. Biol. 39 (1977) 509–520. https://doi.org/10.1016/S0092-8240(77)80054-2.

[112]  D.R. Emerson, K. Cieślicki, X. Gu, R.W. Barber, Biomimetic design of microfluidic manifolds based on a generalised Murray's law, Lab Chip. 6 (2006) 447–454. https://doi.org/10.1039/b516975e.

136

[113] A. Bejan, Constructal-theory network of conducting paths for cooling a heat generating volume, Int. J. Heat Mass Transf. 40 (1997) 799–811. https://doi.org/10.1016/0017-9310(96)00175-5.

[114] C. Zhang, Y. Chen, R. Wu, M. Shi, Flow boiling in constructal tree-shaped minichannel network, Int. J. Heat Mass Transf. 54 (2011) 202–209. https://doi.org/10.1016/j.ijheatmasstransfer.2010.09.051.

[115] R. Revellin, J.R. Thome, A. Bejan, J. Bonjour, Constructal tree-shaped microchannel networks for maximizing the saturated critical heat flux, Int. J. Therm.          Sci.          48          (2009)          342–352. https://doi.org/10.1016/j.ijthermalsci.2008.06.009.

[116] Y. Peng, X. Zhu, B. Cao, Y. Luo, W. Zhou, Heat transfer and permeability of the tree-like branching networks, Int. J. Heat Mass Transf. 129 (2019) 801–811. https://doi.org/10.1016/j.ijheatmasstransfer.2018.09.121.

[117] A.F. Miguel, Optimal Y-shaped constructs heat sinks under different size constraints,   Int.   J.   Heat   Mass   Transf.   131   (2019)   64–71. https://doi.org/10.1016/j.ijheatmasstransfer.2018.11.033.

[118] R.R. Zhiwei Huang , Yunho Hwang, Vikrant Aute, Review of Fractal Heat Exchangers, Int. Compress. Eng. Refrig. Air Cond. High Perform. Build. Conf. (2016) 1–9.

[119] G.B. West, J.H. Brown, B.J. Enquist, A general model for the origin of allometric scaling laws in biology, Science (80-. ). 276 (1997) 122–126. https://doi.org/10.1126/science.276.5309.122.

[120] A. Bejan, S. Lorente, J. Lee, Unifying constructal theory of tree roots, canopies and   forests,   J.   Theor.   Biol.   254   (2008)   529–540. https://doi.org/10.1016/j.jtbi.2008.06.026.

137

[121] A. Bejan, Constructal tree network for fluid flow between a finite-size volume and one source or sink, Rev. Gen. Therm. 36 (1997) 592–604. https://doi.org/10.1016/S0035-3159(97)89986-2.

[122] A. Bejan, Dendritic constructal heat exchanger with small-scale crossflows and larger-scales counterflows, Int. J. Heat Mass Transf. 45 (2002) 4607–4620. https://doi.org/10.1016/S0017-9310(02)00165-5.

[123] A. Bejan, Constructal tree-shaped paths for conduction and convection, Int. J. Energy Res. 27 (2003) 283–299. https://doi.org/10.1002/er.875.

[124] P. Xu, B. Yu, The scaling laws of transport properties for fractal-like tree networks, J. Appl. Phys. 100 (2006). https://doi.org/10.1063/1.2392935.

[125] Y. Chen, P. Cheng, An experimental investigation on the thermal efficiency of fractal tree-like microchannel nets, Int. Commun. Heat Mass Transf. 32 (2005) 931–938. https://doi.org/10.1016/j.icheatmasstransfer.2005.02.001.

[126] A.Y. Alharbi, D. V. Pence, R.N. Cullion, Fluid flow through microscale fractal-like branching channel networks, J. Fluids Eng. Trans. ASME. 125 (2003) 1051–1057. https://doi.org/10.1115/1.1625684.

[127] A.Y. Alharbi, D. V. Pence, R.N. Cullion, Thermal characteristics of microscale fractal-like branching channels, J. Heat Transfer. 126 (2004) 744–752. https://doi.org/10.1115/1.1795236.

[128] M. Sheikholeslami, M. Gorji-Bandpy, D.D. Ganji, Review of heat transfer enhancement methods: Focus on passive methods using swirl flow devices, Renew. Sustain. Energy Rev. 49 (2015) 444–469. https://doi.org/10.1016/j.rser.2015.04.113.

[129] Q. Esmaili, A.A. Ranjbar, S. Porkhial, Experimental analysis of heat transfer in ribbed microchannel, Int. J. Therm. Sci. 130 (2018) 140–147.

138

https://doi.org/10.1016/J.IJTHERMALSCI.2018.04.020.

[130] M.E. Steinke, S.G. Kandlikar, Single-phase heat transfer enhancement techniques in microchannel and minichannel flows, Proc. Second Int. Conf. Microchannels Minichannels. (2004) 141–148.

[131] S.G. Kandlikar, History, advances, and challenges in liquid flow and flow boiling heat transfer in microchannels: A critical review, J. Heat Transfer. 134 (2012). https://doi.org/10.1115/1.4005126.

[132] W.Q. Tao, Y.L. He, Q.W. Wang, Z.G. Qu, F.Q. Song, A unified analysis on enhancing single phase convective heat transfer with field synergy principle, Int. J. Heat Mass Transf. 45 (2002) 4871–4879. https://doi.org/10.1016/S0017-9310(02)00173-4.

[133] J.A. Choi, S.U.S. and Eastman, Enhancing Thermal Conductivity of Fluids with Nanoparticles. , San Francisco, 12-17 November 1995. - References - Scientific Research Publishing, ASME Int. Mech. Eng. Congr. Expo. (1995). https://www.scirp.org/reference/referencespapers?referenceid=2538717 (accessed July 19, 2025).

[134] G.D. Xia, Y.T. Jia, Y.F. Li, D.D. Ma, B. Cai, Numerical simulation and multiobjective optimization of a microchannel heat sink with arc-shaped grooves and ribs, Numer. Heat Transf. Part A Appl. 70 (2016) 1041–1055. https://doi.org/10.1080/10407782.2016.1230394.

[135] Y.F. Li, G.D. Xia, D.D. Ma, Y.T. Jia, J. Wang, Characteristics of laminar flow and heat transfer in microchannel heat sink with triangular cavities and rectangular ribs, Int. J. Heat Mass Transf. 98 (2016) 17–28. https://doi.org/10.1016/j.ijheatmasstransfer.2016.03.022.

[136] I.A. Ghani, N.A.C. Sidik, N. Kamaruzaman, Hydrothermal performance of

microchannel heat sink: The effect of channel design, Int. J. Heat Mass Transf. 107 (2017) 21–44. https://doi.org/10.1016/j.ijheatmasstransfer.2016.11.031.

[137] C. Chen, J.T. Teng, C.H. Cheng, S. Jin, S. Huang, C. Liu, M.T. Lee, H.H. Pan, R. Greif, A study on fluid flow and heat transfer in rectangular microchannels with various longitudinal vortex generators, Int. J. Heat Mass Transf. 69 (2014) 203–214. https://doi.org/10.1016/j.ijheatmasstransfer.2013.10.018.

[138] Z. Dai, D.F. Fletcher, B.S. Haynes, Impact of tortuous geometry on laminar flow heat transfer in microchannels, Int. J. Heat Mass Transf. 83 (2015) 382–398. https://doi.org/10.1016/J.IJHEATMASSTRANSFER.2014.12.019.

[139] Y. Sui, P.S. Lee, C.J. Teo, An experimental study of flow friction and heat transfer in wavy microchannels with rectangular cross section, Int. J. Therm. Sci. 50 (2011) 2473–2482. https://doi.org/10.1016/j.ijthermalsci.2011.06.017.

[140] G. Xia, L. Chai, H. Wang, M. Zhou, Z. Cui, Optimum thermal design of microchannel heat sink with triangular reentrant cavities, Appl. Therm. Eng. 31 (2011) 1208–1219. https://doi.org/10.1016/j.applthermaleng.2010.12.022.

[141] R. Chein, J. Chen, Numerical study of the inlet/outlet arrangement effect on microchannel heat sink performance, Int. J. Therm. Sci. 48 (2009) 1627–1638. https://doi.org/10.1016/j.ijthermalsci.2008.12.019.

[142] E. Utriainen, B. Sundén, Numerical analysis of a primary surface trapezoidal cross wavy duct, Int. J. Numer. Methods Heat Fluid Flow. 10 (2000) 634–648. https://doi.org/10.1108/09615530010347213.

[143] J. Rostami, A. Abbassi, Conjugate heat transfer in a wavy microchannel using nanofluid by two-phase Eulerian – Lagrangian method, Adv. POWDER Technol. (2015) 1–10. https://doi.org/10.1016/j.apt.2015.10.003.

[144] J. Rostami, A. Abbassi, J. Harting, Heat transfer by nanofluids in wavy

140

microchannels, Adv. Powder Technol. 29 (2018) 925–933. https://doi.org/10.1016/j.apt.2018.01.010.

[145] G. Lu, J. Zhao, L. Lin, X. Wang, W. Yan, A new scheme for reducing pressure drop and thermal resistance simultaneously in microchannel heat sinks with wavy porous fins, Int. J. Heat Mass Transf. 111 (2017) 1071–1078. https://doi.org/10.1016/j.ijheatmasstransfer.2017.04.086.

[146] A. Sakanova, J. Zhao, K. Tseng, Investigation on the Influence of Nanofluids in Wavy Microchannel Heat Sink, 5 (2015) 956–970. https://doi.org/10.1109/TCPMT.2015.2441114.

[147] D. Yuan, W. Zhou, T. Fu, C. Liu, Experimental and numerical investigation of heat and mass transfer in non-uniform wavy microchannels, Int. J. Therm. Sci. 152 (2020) 106320. https://doi.org/10.1016/j.ijthermalsci.2020.106320.

[148] H.A. Mohammed, P. Gunnasegaran, N.H. Shuaib, Numerical simulation of heat transfer enhancement in wavy microchannel heat sink, Int. Commun. Heat Mass Transf. 38 (2011) 63–68. https://doi.org/10.1016/j.icheatmasstransfer.2010.09.012.

[149] C.C. Cho, C.L. Chen, C.K. Chen, Characteristics of combined electroosmotic flow and pressure-driven flow in microchannels with complex-wavy surfaces, Int. J. Therm. Sci. 61 (2012) 94–105. https://doi.org/10.1016/j.ijthermalsci.2012.06.008.

[150] F. Bin Abdul Hasis, P.M. Mithun Krishna, G.P. Aravind, M. Deepu, S.R. Shine, Thermo hydraulic performance analysis of twisted sinusoidal wavy microchannels, Int. J. Therm. Sci. 128 (2018) 124–136. https://doi.org/10.1016/j.ijthermalsci.2018.02.018.

[151] Y. Sui, C.J. Teo, P.S. Lee, Direct numerical simulation of fluid flow and heat

141

transfer in periodic wavy channels with rectangular cross-sections Y., Int. J. Heat Mass Transf. 55 (2012) 73–88. https://doi.org/10.1016/j.ijheatmasstransfer.2011.08.041.

[152] L. Lin, J. Zhao, G. Lu, X.D. Wang, W.M. Yan, Heat transfer enhancement in microchannel heat sink by wavy channel with changing wavelength/amplitude, Int. J. Therm. Sci. 118 (2017) 423–434. https://doi.org/10.1016/j.ijthermalsci.2017.05.013.

[153] J.F. Zhu, X.Y. Li, S.L. Wang, Y.R. Yang, X.D. Wang, Performance comparison of wavy microchannel heat sinks with wavy bottom rib and side rib designs, Int. J. Therm. Sci. 146 (2019) 106068. https://doi.org/10.1016/j.ijthermalsci.2019.106068.

[154] H. Ermagan, R. Rafee, Numerical investigation into the thermo-fluid performance of wavy microchannels with superhydrophobic walls, Int. J. Therm. Sci. 132 (2018) 578–588. https://doi.org/10.1016/j.ijthermalsci.2018.06.035.

[155] Z.H. Foo, K.X. Cheng, A.L. Goh, K.T. Ooi, Single-phase convective heat transfer performance of wavy microchannels in macro geometry, Appl. Therm. Eng. 141 (2018) 675–687. https://doi.org/10.1016/j.applthermaleng.2018.06.015.

[156] H. Shen, Y. Zhang, C.C. Wang, G. Xie, Comparative study for convective heat transfer of counter-flow wavy double-layer microchannel heat sinks in staggered arrangement, Appl. Therm. Eng. 137 (2018) 228–237. https://doi.org/10.1016/j.applthermaleng.2018.03.089.

[157] G. Xie, J. Liu, Y. Liu, B. Sunden, W. Zhang, Comparative study of thermal performance of longitudinal and transversal-wavy microchannel heat sinks for

142

electronic cooling, J. Electron. Packag. 135 (2013). https://doi.org/10.1115/1.4023530/372494.

[158] T.K. Nandi, H. Chattopadhyay, Numerical investigations of simultaneously developing flow in wavy microchannels under pulsating inlet flow condition, Int. Commun. Heat Mass Transf. 47 (2013) 27–31. https://doi.org/10.1016/j.icheatmasstransfer.2013.06.008.

[159] Z. Lin, P. Seng, P. Kumar, N. Mou, Investigation of fluid flow and heat transfer in wavy micro-channels with alternating secondary branches, Int. J. Heat Mass Transf. 101 (2016) 1316–1330. https://doi.org/10.1016/j.ijheatmasstransfer.2016.05.097.

[160] A. Sakanova, C.C. Keian, J. Zhao, Performance improvements of microchannel heat sink using wavy channel and nanofluids, Int. J. Heat Mass Transf. 89 (2015) 59–74. https://doi.org/10.1016/j.ijheatmasstransfer.2015.05.033.

[161] J. Rostami, A. Abbassi, M. Saffar-Avval, Optimization of conjugate heat transfer in wavy walls microchannels, Appl. Therm. Eng. 82 (2015) 318–328. https://doi.org/10.1016/j.applthermaleng.2015.02.069.

[162] G. Xie, Z. Chen, B. Sunden, W. Zhang, Comparative study of the flow and thermal performance of liquid-cooling parallel-flow and counter-flow double-layer wavy microchannel heat sinks, Numer. Heat Transf. Part A Appl. 64 (2013) 30–55. https://doi.org/10.1080/10407782.2013.773811.

[163] A.F. Al-Neama, N. Kapur, J. Summers, H.M. Thompson, An experimental and numerical investigation of the use of liquid flow in serpentine microchannels for microelectronics cooling, Appl. Therm. Eng. 116 (2017) 709–723. https://doi.org/10.1016/j.applthermaleng.2017.02.001.

[164] D. Sreehari, A.K. Sharma, On thermal performance of serpentine silicon

143

microchannels, Int. J. Therm. Sci. 146 (2019). https://doi.org/10.1016/J.IJTHERMALSCI.2019.106067.

[165] X. Liu, H. Zhang, C. Zhu, F. Wang, Z. Li, Effects of structural parameters on fluid flow and heat transfer in a serpentine microchannel with fan-shaped reentrant cavities, Appl. Therm. Eng. 151 (2019) 406–416. https://doi.org/10.1016/j.applthermaleng.2019.02.033.

[166] M. Rahimi, M. Hajialyani, R. Beigzadeh, A.A. Alsairafi, Application of artificial neural network and genetic algorithm approaches for prediction of flow characteristic in serpentine microchannels, Chem. Eng. Res. Des. 98 (2015) 147–156. https://doi.org/10.1016/j.cherd.2015.05.005.

[167] R. Filimonov, J. Sorvari, Numerical study on the effect of cross-section orientation on fluid flow and heat transfer in a periodic serpentine triangular microchannel, Appl. Therm. Eng. 125 (2017) 366–376. https://doi.org/10.1016/j.applthermaleng.2017.07.027.

[168] C.Y. Huang, B.H. Huang, F.R. Cheng, S.W. Chen, T.M. Liou, Experimental study of heat transfer enhancement with segmented flow in a microchannel by using molecule-based temperature sensors, Int. J. Heat Mass Transf. 107 (2017) 657–666. https://doi.org/10.1016/j.ijheatmasstransfer.2016.11.063.

[169] D. Toghraie, M.M.D. Abdollah, F. Pourfattah, O.A. Akbari, B. Ruhani, Numerical investigation of flow and heat transfer characteristics in smooth, sinusoidal and zigzag-shaped microchannel with and without nanofluid, J. Therm. Anal. Calorim. 131 (2018) 1757–1766. https://doi.org/10.1007/s10973-017-6624-6.

[170] W. Duangthongsuk, S. Wongwises, An experimental investigation on the heat transfer and pressure drop characteristics of nanofluid flowing in microchannel

144

heat sink with multiple zigzag flow channel structures, Exp. Therm. Fluid Sci. 87 (2017) 30–39. https://doi.org/10.1016/j.expthermflusci.2017.04.013.

[171] K.X. Cheng, Y.S. Chong, K.T. Ooi, Thermal-hydraulic performance of a tapered microchannel, Int. Commun. Heat Mass Transf. 94 (2018) 53–60. https://doi.org/10.1016/j.icheatmasstransfer.2018.03.008.

[172] N. Raja Kuppusamy, R. Saidur, N.N.N. Ghazali, H.A. Mohammed, Numerical study of thermal enhancement in micro channel heat sink with secondary flow, Int. J. Heat Mass Transf. 78 (2014) 216–223. https://doi.org/10.1016/j.ijheatmasstransfer.2014.06.072.

[173] X. Shi, S. Li, Y. Mu, B. Yin, Geometry parameters optimization for a microchannel heat sink with secondary flow channel, Int. Commun. Heat Mass Transf. 104 (2019) 89–100. https://doi.org/10.1016/j.icheatmasstransfer.2019.03.009.

[174] Y. Fan, P.S. Lee, L.W. Jin, B.W. Chua, A simulation and experimental study of fluid flow and heat transfer on cylindrical oblique-finned heat sink, Int. J. Heat Mass Transf. 61 (2013) 62–72. https://doi.org/10.1016/j.ijheatmasstransfer.2013.01.075.

[175] Y.J. Lee, P.S. Lee, S.K. Chou, Numerical study of fluid flow and heat transfer in the enhanced microchannel with oblique fins, J. Heat Transfer. 135 (2013) 1–10. https://doi.org/10.1115/1.4023029.

[176] M. Law, P.S. Lee, Effects of varying secondary channel widths on flow boiling heat transfer and pressure characteristics in oblique-finned microchannels, Int. J. Heat Mass Transf. 101 (2016) 313–326. https://doi.org/10.1016/j.ijheatmasstransfer.2016.05.055.

[177] M. Law, P.S. Lee, A comparative study of experimental flow boiling heat

145

transfer and pressure characteristics in straight- and oblique-finned microchannels, Int. J. Heat Mass Transf. 85 (2015) 797–810. https://doi.org/10.1016/j.ijheatmasstransfer.2015.01.137.

[178] B. Rajabi Far, S.K. Mohammadian, S.K. Khanna, Y. Zhang, Effects of pin tip-clearance on the performance of an enhanced microchannel heat sink with oblique fins and phase change material slurry, Int. J. Heat Mass Transf. 83 (2015) 136–145. https://doi.org/10.1016/j.ijheatmasstransfer.2014.11.082.

[179] S. Soleimanikutanaei, E. Ghasemisahebi, C.X. Lin, Numerical study of heat transfer enhancement using transverse microchannels in a heat sink, Int. J. Therm. Sci. 125 (2018) 89–100. https://doi.org/10.1016/j.ijthermalsci.2017.11.009.

[180] K.C. Wong, J.H. Lee, Investigation of thermal performance of microchannel heat sink with triangular ribs in the transverse microchambers, Int. Commun. Heat Mass Transf. 65 (2015) 103–110. https://doi.org/10.1016/j.icheatmasstransfer.2015.04.011.

[181] L. Chai, L. Wang, Thermal-hydraulic performance of interrupted microchannel heat sinks with different rib geometries in transverse microchambers, Int. J. Therm. Sci. 127 (2018) 201–212. https://doi.org/10.1016/j.ijthermalsci.2018.01.029.

[182] K.C. Wong, M.L. Ang, Thermal hydraulic performance of a double-layer microchannel heat sink with channel contraction, Int. Commun. Heat Mass Transf. 81 (2017) 269–275. https://doi.org/10.1016/j.icheatmasstransfer.2016.09.013.

[183] K. Vafai, L. Zhu, Analysis of two-layered micro-channel heat sink concept in electronic cooling, Int. J. Heat Mass Transf. 42 (1999) 2287–2297.

146

https://doi.org/10.1016/S0017-9310(98)00017-9.

[184]   X.Y. Li, S.L. Wang, X.D. Wang, T.H. Wang, Selected porous-ribs design for performance improvement in double-layered microchannel heat sinks, Int. J. Therm.         Sci.         137         (2019)         616–626. https://doi.org/10.1016/j.ijthermalsci.2018.12.029.

[185]   A.A.A. Arani, O.A. Akbari, M.R. Safaei, A. Marzban, A.A.A.A. Alrashed, G.R. Ahmadi, T.K. Nguyen, Heat transfer improvement of water/single-wall carbon nanotubes (SWCNT) nanofluid in a novel design of a truncated double-layered microchannel heat sink, Int. J. Heat Mass Transf. 113 (2017) 780–795. https://doi.org/10.1016/j.ijheatmasstransfer.2017.05.089.

[186]   A. Sarlak, A. Ahmadpour, M.R. Hajmohammadi, Thermal design improvement of a double-layered microchannel heat sink by using multi-walled carbon nanotube (MWCNT) nanofluids with non-Newtonian viscosity, Appl.         Therm.         Eng.         147         (2019)         205–215. https://doi.org/10.1016/j.applthermaleng.2018.10.084.

[187]   C. Leng, X.D. Wang, T.H. Wang, W.M. Yan, Multi-parameter optimization of flow and heat transfer for a novel double-layered microchannel heat sink, Int. J.       Heat       Mass       Transf.       84       (2015)       359–369. https://doi.org/10.1016/j.ijheatmasstransfer.2015.01.040.

[188]   T.H. Wang, H.C. Wu, J.H. Meng, W.M. Yan, Optimization of a double-layered microchannel heat sink with semi-porous-ribs by multi-objective genetic algorithm,   Int.   J.   Heat   Mass   Transf.   149   (2020)   119217. https://doi.org/10.1016/j.ijheatmasstransfer.2019.119217.

[189]   F. Zhou, W. Zhou, Q. Qiu, W. Yu, X. Chu, Investigation of fluid flow and heat transfer characteristics of parallel flow double-layer microchannel heat

147

exchanger, Appl. Therm. Eng. 137 (2018) 616–631. https://doi.org/10.1016/j.applthermaleng.2018.03.069.

[190] R. Mashayekhi, E. Khodabandeh, O.A. Akbari, D. Toghraie, M. Bahiraei, M. Gholami, CFD analysis of thermal and hydrodynamic characteristics of hybrid nanofluid in a new designed sinusoidal double-layered microchannel heat sink, J. Therm. Anal. Calorim. 134 (2018) 2305–2315. https://doi.org/10.1007/s10973-018-7671-3.

[191] J.M. Wu, J.Y. Zhao, K.J. Tseng, Parametric study on the performance of double-layered microchannels heat sink, Energy Convers. Manag. 80 (2014) 550–560. https://doi.org/10.1016/j.enconman.2014.01.014.

[192] D. Jing, L. He, X. Wang, Optimization analysis of fractal tree-like microchannel network for electroviscous flow to realize minimum hydraulic resistance, Int. J. Heat Mass Transf. 125 (2018) 749–755. https://doi.org/10.1016/j.ijheatmasstransfer.2018.04.115.

[193] D. Jing, J. Song, Y.I. Sui, HYDRAULIC AND THERMAL PERFORMANCES OF LAMINAR FLOW IN FRACTAL TREELIKE BRANCHING MICROCHANNEL NETWORK WITH WALL VELOCITY SLIP, Fractals. 28 (2020) 1–10. https://doi.org/10.1142/S0218348X2050022X.

[194] F.J. Hong, P. Cheng, H. Ge, G.T. Joo, Conjugate heat transfer in fractal-shaped microchannel network heat sink for integrated microelectronic cooling application, Int. J. Heat Mass Transf. 50 (2007) 4986–4998. https://doi.org/10.1016/j.ijheatmasstransfer.2007.09.006.

[195] H. Tan, L. Wu, M. Wang, Z. Yang, P. Du, Heat transfer improvement in microchannel heat sink by topology design and optimization for high heat flux chip cooling, Int. J. Heat Mass Transf. 129 (2019) 681–689.

148

https://doi.org/10.1016/j.ijheatmasstransfer.2018.09.092.

[196] L. Ghodoossi, Thermal and hydrodynamic analysis of a fractal microchannel network, Energy Convers. Manag. 46 (2005) 771–788. https://doi.org/10.1016/j.enconman.2004.05.008.

[197] S. Xu, Y. Li, X. Hu, L. Yang, Characteristics of heat transfer and fluid flow in a fractal multilayer silicon microchannel, Int. Commun. Heat Mass Transf. 71 (2016) 86–95. https://doi.org/10.1016/j.icheatmasstransfer.2015.12.024.

[198] C.P. Zhang, Y.F. Lian, C.H. Hsu, J.T. Teng, S. Liu, Y.J. Chang, R. Greif, Investigations of thermal and flow behavior of bifurcations and bends in fractal-like microchannel networks: Secondary flow and recirculation flow, Int. J. Heat Mass Transf. 85 (2015) 723–731. https://doi.org/10.1016/j.ijheatmasstransfer.2015.01.118.

[199] D. Heymann, D. Pence, V. Narayanan, Optimization of fractal-like branching microchannel heat sinks for single-phase flows, Int. J. Therm. Sci. 49 (2010) 1383–1393. https://doi.org/10.1016/j.ijthermalsci.2010.01.015.

[200] Y. Yan, H. Yan, S. Feng, L. Li, Thermal-hydraulic performances and synergy effect between heat and flow distribution in a truncated doubled-layered heat sink with Y-shaped fractal network, Int. J. Heat Mass Transf. 142 (2019) 118337. https://doi.org/10.1016/j.ijheatmasstransfer.2019.06.093.

[201] C.P. Zhang, Y.F. Lian, X.F. Yu, W. Liu, J.T. Teng, T.T. Xu, C.H. Hsu, Y.J. Chang, R. Greif, Numerical and experimental studies on laminar hydrodynamic and thermal characteristics in fractal-like microchannel networks. Part A: Comparisons of two numerical analysis methods on friction factor and Nusselt number, Int. J. Heat Mass Transf. 66 (2013) 930–938. https://doi.org/10.1016/j.ijheatmasstransfer.2013.06.073.

149

[202] C.P. Zhang, Y.F. Lian, X.F. Yu, W. Liu, J.T. Teng, T.T. Xu, C.H. Hsu, Y.J. Chang, R. Greif, Numerical and experimental studies on laminar hydrodynamic and thermal characteristics in fractal-like microchannel networks. Part B: Investigations on the performances of pressure drop and heat transfer, Int. J. Heat Mass Transf. 66 (2013) 939–947. https://doi.org/10.1016/j.ijheatmasstransfer.2013.07.021.

[203] X.F. Yu, C.P. Zhang, J.T. Teng, S.Y. Huang, S.P. Jin, Y.F. Lian, C.H. Cheng, T.T. Xu, J.C. Chu, Y.J. Chang, T. Dang, R. Greif, A study on the hydraulic and thermal characteristics in fractal tree-like microchannels by numerical and experimental methods, Int. J. Heat Mass Transf. 55 (2012) 7499–7507. https://doi.org/10.1016/j.ijheatmasstransfer.2012.07.050.

[204] S.M. Senn, D. Poulikakos, Laminar mixing, heat transfer and pressure drop in tree-like microchannel nets and their application for thermal management in polymer electrolyte fuel cells, J. Power Sources. 130 (2004) 178–191. https://doi.org/10.1016/j.jpowsour.2003.12.025.

[205] D. Haller, P. Woias, N. Kockmann, Simulation and experimental investigation of pressure loss and heat transfer in microchannel networks containing bends and T-junctions, Int. J. Heat Mass Transf. 52 (2009) 2678–2689. https://doi.org/10.1016/j.ijheatmasstransfer.2008.09.042.

[206] Z. Lu, K. Zhang, J. Liu, F. Li, Effect of branching level on the performance of constructal theory based Y-shaped liquid cooling heat sink, Appl. Therm. Eng. 168 (2020) 114824. https://doi.org/10.1016/j.applthermaleng.2019.114824.

[207] M. Farzaneh, M.R. Salimpour, M.R. Tavakoli, Design of bifurcating microchannels with/without loops for cooling of square-shaped electronic components, Appl. Therm. Eng. 108 (2016) 581–595.

150

https://doi.org/10.1016/j.applthermaleng.2016.07.099.

[208] Y. Yan, Z. He, G. Wu, L. Zhang, Z. Yang, L. Li, Influence of hydrogels embedding positions on automatic adaptive cooling of hot spot in fractal microchannel heat sink, Int. J. Therm. Sci. 155 (2020) 106428. https://doi.org/10.1016/j.ijthermalsci.2020.106428.

[209] Y. Yan, H. Yan, S. Yin, L. Zhang, L. Li, Single/multi-objective optimizations on hydraulic and thermal management in micro-channel heat sink with bionic Y-shaped fractal network by genetic algorithm coupled with numerical simulation, Int. J. Heat Mass Transf. 129 (2019) 468–479. https://doi.org/10.1016/j.ijheatmasstransfer.2018.09.120.

[210] Y. Wang, L. Huang, D. Mei, Y. Feng, M. Qian, Numerical modeling of microchannel reactor with porous surface microstructure based on fractal geometry, Int. J. Hydrogen Energy. 43 (2018) 22447–22457. https://doi.org/10.1016/j.ijhydene.2018.10.135.

[211] S. Xu, W. Wang, K. Fang, C.N. Wong, Heat transfer performance of a fractal silicon microchannel heat sink subjected to pulsation flow, Int. J. Heat Mass Transf. 81 (2015) 33–40. https://doi.org/10.1016/j.ijheatmasstransfer.2014.10.002.

[212] L. Liang, J. Hou, X. Fang, Y. Han, J. Song, L. Wang, Z. Deng, G. Xu, H. Wu, Flow characteristics and heat transfer performance in a Y-Fractal mini/microchannel heat sink, Case Stud. Therm. Eng. 15 (2019) 100522. https://doi.org/10.1016/j.csite.2019.100522.

[213] H. Tan, K. Zong, P. Du, Temperature uniformity in convective leaf vein-shaped fluid microchannels for phased array antenna cooling, Int. J. Therm. Sci. 150 (2020) 106224. https://doi.org/10.1016/j.ijthermalsci.2019.106224.

151

[214]   P. Huang, G. Dong, X. Zhong, M. Pan, Numerical investigation of the fluid flow and heat transfer characteristics of tree-shaped microchannel heat sink with variable cross-section, Chem. Eng. Process. - Process Intensif. 147 (2020) 107769. https://doi.org/10.1016/j.cep.2019.107769.

[215]   D. Zhuang, Y. Yang, G. Ding, X. Du, Z. Hu, Optimization of Microchannel Heat Sink with Rhombus Fractal-like Units for Electronic Chip Cooling, Int. J. Refrig. 116 (2020) 108–118. https://doi.org/10.1016/j.ijrefrig.2020.03.026.

[216]   Z. Lyu, F. Pourfattah, A.A.A. Arani, A. Asadi, L.K. Foong, On the Thermal Performance of a Fractal Microchannel Subjected to Water and Kerosene Carbon Nanotube Nanofluid, Sci. Rep. 10 (2020) 1–16. https://doi.org/10.1038/s41598-020-64142-w.

[217]   W.T. Yan, C. Li, W.B. Ye, Numerical investigation of hydrodynamic and heat transfer performances of nanofluids in a fractal microchannel heat sink, Heat Transf. - Asian Res. 48 (2019) 2329–2349. https://doi.org/10.1002/htj.21494.

[218]   H.L. Liu, X.K. An, C.S. Wang, Heat transfer performance of T-Y type micro-channel heat sink with liquid GaInSn coolant, Int. J. Therm. Sci. 120 (2017) 203–219. https://doi.org/10.1016/j.ijthermalsci.2017.06.008.

[219]   Y. Chen, C. Zhang, M. Shi, Y. Yang, Thermal and hydrodynamic characteristics of constructal tree-shaped minichannel heat sink, AIChE J. 56 (2010) 2018–2029. https://doi.org/10.1002/aic.

[220]   C. Xia, J. Fu, J. Lai, X. Yao, Z. Chen, Conjugate heat transfer in fractal tree-like channels network heat sink for high-speed motorized spindle cooling, Appl. Therm. Eng. 90 (2015) 1032–1042. https://doi.org/10.1016/j.applthermaleng.2015.07.024.

[221]   R. Brinda, R. Joseph Daniel, K. Sumangala, Ladder shape micro channels

152

employed high performance micro cooling system for ULSI, Int. J. Heat Mass Transf. 55 (2012) 3400–3411. https://doi.org/10.1016/j.ijheatmasstransfer.2012.03.044.

[222] S. Riera, J. Barrau, M. Omri, L.G. Fréchette, J.I. Rosell, Stepwise varying width microchannel cooling device for uniform wall temperature: Experimental and numerical study, Appl. Therm. Eng. 78 (2015) 30–38. https://doi.org/10.1016/j.applthermaleng.2014.12.012.

[223] Y. Tang, Z. He, M. Pan, J. Wang, Ring-shaped microchannel heat exchanger based on turning process, Exp. Therm. Fluid Sci. 34 (2010) 1398–1402. https://doi.org/10.1016/j.expthermflusci.2010.06.015.

[224] P. Li, D. Zhang, Y. Xie, G. Xie, Flow structure and heat transfer of non-Newtonian fluids in microchannel heat sinks with dimples and protrusions, Appl. Therm. Eng. 94 (2016) 50–58. https://doi.org/10.1016/j.applthermaleng.2015.10.119.

[225] X.J. Wei, Y.K. Joshi, P.M. Ligrani, Numerical simulation of laminar flow and heat transfer inside a microchannel with one dimpled surface, J. Electron. Packag. Trans. ASME. 129 (2007) 63–70. https://doi.org/10.1115/1.2429711.

[226] V.Y. Rudyak, M.I. Pryazhnikov, A. V. Minakov, Thermal Conductivity, Rheology and Electrical Conductivity of Water- and Ethylene Glycol-Based Nanofluids with Copper and Aluminum Particles, Phys. Mesomech. 27 (2024) 205–216. https://doi.org/10.1134/S1029959924020097/METRICS.

[227] J. Matouq, R. Al-Waked, M. Al-Rashdan, D. Bani Mustafa, M.S. Nasif, Computational Fluid Dynamics Analysis of Slip Flow and Heat Transfer at the Entrance Region of a Circular Pipe, Appl. Sci. 2024, Vol. 14, Page 6528. 14 (2024) 6528. https://doi.org/10.3390/APP14156528.

153

[228] O.A. Alawi, N.A.C. Sidik, H.W. Xian, T.H. Kean, S.N. Kazi, Thermal conductivity and viscosity models of metallic oxides nanofluids, Int. J. Heat Mass Transf. 116 (2018) 1314–1325. https://doi.org/10.1016/J.IJHEATMASSTRANSFER.2017.09.133.

[229] M. Gupta, V. Singh, Z. Said, Heat transfer analysis using zinc Ferrite/water (Hybrid) nanofluids in a circular tube: An experimental investigation and development of new correlations for thermophysical and heat transfer properties, Sustain. Energy Technol. Assessments. 39 (2020) 100720. https://doi.org/10.1016/J.SETA.2020.100720.

[230] S.O. Giwa, M. Sharifpur, M. Goodarzi, H. Alsulami, J.P. Meyer, Influence of base fluid, temperature, and concentration on the thermophysical properties of hybrid nanofluids of alumina–ferrofluid: experimental data, modeling through enhanced ANN, ANFIS, and curve fitting, J. Therm. Anal. Calorim. 143 (2021) 4149–4167. https://doi.org/10.1007/S10973-020-09372-W/METRICS.

[231] J.S. Goud, P. Srilatha, R.S. Varun Kumar, K.T. Kumar, U. Khan, Z. Raizah, H.S. Gill, A.M. Galal, Role of ternary hybrid nanofluid in the thermal distribution of a dovetail fin with the internal generation of heat, Case Stud. Therm. Eng. 35 (2022) 102113. https://doi.org/10.1016/J.CSITE.2022.102113.

[232] S.G. Kandlikar, A. V. Bapat, Evaluation of jet impingement, spray and microchannel chip cooling options for high heat flux removal, Heat Transf. Eng. 28 (2007) 911–923. https://doi.org/10.1080/01457630701421703.

[233] R.W. Hornbeck, Laminar flow in the entrance region of a pipe, Appl. Sci. Res. 13 (1964) 224–232. https://doi.org/10.1007/BF00382049/METRICS.

[234] R.K. Shah, A.L. London, Laminar Flow Forced Convection in Ducts: A Source Book for Compact Heat Exchanger Analytical Data, Laminar Flow Forced

154

Convect.     Ducts.     Suppl.     1     (1978)     1–482.
http://www.sciencedirect.com/science/article/pii/B978012020051150022X
(accessed July 29, 2025).

[235] R.J. Phillips, Forced-convection, liquid-cooled, microchannel heat sinks,
(1987). https://dspace.mit.edu/handle/1721.1/14921 (accessed July 29, 2025).

[236] O.G. Jones, An Improvement in the Calculation of Turbulent Friction in
Rectangular     Ducts,     J.     Fluids     Eng.     98     (1976)     173–180.
https://doi.org/10.1115/1.3448250.

[237] J.P. Hartnett, J.C.Y. Koh, S.T. McComas, A Comparison of Predicted and
Measured Friction Factors for Turbulent Flow Through Rectangular Ducts, J.
Heat Transfer. 84 (1961) 82–88. https://doi.org/10.1115/1.3684299.

[238] A. Bucci, G.P. Celata, M. Cumo, E. Serra, G. Zummo, Water Single-Phase
Fluid Flow and Heat Transfer in Capillary Tubes, Int. Conf. Microchannels
Minichannels. 1 (2009) 319–326. https://doi.org/10.1115/ICMM2003-1037.

[239] S.G. Kandlikar, High flux heat removal with microchannels - A roadmap of
challenges     and     opportunities,     Heat     Transf.     Eng.     26     (2005)     5–14.
https://doi.org/10.1080/01457630591003655.

[240] S.G. Kandlikar, S. Garimella, D. Li, S. Colin, M.R. King, Heat Transfer and
Fluid     Flow     in     Minichannels     and     Microchannels,     2006.
https://doi.org/10.1016/B978-0-08-044527-4.X5000-2.

[241] Ansys Inc, Ansys Fluent workbench Tutorial Guide, (2021) 1–1025.

[242] T. Bergman, A. Lavine, F. Incropera, D. DeWitt, Introduction to heat transfer,
2011.

[243] D. V. Pence, Improved thermal efficiency and temperature uniformity using
fractal-like branching channel networks, Heat Transf. Transp. Phenom.

155

Microscale. (n.d.) 142–148. https://doi.org/10.1615/1-56700-150-5.180.

[244] P. Xu, B. Yu, M. Yun, M. Zou, Heat conduction in fractal tree-like branched networks, Int. J. Heat Mass Transf. 49 (2006) 3746–3751. https://doi.org/10.1016/J.IJHEATMASSTRANSFER.2006.01.033.

[245] M. Bezaatpour, M. Goharkhah, A magnetic vortex generator for simultaneous heat transfer enhancement and pressure drop reduction in a mini channel, Heat Transf. 49 (2020) 1192–1213. https://doi.org/10.1002/HTJ.21658;CTYPE:STRING:JOURNAL.

[246] S.B. Islami, B. Dastvareh, R. Gharraei, Numerical study of hydrodynamic and heat transfer of nanofluid flow in microchannels containing micromixer, Int. Commun. Heat Mass Transf. 43 (2013) 146–154. https://doi.org/10.1016/J.ICHEATMASSTRANSFER.2013.01.002.

[247] S. Mirjalili, Moth-flame optimization algorithm: A novel nature-inspired heuristic paradigm, Knowledge-Based Syst. 89 (2015) 228–249. https://doi.org/10.1016/J.KNOSYS.2015.07.006.

[248] A.A. Heidari, S. Mirjalili, H. Faris, I. Aljarah, M. Mafarja, H. Chen, Harris hawks optimization: Algorithm and applications, Futur. Gener. Comput. Syst. 97 (2019) 849–872. https://doi.org/10.1016/J.FUTURE.2019.02.028.

[249] M.E. Steinke, S.G. Kandlikar, Single-phase liquid friction factors in microchannels, Int. J. Therm. Sci. 45 (2006) 1073–1083.

[250] M.E. Steinke, S.G. Kandlikar, Single-phase liquid friction factors in microchannels, Int. J. Therm. Sci. 45 (2006) 1073–1083. https://doi.org/10.1016/J.IJTHERMALSCI.2006.01.016.

156

# LIST OF PUBLICATIONS

## Published paper in International Journals

i.  H. Sadique, Q. Murtaza, and Samsher, "Heat transfer augmentation in microchannel heat sink using secondary flows: A review," International Journal of Heat and Mass Transfer, vol. 194, p. 123063, Sep. 2022, doi: https://doi.org/10.1016/j.ijheatmasstransfer.2022.123063

ii. H. Sadique, Samsher, and Q. Murtaza, "Numerical study and moth flame optimization of thermal–hydraulic performance of fractal microchannel heat sink with ribs and cavity," International Journal of Heat and Fluid Flow, vol. 113, p. 109777, Feb. 2025, doi: https://doi.org/10.1016/j.ijheatfluidflow.2025.109777

## Paper Presented/Published in International Conferences

i.  H. Sadique, Q. Murtaza, and Samsher, "Numerical Investigation of the Effects of Al2O3 Nanofluid on the Thermohydraulic Performance of Fractal Microchannel Heat Sink," Lecture notes in mechanical engineering, pp. 421–433, Jan. 2024,

doi: https://doi.org/10.1007/978-981-97-5373-4_34.

ii. H. Sadique, Samsher, and Q. Murtaza, "Numerical Study on the Effect of Rib Configurations on the Thermal-Hydrodynamic Performance of Microchannel Heat Sink," Lecture Notes in Mechanical Engineering, pp. 327–339, 2024, doi: https://doi.org/10.1007/978-981-97-0918-2_26

# CURRICULUM VITAE

## Hussam Sadique

## Research Scholar | Mechanical Engineering | Computational Fluid Dynamics

Hussam Sadique is a dedicated research scholar at Delhi Technological University, specializing in computational fluid dynamics and finite element analysis. With a strong academic background, his work focuses on computational analysis of microchannel heat sinks. He possesses a strong academic foundation, and a diverse skill set that includes machine learning applications, Python programming, ANSYS Workbench, and SolidWorks.

He is presently working as a Lecturer in the Department of Science, Technology, and Technical Education (DSTTE), Government of Bihar. He has extensive teaching and research experience, having served as a Teaching Assistant in the Department of Mechanical Engineering at Delhi Technological University since 2017. His research interests lie in thermal management of MEMS, emissions in diffusion flames, and microfluidics. He has contributed to numerous publications in reputed journals and conferences.

His expertise also spans MS Office, modelling, and numerical simulation techniques, with a focused interest in heat transfer and fluid mechanics. Through his ongoing research, he aims to advance the understanding of fluid dynamics in microfluidic systems, contributing to improvements in energy efficiency and mechanical engineering design.

**Key Skills:** Microchannels, Heat Transfer, Machine Learning, Computational Fluid Dynamics, Finite Element Analysis, Ansys Workbench, SolidWorks.

**Email:** hussam.mech@gmail.com

158

# Annexure

## A1: Regression Coefficient Codes

```matlab
%% Neural Network Setup for an Equivalent Polynomial Fit
% Our target model:
%   y = b0 + b1*x1 + b2*x2 + b3*x1^2 + b4*x1*x2 + b5*x2^2
% Data is provided as rows: [y, x1, x2]

% === Step 1: Define Your Data ===
m=[target2;input]
M=m'
data = [M];

% === Step 2: Prepare the Data for the Neural Network ===
% Our inputs are x1 and x2. Arrange the inputs as a 2 x N matrix.
x1 = data(:,2);
x2 = data(:,3);
N  = size(data,1);
X = [x1, x2]';  % Now X is 2 x N

% Our target output is y (a 1 x N vector).
Y = data(:,1)';

% For our equivalent polynomial network, we precompute the polynomial
basis
% For a quadratic polynomial in x1 and x2, we want these 6 basis
functions:
% 1, x1, x2, x1^2, x1*x2, x2^2.
U = [ones(N,1), x1, x2, x1.^2, x1.*x2, x2.^2]';  % U is 6 x N

% === Step 3A: Direct Polynomial Regression (for reference) ===
% Solve U * coeffs = Y' (with Y' as N x 1)
coeffs_direct = (U') \ Y';
fprintf('Direct polynomial regression coefficients:\n');
fprintf('y = %.4f + %.4f*x1 + %.4f*x2 + %.4f*x1^2 + %.4f*x1*x2 +
%.4f*x2^2\n', coeffs_direct);

% === Step 3B: Neural Network Training on Augmented (Polynomial Basis)
Data ===
% Here we build a network that takes as input the polynomial basis U.
% Since the mapping is linear in these basis functions, we can use a
network
% with no hidden layers (i.e. a single linear layer).
netPoly = feedforwardnet([],'trainlm');  % [] means no hidden layer
netPoly = configure(netPoly, U, Y);
% Train the network on the augmented data.
netPoly.trainParam.epochs = 300;  % adjust epochs as needed
netPoly = train(netPoly, U, Y);

% After training, the network consists of a single layer. Its weights
and bias are:
W_nn = netPoly.IW{1};  % 1 x 6 weight matrix
b_nn = netPoly.b{1};   % scalar bias

fprintf('\nNeural network (polynomial basis) coefficients:\n');
fprintf('y = %.4f + %.4f*x1 + %.4f*x2 + %.4f*x1^2 + %.4f*x1*x2 +
%.4f*x2^2\n', b_nn, W_nn);
```

159

```matlab
% === Step 4: Compare the Two Approaches ===
% They should be very close if the network has converged.
disp('Difference between direct and NN coefficients:');
disp(coeffs_direct' - [b_nn, W_nn]');

%% (Optional) Visualize the Fit
% We create a grid of x1 and x2 values, compute the polynomial
prediction using the NN weights,
% and plot the resulting surface along with the original data points.
numPoints = 50;
x1_grid = linspace(min(x1), max(x1), numPoints);
x2_grid = linspace(min(x2), max(x2), numPoints);
[X1, X2] = meshgrid(x1_grid, x2_grid);
% Compute the polynomial basis for each grid point:
U_grid  = [ones(numPoints*numPoints,1),  X1(:),  X2(:),  X1(:).^2,
X1(:).*X2(:), X2(:).^2]';
Y_grid = netPoly(U_grid);  % Evaluate the network (which is equivalent
to our polynomial)
Y_grid = reshape(Y_grid, numPoints, numPoints);

figure;
surf(X1, X2, Y_grid, 'EdgeColor','none','FaceAlpha',0.8);
colormap jet;
hold on;
scatter3(x1, x2, data(:,1), 50, 'k', 'filled');
xlabel('x1');
ylabel('x2');
zlabel('y');
title('Neural Network Polynomial Fit (Equivalent Equation)');
hold off;
```

## A2: Pareto Curve Code

```matlab
clc;
clear Best_score;
clear Best_pos;
clear cg_curve;

% Parameters for HHO and Pareto Optimization
SearchAgents_no = 30;   % Number of search agents
Max_iteration = 100;    % Maximum number of iterations

% Bounds and dimensionality for HHO
lb = [-1 200];  % Lower bounds
ub = [1 400];   % Upper bounds
dim = 2;        % Dimensionality of x

% Initialize parameters for Pareto optimization
numRuns = 10;                              % Number of runs for
different weights
weightCombinations = linspace(0, 1, numRuns); % Weight range for
Pareto front
paretoResults = zeros(numRuns^3, 4);       % Store of1, of2, of3,
and of4 values for Pareto plot
BestPosResults = zeros(numRuns^3, dim);    % Store optimal positions

% Index for storing results
```

160

```matlab
index = 1;

% Loop through each combination of weights to calculate the Pareto
front
for w1 = weightCombinations
    for w2 = weightCombinations
        for w3 = weightCombinations
            % Ensure the sum of weights equals 1
            w4 = 1 - (w1 + w2 + w3);
            if w4 < 0
                continue;
            end

            % Define the weighted objective function for HHO
            fobj = @(x) w1 * objective1(r, x) + w2 * objective2(s, x)
+ w3 * objective3(t, x) + w4 * objective4(u, x);

            % Run HHO optimization
            [Best_score, Best_pos, cg_curve] = HHO(SearchAgents_no,
Max_iteration, lb, ub, dim, fobj);

            % Store optimized of1, of2, of3, and of4 values
            of1_optimal = objective1(r, Best_pos);
            of2_optimal = objective2(s, Best_pos);
            of3_optimal = objective3(t, Best_pos);
            of4_optimal = objective4(u, Best_pos);
            paretoResults(index, :) = [of1_optimal, of2_optimal,
of3_optimal, of4_optimal];

            % Save the Best_pos parameters corresponding to the
optimal results
            BestPosResults(index, :) = Best_pos;
            index = index + 1;
        end
    end
end

% Plot the Pareto front in 4D space (Scatter plots of all combinations)
figure;
subplot(2, 2, 1);
scatter3(paretoResults(:, 1), paretoResults(:, 2), paretoResults(:,
3), 'filled');
xlabel('Objective 1 (of1)');
ylabel('Objective 2 (of2)');
zlabel('Objective 3 (of3)');
title('Pareto Front (of1, of2, of3)');
grid on;

subplot(2, 2, 2);
scatter3(paretoResults(:, 1), paretoResults(:, 2), paretoResults(:,
4), 'filled');
xlabel('Objective 1 (of1)');
ylabel('Objective 2 (of2)');
zlabel('Objective 4 (of4)');
title('Pareto Front (of1, of2, of4)');
grid on;

subplot(2, 2, 3);
scatter3(paretoResults(:, 1), paretoResults(:, 3), paretoResults(:,
4), 'filled');
```

161

```matlab
xlabel('Objective 1 (of1)');
ylabel('Objective 3 (of3)');
zlabel('Objective 4 (of4)');
title('Pareto Front (of1, of3, of4)');
grid on;

subplot(2, 2, 4);
scatter3(paretoResults(:, 2), paretoResults(:, 3), paretoResults(:, 4), 'filled');
xlabel('Objective 2 (of2)');
ylabel('Objective 3 (of3)');
zlabel('Objective 4 (of4)');
title('Pareto Front (of2, of3, of4)');
grid on;

% Convergence curve for the last run
figure;
semilogy(cg_curve, 'Color', 'b');
title('Convergence curve');
xlabel('Iteration');
ylabel('Best flame (score) obtained so far');
axis tight;
grid off;
box on;
legend('HHO');

% Display the best solution and score found
display(['The    best    solution    obtained    by    HHO    is    :    ', num2str(Best_pos)]);
display(['The best optimal value of the objective function found by HHO is : ', num2str(Best_score)]);
```

## A3: Polynomial Equation Codes

```matlab
%% Neural Network Setup for an Equivalent Polynomial Fit
% Our target model:
%    y = b0 + b1*x1 + b2*x2 + b3*x3 + b4*x4 + b5*x1^2 + b6*x1*x2 + b7*x1*x3 + b8*x1*x4 +
%          b9*x2^2 + b10*x2*x3 + b11*x2*x4 + b12*x3^2 + b13*x3*x4 + b14*x4^2
% Data is provided as rows: [y, x1, x2, x3, x4]

% === Step 1: Define Your Data ===
m=[target2;input]
M=m'
data = [M];

% === Step 2: Prepare the Data for the Neural Network ===
% Our inputs are x1, x2, x3, and x4. Arrange the inputs as a 4 x N matrix.
x1 = data(:,2);
x2 = data(:,3);
x3 = data(:,4);
x4 = data(:,5);
N  = size(data,1);
X = [x1, x2, x3, x4]';   % Now X is 4 x N

% Our target output is y (a 1 x N vector).
Y = data(:,1)';
```

162

```matlab
% For our equivalent polynomial network, we precompute the polynomial
basis
% For a quadratic polynomial in x1, x2, x3, and x4, we want these 15
basis functions:
% 1, x1, x2, x3, x4, x1^2, x1*x2, x1*x3, x1*x4, x2^2, x2*x3, x2*x4,
x3^2, x3*x4, x4^2.
U = [ones(N,1), x1, x2, x3, x4, x1.^2, x1.*x2, x1.*x3, x1.*x4, ...
     x2.^2, x2.*x3, x2.*x4, x3.^2, x3.*x4, x4.^2]';  % U is 15 x N

% === Step 3A: Direct Polynomial Regression (for reference) ===
% Solve U * coeffs = Y' (with Y' as N x 1)
coeffs_direct = (U') \ Y';
fprintf('Direct polynomial regression coefficients:\n');
fprintf('y = %.4f + %.4f*x1 + %.4f*x2 + %.4f*x3 + %.4f*x4 + %.4f*x1^2
+ %.4f*x1*x2 + %.4f*x1*x3 + %.4f*x1*x4 + %.4f*x2^2 + %.4f*x2*x3 +
%.4f*x2*x4 + %.4f*x3^2 + %.4f*x3*x4 + %.4f*x4^2\n', coeffs_direct);

% === Step 3B: Neural Network Training on Augmented (Polynomial Basis)
Data ===
% Here we build a network that takes as input the polynomial basis U.
% Since the mapping is linear in these basis functions, we can use a
network
% with no hidden layers (i.e. a single linear layer).
netPoly = feedforwardnet([],'trainlm');  % [] means no hidden layer
netPoly = configure(netPoly, U, Y);
% Train the network on the augmented data.
netPoly.trainParam.epochs = 300;  % adjust epochs as needed
netPoly = train(netPoly, U, Y);

% After training, the network consists of a single layer. Its weights
and bias are:
W_nn = netPoly.IW{1};  % 1 x 15 weight matrix
b_nn = netPoly.b{1};   % scalar bias

fprintf('\nNeural network (polynomial basis) coefficients:\n');
fprintf('y = %.4f + %.4f*x1 + %.4f*x2 + %.4f*x3 + %.4f*x4 + %.4f*x1^2
+ %.4f*x1*x2 + %.4f*x1*x3 + %.4f*x1*x4 + %.4f*x2^2 + %.4f*x2*x3 +
%.4f*x2*x4 + %.4f*x3^2 + %.4f*x3*x4 + %.4f*x4^2\n', b_nn, W_nn);

% === Step 4: Compare the Two Approaches ===
% They should be very close if the network has converged.
disp('Difference between direct and NN coefficients:');
disp(coeffs_direct' - [b_nn, W_nn]');
```

163